4-2006

Performance-Metric Driven Atmospheric Compensation for Robust Free-Space Laser Communication

Peter N. Crabtree

Performance-Metric Driven Atmospheric Compensation for Robust Free-Space Laser Communication

DISSERTATION

Peter N. Crabtree, Major, USAF

AFIT/DS/ENG/06-03

DEPARTMENT OF THE AIR FORCE
AIR UNIVERSITY

AIR FORCE INSTITUTE OF TECHNOLOGY

Wright-Patterson Air Force Base, Ohio

The views expressed in this dissertation are those of the author and no not reflect the official policy or position of the United States Air Force, Department of Defense, or the United States Government.

AFIT/DS/ENG/06-03

Performance-Metric Driven Atmospheric Compensation for Robust Free-Space Laser Communication

DISSERTATION

Presented to the Faculty

Graduate School of Engineering and Management

Air Force Institute of Technology

Air University

Air Education and Training Command

In Partial Fulfillment of the Requirements for the

Degree of Doctor of Philosophy

Peter N. Crabtree, B.S.E.E., M.S.E.E.

Major, USAF

March 2006

AFIT/DS/ENG/06-03

Performance-Metric Driven Atmospheric Compensation for Robust Free-Space Laser Communication

Peter N. Crabtree, B.S.E.E., M.S.E.E.
Major, USAF

Approved:

Lt Col Matthew E. Goda, Ph.D. Dissertation Advisor	30 MARCH 06 Date
Dr. William P. Baker Committee Member	30 Mar 06 Date
Dr. Michael A. Temple Committee Member	31 Mar 06 Date
Dr. Edward A. Watson Committee Member	30 MAR 06 Date
Dr. James T. Moore Dean's Representative	30 March 2006 Date

Accepted:

M.U. Thomas Dean, Graduate School of Engineering and Management	3 April 2006 Date

AFIT/DS/ENG/06-03

Abstract

The effect of turbulence on laser propagation is a significant challenge to current electro-optical systems. While atmospheric compensation techniques in space object imaging and high-energy laser weapons have been thoroughly investigated, optimizing these techniques for Laser Communication (LaserCom) has not been examined to the same degree. Average Strehl ratio is the typical design metric for current atmospheric compensation systems. However, fade probability is the relevant metric for LaserCom. This difference motivated the investigation into metric-driven atmospheric compensation.

Metric-based tracking techniques for fade mitigation is the first major focus of this research. In a moderate range air-to-air scenario, focal plane spot breakup is the dominant failure mechanism. Although the impact of spot breakup on average Strehl is small, spot breakup considerably increases fade probability. This result demonstrates that optimization of an atmospheric compensation system requires consideration of the metric of interest. Metric-driven design led to exploration of peak intensity tracking, which reduces fade probability by greater than 50% over conventional centroid trackers and Adaptive Optics (AO) systems for scenarios studied.

An investigation of atmospheric compensation requirements based on deep fade phenomenology is the second major focus of this research. Fades are classified based on complexity of the required compensation technique. For compensation techniques studied, regions of superior performance, in terms of fade probability, are identified. Peak tracking is shown to outperform AO for thresholds below approximately 4% of the unabberated intensity. Furthermore, the boundary between superior performance regions is nearly invariant to turbulence strength. This boundary invariance simplifies operation of a composite system which is able to adaptively select compensation methodology in near real-time.

An adaptive binary decision threshold is the third major focus of this research. Results show this technique to be viable for decreasing Bit-Error Rate (BER) in the presence of scintillation and receiver noise. Expressions for BER are derived for both the fixed and adaptive threshold cases. Analytic results show that an adaptive threshold provides a BER improvement of up to 1.60 orders of magnitude (33-fold decrease) for a 10 Gbps link, and up to 0.56 orders of magnitude (3.6-fold decrease) for a 10 Mbps link. Adaptive thresholding yields improved performance without the additional cost, weight, and/or complexity of increasing source power, incorporating wavefront control at receiver, or incorporating AO at the transmitter.

Acknowledgements

First, I would like to thank my parents for a constant love, encouragement, and patience that all children (and people) deserve, but many do not receive. After setting aside personal career ambitions years ago to raise my three siblings and I, my mother went to college later in life and now teaches high school English. The sincere desire and appreciation she has for education, both for herself and her students, is a true inspiration. More recently, Almighty God has blessed me with a wonderful soul-mate. Thank you, my wife, for your love. I would also like to thank my faculty advisors, Lt Col Goda, Dr. Baker, Dr. Temple, and Dr. Watson, for their guidance and support throughout the course of this research effort. A special thanks also goes to Dr. Spillar and Dr. Rhoadarmer of the Air Force Research Lab for their insight and suggestions.

Peter N. Crabtree

Table of Contents

List of Figures

List of Tables

List of Symbols

Symbol		Page
η	Quantum Efficiency	131
ν	Optical Frequency	131
i_T	Decision Threshold in terms of Detector Current	135
P_{FA}	Probability of False Alarm	135
P_{MD}	Probability of Missed Detection	135

List of Abbreviations

Abbreviation		Page
LGS	Laser Guide Star	56
NIR	Near Infrared	56
SI	Shearing Interferometer	57
SRI	Self-Referencing Interferometer	57
LS	Least-Squares	57
MEMS	Micro Electro-Mechanical System	58
SLM	Spatial Light Modulator	58
BP	Branch Point	63
MCAO	Multi-Conjugate Adaptive Optics	68
OOK	On-Off Keyed	71
FEC	Forward Error-Correction Code	71
SMF	Single Mode Fiber	72
GEO	Geosynchronous Orbit	79
MOI	Metric of Interest	91
CE	Coupling Efficiency	110

Performance-Metric Driven Atmospheric Compensation for Robust Free-Space Laser Communication

I. Introduction

1.1 Problem Definition

The atmosphere presents a significant challenge for many Electro-Optical (EO) systems. Attenuation, scattering, turbulence, clouds, and thermal blooming are all potential obstacles to system performance. For this research, turbulence is the sole atmospheric distortion investigated. Atmospheric turbulence can be described by random fluctuations in the velocity of nearly homogeneous patches of air existing in a continuum of sizes. The chaotic mixing of these atmospheric cells leads to a random distribution of air temperature and pressure, and therefore refractive index. The resulting phase distortions imposed on wavefronts traveling through the atmosphere are termed optical turbulence. Extended turbulence and challenging engagement scenarios also lead to amplitude fluctuations, which are sensed as intensity variations by the human eye and optical detectors. The twinkling of stars is a well known example.

A variety of atmospheric compensation methods have been investigated, mostly from the perspective of High-Energy Laser (HEL) weapons and space object imaging. These methods are broadly classified as either real-time or post-processing techniques [84]. Hybrid techniques have also been considered for image restoration. A real-time system relies on a mechanical device to adjust the wavefront phase. This technology area is known as Adaptive Optics (AO). Post-processing algorithms for image restoration are often studied from an inverse filtering or deconvolution framework.

A Mean Square Error (MSE) performance metric is typical of both AO systems and image restoration algorithms. For post-processing techniques, the common metric is the MSE between the truth and restored image intensities. In AO, the aperture averaged mean square phase abberation is often used for system analysis and design. For a closed-loop system, assuming negligible amplitude fluctuations, mean square phase is directly related to average Strehl ratio [47, 89]. As a result, characterization of turbulence effects and optimization of AO performance is typically accomplished in terms of mean square phase [44, 64, 101, 103].

Laser Communication (LaserCom) is the primary application motivating this research. Unmanned Aerial Vehicles (UAVs) of various sizes are playing an ever increasing role in surveillance, reconnaissance, and weapon delivery applications. In the case of imagery collection, large amounts of data must be quickly disseminated to decision makers. LaserCom is under investigation to improve this capability. For communication performance, the probability of fade, which is associated to the tail of the signal power's Probability Density Function (PDF), is more important than average signal power. In summary, the difference of design approaches based on minimizing MSE versus preventing deep signal fades is the motivation for this research. The additional weight, size, power, and other constraints imposed on small airborne platforms are also considered in the sense that simplicity is desired.

1.2 Problem Relevance

HEL weapons and LaserCom are both important transformational technologies for the military. HEL weapons, and directed-energy weapons in general, will provide future battlefield commanders with unique capabilities. These technologies offer profound advantages over conventional weapons [80] given their potential for instantly delivering tailored effects from a large standoff distance with pin-point accuracy [81:15]. LaserCom is envisioned as a replacement and/or complement to existing Radio-Frequency (RF) based communication links. Very small optical wavelengths and corresponding narrow beamwidths make interception much more difficult than

for RF systems. LaserCom can serve as a rapidly deployable, high-bandwidth, highly secure, line-of-sight connection, improving the ability to provide decision makers with near real-time access to data collected [81:15]. In fact, commercial LaserCom components were installed within days of the terrorist attack on the World Trade Center, successfully re-establishing high speed data links used by Merrill Lynch Brokerage [54]. However, optical wavelengths are also much more susceptible to atmospheric turbulence effects than those in the RF range.

1.3 Research Contributions

The primary contributions from this research are

- Extended the standard approach to atmospheric turbulence compensation system design from one that strives to minimize MSE to one that strives to optimize a particular metric of interest: fade probability.
- Identified focal plane image breakup as the dominant failure mechanism causing deep fades for moderate range air-to-air LaserCom. Significant breakup first occurs when $D/r_0 \approx 0.6$ and $\sigma_\chi^2 = 0.19$.
- Investigated alternate tracking techniques based on metric-driven design and knowledge of spot breakup.
  - Demonstrated that peak-intensity tracking outperforms traditional centroid tracking and AO in terms of the metric of interest. Fade probability is reduced by greater than 50% over conventional centroid trackers and AO systems for scenarios studied.
  - Demonstrated that metric-driven control of two wavefront phase modes outperforms MSE-driven control of over 23 modes for the metric of interest. This improved performance is achieved with a simpler system, which is very important for potential UAV based optical receivers.
- Defined an architecture to further examine preferred regions of operation for various atmospheric compensation techniques. The fade threshold boundary for

defining regions of superior performance for AO and peak tracking is demonstrated to be nearly invariant to turbulence strength. This boundary invariance simplifies operation of a composite system which is able to adaptively select compensation methodology in real-time.

- Demonstrated that an adaptive threshold provides a Bit-Error Rate (BER) improvement of up to 1.60 orders of magnitude (33-fold decrease) for a 10 Gbps link, and up to 0.56 orders of magnitude (3.6-fold decrease) for a 10 Mbps link. Adaptive thresholding yields improved performance without the additional cost, weight, and/or complexity of increasing source power, incorporating wavefront control at receiver, or incorporating AO at the transmitter.

1.4 Document Outline

Chapter II covers background necessary for a study of light propagation through atmospheric turbulence. Critical mathematical concepts are first reviewed, followed by a theoretic discussion of atmospheric optical turbulence and its characterization. Free-space optical wave propagation is then reviewed, which is based on the scalar wave equation derived from Maxwell's equations. Finally, the theory of propagation through turbulence and the accepted approach to its numerical modelling are discussed.

Chapter III provides necessary background on laser communication and AO. A brief history of AO technology development is provided. A basic system for compensated real-time imaging is then described, including discussions of the major subsystems: beacon, wavefront sensor, wavefront computer, and deformable mirror. Next is a discussion of Strehl ratio, which is the standard performance metric for AO systems. Two forms of instantaneous Strehl ratio are formulated for use in subsequent chapters. Next is a discussion of error sources and system limitations, followed by a review of one advanced concept currently being investigated to improve AO performance in very challenging scenarios. Next, digital communication and direct-detection Laser-

Com are described. Last, existing literature relevant to this research is reviewed, including a summary of important concepts for atmospheric compensation.

Chapter IV presents the results of an investigation of alternate tracking algorithms for LaserCom fade mitigation. A moderate range air-to-air scenario was studied using analysis and wave-optics simulation. Focal plane image spot breakup is shown to be the dominant failure mechanism. The impact of spot breakup is minimal for average Strehl, but considerable for fade probability - demonstrating that optimization of a wavefront control system should consider the performance metric of interest. Fade probability is directly related to BER for direct-detection communication systems. Metric-driven design led to exploration of peak intensity tracking, which reduced fade probability by greater than 50% over conventional centroid trackers and AO systems for scenarios studied. The duration of both signal fades and periods of focal plane image breakup are then characterized. From a system design standpoint these results are important for both sensor frame-rate and system bandwidth requirements, as well as optimizing error-correction codes. At times, the peak tracker jumped from one subspot to another during a single period of spot breakup, leading to fade conditions. Modifications to the basic peak tracking algorithm are proposed and show promise for further performance improvement.

Chapter V investigates atmospheric compensation requirements based on deep fade phenomenology. Fades are classified based on complexity of the required compensation technique. For compensation techniques studied, regions of superior performance are identified in terms of fade probability as a function of detection threshold. Peak tracking outperforms AO for thresholds below approximately 4% of the unabberated intensity. Furthermore, the boundary between regions of superior performance is nearly invariant to turbulence strength. This boundary invariance simplifies operation of a composite system which is able to adaptively select compensation methodology in real-time.

Chapter VI presents an adaptive binary decision threshold for mitigating scintillation induced bit-errors. Results show this technique to be viable for decreasing BER in the presence of scintillation and receiver noise. Expressions for BER are derived for both the fixed and adaptive threshold cases. Analytic results show an adaptive threshold provides BER improvement of 0.41 to 1.60 orders of magnitude for a 10 Gbps link, and up to 0.56 orders of magnitude for a 10 Mbps link. Adaptive thresholding yields improved performance without the additional cost, weight, and/or complexity of increasing source power, incorporating wavefront control at receiver, or incorporating AO at the transmitter.

Chapter VII concludes with a review of primary research contributions.

II. Atmospheric Turbulence and the Propagation of Light

This chapter covers relevant background in the areas of mathematics, optics, and atmospheric turbulence. Fundamental mathematical concepts and relations crucial to analysis of turbulence and propagation are presented in Section 2.1. Section 2.2 covers atmospheric turbulence theory applicable to the visible and infrared wavelengths. Section 2.3 discusses free-space propagation of light, fundamentally governed by Maxwell's equations. Optical turbulence effects on propagation are covered in Section 2.4. Finally, Section 2.5 introduces the numerical simulation approach commonly used for high-fidelity modelling of optical turbulence effects.

2.1 Mathematical Foundations

2.1.1 Linear Systems and Random Processes. For Linear Time-Invariant (LTI) or Linear Space-Invariant (LSI) systems and deterministic signals, the input, $x(t)$, and output, $y(t)$, are related by

$$\begin{aligned} y(t) &= \int_{-\infty}^{\infty} x(\alpha)h(t-\alpha)d\alpha \\ &= (x \circledast h)(t) \quad , \end{aligned} \tag{2.1}$$

where $h(t)$ is the system impulse response and $\circledast$ is the convolution operator. This input-output relationship becomes straightforward multiplication in the frequency domain:

$$Y(f) = X(f)H(f) \quad , \tag{2.2}$$

where $Y(f)$, $X(f)$, and $H(f)$ are the Fourier transforms of $y(t)$, $x(t)$, and $h(t)$, respectively. Under certain conditions, a similar relationship holds for stochastic signals. For Wide-Sense Stationary (WSS) random processes (constant mean and autocorrelation only a function of separation) the Power Spectral Densities (PSDs) of the input and output of a LTI system are related by

$$S_y(f) = S_x(f)\left|H(f)\right|^2 \quad , \tag{2.3}$$

where $S_x(f)$ and $S_y(f)$ are the PSDs of the input and output, respectively, and $H(f)$ is again the Fourier transform of the system impulse response. Based on the Wiener-Khintchine theorem [6:713], a relationship between the autocorrelation (or covariance) function and the PSD of a WSS random process exists and is given by

$$S_x(f) = \mathcal{F}\left\{\Gamma_x(\tau)\right\} \quad , \tag{2.4}$$

where $\mathcal{F}\{\cdot\}$ is the Fourier transform operator and $\Gamma_x(\tau)$ is the autocorrelation function of the random process x.

A multi-dimensional random process is known as a random field. In general, the spatial autocorrelation of a real-valued scalar random field, $x(\vec{r})$, is given by

$$\Gamma_x\left(\vec{r_1}, \vec{r_2}\right) = E\left\{x(\vec{r_1})x(\vec{r_2})\right\} \quad , \tag{2.5}$$

where $E\{\cdot\}$ is the expectation operator. Several properties are often assumed in the study of optical turbulence to allow application of existing mathematical tools. First, if a random field is statistically homogeneous, then its moments are independent of location (i.e., invariant to translation), and the autocorrelation is solely a function of the separation vector, $\vec{r} = \vec{r_2} - \vec{r_1}$:

$$\begin{aligned} \Gamma_x\left(\vec{r_1}, \vec{r_2}\right) &= E\left\{x(\vec{r_1})x(\vec{r_1} + \vec{r})\right\} \\ &= \Gamma_x(\vec{r}) \quad \forall \ \vec{r_1} \quad . \end{aligned} \tag{2.6}$$

Homogeneity allows application of the Wiener-Khintchine theorem to a random field. Second, if a random field is also statistically isotropic, then its moments are independent of (invariant to) rotation and the autocorrelation is only a function of separation magnitude:

$$\Gamma_x\left(\vec{r_1}, \vec{r_2}\right) = \Gamma_x(|\vec{r}|) \quad . \tag{2.7}$$

Many analyses assume the underlying random process is also ergodic, so that ensemble averages can be equated to temporal (or spatial) averages.

Some useful relations between the spectral and spatial domains are now presented. Following the work of Beland [20:161-164], these relationships are presented in terms of the covariance function:

$$\begin{aligned} B_x\left(\vec{r_1},\vec{r_2}\right) &= E\left\{[x(\vec{r_1})-E\{x(\vec{r_1})\}][x(\vec{r_2})-E\{x(\vec{r_2})\}]\right\} \\ &= \Gamma_x\left(\vec{r_1},\vec{r_2}\right)-E\left\{x(\vec{r_1})E\{x(\vec{r_2})\}\right\}-E\left\{E\{x(\vec{r_1})\}x(\vec{r_2})\right\} \\ &\quad + E\{x(\vec{r_1})\}E\{x(\vec{r_2})\} \\ &= \Gamma_x\left(\vec{r_1},\vec{r_2}\right)-E\{x(\vec{r_1})\}E\{x(\vec{r_2})\} \quad . \end{aligned} \tag{2.8}$$

Note that for zero-mean processes, $E\{x(\vec{r_1})\}=E\{x(\vec{r_2})\}=0$ and the spatial covariance of (2.8) and the spatial autocorrelation of (2.5) are equal.

The three-dimensional Wiener-Khintchine theorem for a homogeneous random field $x(\vec{r})$ is given by

$$\Phi_x(\vec{K})=\left(\frac{1}{2\pi}\right)^3\iiint_{-\infty}^{\infty}B_x(\vec{r})e^{i\vec{K}\cdot\vec{r}}d\vec{r} \quad , \tag{2.9}$$

where $\vec{K}=K_x\hat{x}+K_y\hat{y}+K_z\hat{z}$ is the vector wavenumber and $B_x(\vec{r})$ is the covariance function. The inverse relation is given by

$$B_x\left(\vec{r}\right)=\iiint_{-\infty}^{\infty}\Phi_x(\vec{K})e^{-i\vec{K}\cdot\vec{r}}d\vec{K} \quad . \tag{2.10}$$

For real-valued homogeneous random fields, the covariance and spectrum are both even functions, which implies that (2.9) and (2.10) can be expressed as cosine transforms:

$$\Phi_x(\vec{K})=\left(\frac{1}{2\pi}\right)^3\iiint_{-\infty}^{\infty}B_x(\vec{r})\cos(\vec{K}\cdot\vec{r})d\vec{r} \tag{2.11}$$

and

$$B_x(\vec{r}) = \iiint_{-\infty}^{\infty} \Phi_x(\vec{K}) \cos(\vec{K} \cdot \vec{r}) d\vec{K} \quad . \tag{2.12}$$

If the medium is also statistically isotropic, integration over the two angular dimensions in spherical coordinates gives

$$\Phi_x(K) = \left(\frac{1}{2\pi^2 K} \right) \int_0^{\infty} B_x(r) \sin(Kr) r dr \tag{2.13}$$

and

$$B_x(r) = \frac{4\pi}{r} \int_0^{\infty} \Phi_x(K) \sin(Kr) K dK \quad , \tag{2.14}$$

where $K = |\vec{K}|$ is magnitude of the 3-D wavenumber vector and $r = |\vec{r}|$ is magnitude of the 3-D spatial separation vector. Atmospheric parameters are often measured and statistics estimated in 1-D, so the following relation between the 1-D, $S_x(K)$, and 3-D, $\Phi_x(K)$, PSDs can be very useful:

$$\Phi_x(K) = -\frac{1}{2\pi K} \left[\frac{d}{dK} S_x(K) \right] \quad . \tag{2.15}$$

However, optical systems are typically concerned with fields and their properties in a two-dimensional form - the plane transverse to the optical axis. As such, it can be useful to integrate over the spatial frequency variable corresponding to propagation direction, K_z:

$$F_x(K_x, K_y; z) = \int_{-\infty}^{\infty} \Phi_x(K_x, K_y, K_z) \cos(K_z z) dK_z \quad , \tag{2.16}$$

where $F_x(K_x, K_y; z)$ is the resulting 2-D PSD describing homogeneous fluctuations for planes separated by a distance z. For homogeneous and isotropic conditions, converting to cylindrical coordinates, setting $z = 0$, and integrating out the angular dependence gives the 2-D covariance:

$$B_x(\rho) = 2\pi \int_0^{\infty} J_0(\mathcal{K}\rho) F_x(\mathcal{K}, 0) d\mathcal{K} \quad , \tag{2.17}$$

where $\mathcal{K} = \sqrt{K_x^2 + K_y^2}$ is the magnitude of the radial vector wavenumber and $J_0(\cdot)$ is a Bessel function of the first kind, zero-order.

2.1.2 Structure Functions. Random fields are more difficult to analyze when they are not stationary (i.e., non-homogeneous) because the autocorrelation and covariance functions cannot be spectrally decomposed using the Wiener-Khintchine theorem. However, there are times when a random field can be described as having homogeneous fluctuations about a slowly varying mean. This scenario is known as stationary increments in the temporal domain or local homogeneity in the spatial domain. A locally homogeneous random field, $x(\vec{r})$, is mathematically described by

$$x(\vec{r}) = \mu_x(\vec{r}) + x_1(\vec{r}), \quad E\left\{x_1(\vec{r})\right\} = 0 \quad \forall \ \vec{r} \quad , \tag{2.18}$$

where $x_1(\vec{r})$ is assumed homogeneous and $\mu_x(\vec{r}) = E\left\{x(\vec{r})\right\}$ is the mean of $x(\vec{r})$ and assumed to be slowly varying.

The structure function is defined as

$$D_x(\vec{r_1}, \vec{r_2}) = E\left\{\left[x(\vec{r_1}) - x(\vec{r_2})\right]^2\right\} \quad , \tag{2.19}$$

and is a valuable tool for describing and analyzing locally homogeneous fields. Substituting (2.18) into (2.19) gives an insightful formulation [20:165]:

$$\begin{aligned} D_x(\vec{r_1}, \vec{r_2}) &= [\mu_x(\vec{r_1}) - \mu_x(\vec{r_2})]^2 + E\left\{\left[x_1(\vec{r_1}) - x_1(\vec{r_2})\right]^2\right\} \\ &\quad + 2\mu_x(\vec{r_1}) E\left\{x_1(\vec{r_1}) - x_1(\vec{r_2})\right\} - 2\mu_x(\vec{r_2}) E\left\{x_1(\vec{r_1}) - x_1(\vec{r_2})\right\} \\ &= [\mu_x(\vec{r_1}) - \mu_x(\vec{r_2})]^2 + E\left\{\left[x_1(\vec{r_1}) - x_1(\vec{r_2})\right]^2\right\} \quad ; \end{aligned} \tag{2.20}$$

the structure function is now decomposed into the sum of contributions from the means and the fluctuations. For many physical processes (such as atmospheric turbulence), the difference between the means will be negligible for separations of interest. Therefore, $[\mu_x(\vec{r_1}) - \mu_x(\vec{r_2})]^2 \ll E\left\{\left[x_1(\vec{r_1}) - x_1(\vec{r_2})\right]^2\right\}$ is assumed, which leads to the

following approximation:

$$D_x(\vec{r_1},\vec{r_2}) \approx E\left\{[x_1(\vec{r_1}) - x_1(\vec{r_2})]^2\right\} \tag{2.21}$$

$$\approx D_{x_1}(\vec{r_1},\vec{r_2}) \quad . \tag{2.22}$$

Expanding the argument of the expectation operator in (2.19), the structure function can be rewritten as

$$D_x(\vec{r_1},\vec{r_2}) = E\left\{x(\vec{r_1})^2\right\} + E\left\{x(\vec{r_2})^2\right\} - 2E\left\{x(\vec{r_1})x(\vec{r_2})\right\} \quad . \tag{2.23}$$

Homogeneity (stationarity) allows further simplification:

$$D_x(\vec{r}) = 2E\left\{x(\vec{r_1})^2\right\} - 2E\left\{x(\vec{r_1})x(\vec{r_1}+\vec{r})\right\} \quad . \tag{2.24}$$

When the autocorrelation function exists, the structure function can be expressed as

$$D_x(\vec{r}) = 2\left[\Gamma_x(0) - \Gamma_x(\vec{r})\right] \quad . \tag{2.25}$$

Finally, if the field is also isotropic the structure function only depends on separation magnitude:

$$D_x(r) = 2\left[\Gamma_x(0) - \Gamma_x(r)\right] \quad , \tag{2.26}$$

where $r = |\vec{r}|$.

Similar to the covariance/PSD relationship, a generalized form of the Wiener-Khintchine theorem provides a spectral decomposition of the structure function. Note that if the process is only locally homogeneous, no covariance (autocorrelation) is associated with the PSD. For a locally homogeneous random field, the structure function/PSD relationship is given by [20:164]

$$D_x(\vec{r}) = 2\iiint_{-\infty}^{\infty} \Phi(\vec{K})[1 - \cos(\vec{K}\cdot\vec{r})]d\vec{K} \quad . \tag{2.27}$$

If the random field is also locally isotropic, the spectral decomposition is given by

$$D_x(r) = 8\pi \int_0^\infty \Phi(K) \left[1 - \frac{\sin(Kr)}{Kr}\right] K^2 dK \quad . \tag{2.28}$$

The inverse relation is given by

$$\Phi_x(K) = \left(\frac{1}{4\pi^2 K^2}\right) \int_0^\infty \frac{\sin(Kr)}{Kr} \frac{d}{dr} \left[r^2 \frac{d}{dr} D_x(r)\right] dr \quad . \tag{2.29}$$

The 2-D structure function is related to the 2-D spectrum by

$$D_x(\rho) = 4\pi \int_0^\infty [1 - J_0(\mathcal{K}\rho)] F_x(\mathcal{K}, 0) \mathcal{K} d\mathcal{K} \quad , \tag{2.30}$$

where $\mathcal{K} = \sqrt{K_x^2 + K_y^2}$.

From (2.28) several observations are made about the value of the structure function [20:166]. The term $[1 - \sin(Kr)/Kr]$ acts to high-pass filter the PSD, significantly reducing structure function dependence on low spatial frequencies, which correspond to separations much larger than r. The structure function is also mathematically convenient because, unlike the covariance function, it exists even when there is a singularity at the PSD origin. The result is a statistical descriptor more general than the covariance or autocorrelation.

2.1.3 Orthonormal Basis Functions. Two vectors are orthogonal if their inner (dot) product is zero. Likewise, two functions are orthogonal over the interval (a, b) if their inner (scalar) product is zero:

$$\int_a^b A(x) B(x) dx = 0 \quad . \tag{2.31}$$

Furthermore, a function (vector) is called normalized if its magnitude is unity:

$$\int_a^b A(x) A(x) dx = 1 \quad . \tag{2.32}$$

Consider a complete set of functions $\{\phi_k(x)\}, k = 1, 2, 3, \ldots$, which span the space of an arbitrary function, $f(x)$, and are all normalized and mutually orthogonal:

$$\int_a^b \phi_m(x)\phi_n(x)dx = \delta_{mn} \quad \forall \ m, n \quad , \tag{2.33}$$

where δ_{mn} is the Kronecker delta function given by

$$\delta_{mn} = \begin{cases} 1, & m = n \\ 0, & m \neq n \end{cases} \quad . \tag{2.34}$$

Such an orthonormal basis set can be used to decompose $f(x)$:

$$f(x) = \sum_{n=1}^{\infty} c_n \phi_n(x) \quad a \leq x \leq b \quad , \tag{2.35}$$

proividing a valuable analysis tool. If the series on the right side of (2.35) converges, then the expansion coefficients are given by

$$c_n = \int_a^b f(x)\phi_n(x)dx \quad . \tag{2.36}$$

A finite sum of orthonormal functions can be used to approximate an arbitrary function that is piecewise continuous and has a piecewise continuous first derivative:

$$S_M(x) = \sum_{n=1}^{M} \alpha_n \phi_n(x) \quad a \leq x \leq b \quad . \tag{2.37}$$

The mean square error between $S_M(x)$ and $f(x)$ is minimized when the arbitrary coefficients, α_n, are found using (2.36).

2.1.4 Zernike Polynomials. The Zernikes are a set of polynomials which are orthogonal over the unit circle. The seminal paper addressing application of Zernikes to modelling optical turbulence was published in 1976 by Robert Noll [64]. Following Noll and more recent work of Roggemann and Welsh [84], the Zernike polynomials

Table 2.1: The first 11 Zernike polynomials [65].

n	m	i	Zernike Polynomial	Associated Aberration
0	0	1	1	Piston
1	1	2	$2r\cos\theta$	Tip
1	1	3	$2r\sin\theta$	Tilt
2	0	4	$\sqrt{3}(2r^2-1)$	Defocus
2	2	5	$\sqrt{6}r^2\sin 2\theta$	Astigmatism
2	2	6	$\sqrt{6}r^2\cos 2\theta$	Astigmatism
3	1	7	$\sqrt{8}(3r^3-2r)\sin\theta$	Pure Coma
3	1	8	$\sqrt{8}(3r^3-2r)\cos\theta$	Pure Coma
3	3	9	$\sqrt{8}r^3\sin 3\theta$	Trefoil
3	3	10	$\sqrt{8}r^3\cos 3\theta$	Trefoil
4	0	11	$\sqrt{5}(6r^4-6r^2+1)$	Spherical

are defined by the following equations:

$$Z(r,\theta)_{i=even} = \sqrt{2(n+1)}R_n^m(r)\cos(m\theta), \quad m \neq 0, \tag{2.38}$$

$$Z(r,\theta)_{i=odd} = \sqrt{2(n+1)}R_n^m(r)\sin(m\theta), \quad m \neq 0, \quad \text{and} \tag{2.39}$$

$$Z_i(r,\theta) = \sqrt{n+1}R_n^0(r), \quad m = 0, \tag{2.40}$$

where the azimuthal and radial orders, m and n, respectively, are required to be non-negative integers with $n \geq m$ and $n-m = even$. The Zernike radial functions, $R_n^m(r)$, are defined by

$$R_n^m(r) = \sum_{s=0}^{(n-m)/2} \frac{(-1)^s(n-s)!}{s![(n+m)/2-s]![(n-m)/2-s]!} r^{n-2s} \quad . \tag{2.41}$$

Zernike polynomials are often referenced by the single index, i. The beauty of Zernikes in the analysis of optical turbulence effects is that lower order modes correspond to traditional static abberations, such as coma and astigmatism. The first 11 Zernike polynomials are listed in Table 2.1 [65], along with their corresponding mode numbers and induced optical aberrations.

2.2 Optical Turbulence

2.2.1 Kolmogorov Theory (Velocity Fluctuations). Chaotic motion of air in the atmosphere is the fundamental physical cause of optical turbulence. Therefore, results from the area of fluid dynamics are foundational. Fluid flow is typically characterized as falling into one of two regimes: laminar (smooth and steady) or turbulent (chaotic). The Reynold's number is used to define the transition between these two states. Reasonable assumptions for atmospheric parameters give a Reynold's number on the order of 10^5, which is large enough to assume that atmospheric flow is almost always turbulent [84:58]. The nature of turbulent fluid dynamics is described by the Navier-Stokes equations, which are nonlinear and underdetermined [20:157]. Difficulties in using these equations led Kolmogorov to take a statistical approach in his investigation of velocity fluctuations in the atmosphere.

The main physical construct behind Kolmogorov's approach is the energy cascade theory of Richardson [75], which states that energy is injected into the system at large scale sizes. This large scale size is termed the outer scale, L_0, for atmospheric turbulence. L_0 ranges from tens to a few hundred meters, and near the Earth's surface is proportional to height as $L_0 = 0.4h$ [92]. Energy is injected into the atmosphere by the sun as large air masses are put in motion via convection and/or wind shear. Nearly uniform atmospheric patches are initially on the order of L_0 in size, but break up over time in turbulent flow. Energy thus cascades downward through a continuum of smaller and smaller "eddies." Eventually, eddies reach a lower size threshold called the inner scale, l_0, where energy begins to dissipate as heat [20:167]. The value of l_0 ranges from millimeters near the Earth's surface to centimeters in the upper atmosphere. The range of scale sizes between l_0 and L_0 is termed the inertial range, where kinetic forces dominate and eddy properties are independent of the parent. Kolmogorov assumed that velocity fluctuations are homogeneous and isotropic in this range. Strong turbulence causes l_0 to decrease and L_0 to increase, expanding the inertial range at both ends.

Using dimensional arguments, Kolmogorov showed that the structure function for longitudinal velocity fluctuations in the inertial range is given by

$$D_v(r) = C_v^2 r^{2/3} \ , \qquad l_0 < r < L_0 \quad , \tag{2.42}$$

where C_v^2 is called the velocity "structure constant" and describes the strength of turbulence. Validity of the 2/3 power law structure function breaks down for separations outside the inertial range due to a loss of isotropic conditions. With the assumption of a locally homogeneous and isotropic field, a Taylor's series expansion of the structure function definition of (2.28) for small separations shows behavior proportional to r^2. Continuity of the two regions of behavior is mathematically enforced at $r = l_0$:

$$D_v(r) = C_v^2 l_0^{-4/3} r^2 \ , \qquad r < l_0 \quad . \tag{2.43}$$

2.2.2 Conservative Passive Scalars. Kolmogorov's treatment of turbulence was in terms of velocity fluctuations, which result in a chaotic mixture of various sized parcels, or cells, of air. Each parcel has a slightly different temperature, pressure, and humidity. A particular cell characteristic is termed passive if its dynamics do not affect (exchange energy with) the turbulent flow. Furthermore, the turbulent mixing of air is assumed to be an adiabatic (conservative) process in that a parcel of air swirled around by an eddy does not have time to gain or lose heat [20:170]. Extending Kolmogorov's theory to conservative passive scalars is credited to Corrsin and Obhukov [20:170]. This extension was key because velocity fluctuations are not directly applicable to a study of optical turbulence. However, the index of refraction can be expressed as a function of conservative passive scalars. Kolmogorov theory is thus extended to describe the refractive index variations that cause bending of light rays and changes in optical wavefront phase.

The refractive index, n, for optical and infrared wavelengths at a specific location in the atmosphere is a function of wavelength, pressure, and temperature [5, 41]:

$$n(r) \approx 1 + 77.6 \times 10^{-6}(1 + 7.52 \times 10^{-3}\lambda^{-2})\frac{P(r)}{T(r)} \quad , \tag{2.44}$$

where λ is wavelength in μm, P is pressure in millibars, and T is temperature in kelvin. Dependence on wavelength is relatively weak in the optical range (~ 0.3 to 10 μm). Therefore, (2.44) is often simplified by letting $\lambda = 0.5$ μm [20:173]:

$$n(r) \approx 1 + 79 \times 10^{-6}\frac{P(r)}{T(r)} \quad . \tag{2.45}$$

Differentiating (2.45) with respect to pressure and temperature reveals a greater sensitivity to temperature changes. Potential temperature is a conservative passive scalar, so Kolmogorov theory can be used.

The atmospheric index can be rewritten in terms of potential temperature and specific humidity. This allows extension of Kolmogorov theory to the key quantity of interest for optical turbulence studies: the refractive index. The structure function for refractive index fluctuations is thus seen to follow the 2/3 power law, and is given by

$$D_n(r) = \begin{cases} C_n^2 r^{2/3}, & l_0 \leq r < L_0 \\ C_n^2 l_o^{-4/3} r^2, & r \leq l_0 \end{cases} \quad , \tag{2.46}$$

where C_n^2 is the refractive index "structure constant" and the index fluctuations are assumed to be locally homogeneous and isotropic. The generalized Wiener-Khintchine theorem is used to find the corresponding PSD, known as the Kolmogorov spectrum:

$$\Phi_n(K) = 0.033 C_n^2 K^{-11/3} \quad , \tag{2.47}$$

where $K = |\vec{K}|$ is the magnitude of the three-dimensional spatial frequency vector.

There are several other PSD forms describing refractive index fluctuations. All obey the $-11/3$ power law (three-dimensional spectra) in the inertial range, but some

modifications have been made outside the inertial range - for the sake of mathematical convenience or experimental comparison. Based on an assumed physical model of the fluctuations, Kolmogorov began with the velocity structure function, $D_v(r)$. To use the generalized Wiener-Khintchine theorem to find the corresponding PSD, the structure function is integrated over all separations. The resulting Kolmogorov spectrum has a singularity at $K = 0$, resulting in infinite area under the spectrum. This implies a random process with infinite variance (energy), which is non-physical and not representative of the atmosphere captured by a finite aperture. It is for this reason that several mathematical modifications to the original Kolmogorov spectrum have been developed. The most recent of these modified spectra both bounds total energy under the curve and accounts for a bump seen empirically at high frequencies near $1/l_0$. Although these spectra are mathematically valid for all separations (wavenumbers), their form outside the inertial range is not based on a physical model/understanding of the atmosphere.

Tatarskii [93] proposed a spectrum which allows for a finite inner scale. He multiplied the Kolmogorov PSD by a Gaussian term with a $1/e$ point near $K = 1/l_0$. This low-pass filter significantly reduces spectral energy for wavenumbers larger than about $1/l_0$:

$$\Phi_n(K) = 0.033 C_n^2 K^{-11/3} \exp\left(-\frac{K^2}{K_m^2}\right) \quad , \tag{2.48}$$

where $K_m = 5.92/l_0$ is the Gaussian cutoff ($1/e$ point). Although this specific form was chosen ad-hoc, it makes sense to limit energy in this region because fluctuations disappear as energy begins to dissipate as heat. The von Karman [20:174] spectrum allows for a finite outer scale and eliminates the singularity:

$$\Phi_n(K) = 0.033 C_n^2 (K^2 + K_0^2)^{-11/6} \quad , \tag{2.49}$$

where $K_0 = 2\pi/L_0$. A combination of the Tatarski and von Karman spectra is termed the modified von Karman PSD [20:174]:

$$\Phi_n(K) = 0.033C_n^2(K^2 + K_0^2)^{-11/6} \exp\left(-\frac{K^2}{K_m^2}\right) \quad . \tag{2.50}$$

The modified von Karman spectra is fairly tractable and readily used for theoretical studies. However, behavior outside the inertial range does not reflect empirical data showing a bump at large spatial frequencies (wavenumbers) near $1/l_0$. Hill [5:54] introduced a numerical model known as the "Bump" (or "Hill") PSD that closely matches the experimental data. To increase usefulness of the Hill model, Andrews [5:54] proposed an analytical approximation given by

$$\Phi_n(K) = 0.033C_n^2\left[1 + 1.802\frac{K}{K_l} - 0.254\left(\frac{K}{K_l}\right)^{7/6}\right]\frac{\exp\left\{-\left(\frac{K}{K_l}\right)^2\right\}}{(K^2 + K_0^2)^{11/6}} \quad , \tag{2.51}$$

where $K_l = 3.3/l_0$ and $K_0 = 2\pi/L_0$.

2.2.3 Refractive Index Structure Constant (Parameter). C_n^2 is the primary measure of optical turbulence strength along the propagation path. Several additional scalar parameters which more precisely characterize certain optical effects of turbulence are presented in Section 2.4.2. Many of these additional parameters are proportional to moments of the C_n^2 profile. C_n^2 typically ranges from about 10^{-17} $\mathrm{m}^{-2/3}$ for "weak" turbulence to about 10^{-13} $\mathrm{m}^{-2/3}$ for "strong" turbulence. The "constant" in refractive index structure constant is a misnomer; C_n^2 actually varies over time and space. Therefore, C_n^2 is also known as the "structure parameter" and is often expressed as a function of altitude or distance from the telescope aperture. C_n^2 is measured using thermal probes or point-to-point laser measurements. Temperature measurements can be made horizontally or over a narrow range of altitude, where pressure fluctuations can be neglected. The refractive index structure constant C_n^2

can thus be related to the temperature structure constant C_T^2 as

$$C_n^2 = \left(79 \times 10^{-6} \frac{P}{T^2}\right)^2 C_T^2 \quad . \tag{2.52}$$

Measurements of C_n^2 have been made at several geographical locations, leading to various analytical models. One that is often used in research is the Hufnagel-Valley model [84:61-62]:

$$C_n^2(h) = 5.94 \times 10^{-53} \left(\frac{v}{27}\right)^2 h^{10} \exp\left(\frac{-h}{1000}\right) + 2.7 \times 10^{-16} \exp\left(\frac{-h}{1500}\right) + A \exp\left(\frac{-h}{100}\right) \quad , \tag{2.53}$$

where A ($\mathrm{m}^{-2/3}$) describes strength of turbulence near the ground, v (m/s) is rms wind speed (5 to 20 km above ground), and h is altitude above sea level (meters). Typically, the free parameters are set to $A = 21$ m/s and $v = 1.7 \times 10^{-14}$ $\mathrm{m}^{-2/3}$, resulting in what is commonly called the H-$V_{5/7}$ model. The 5/7 notation describes the fact that these parameter values were chosen so that at a wavelength of $\lambda = 0.5$ μm, the resulting atmospheric coherence length is $r_0 = 5$ cm and the isoplanatic angle is $\theta_0 = 7$ μrad. Another C_n^2 model widely used in Airborne Laser (ABL) studies is called Clear-1 [20:220]:

$$\log_{10}\{C_n^2(h)\} = \begin{cases} -\infty & h \leq 1.23 \\ -10.7025 - 4.3507h + 0.8141h^2 & 1.23 < h \leq 2.13 \\ -16.2897 + 0.0335h - 0.0134h^2 & 2.13 < h \leq 10.34 \\ -17.0577 - 0.0449h - 0.0005h^2 + 0.6181\alpha(h) & 10.34 < h \leq 30 \end{cases} , \tag{2.54}$$

where h is altitude above mean sea level in km and $\alpha(h)$ is given by

$$\alpha(h) = \exp\left[-0.5\left(\frac{h - 15.5617}{3.4666}\right)^2\right] \quad . \tag{2.55}$$

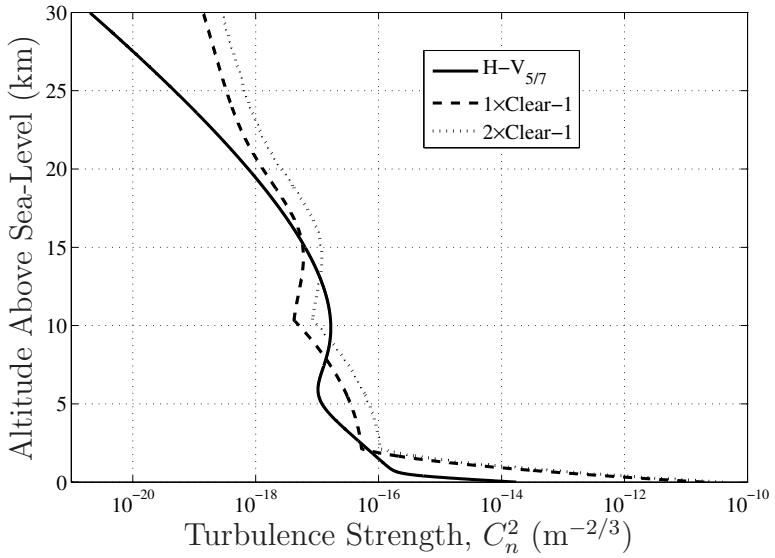

Figure 2.1: Models of turbulence strength as characterized by the refractive index structure parameter, C_n^2 [20, 84].

Note that Clear-1 is based on measurements taken in the New Mexico desert where ground level is 1.216 km. Also, the Clear-1 C_n^2 profile is often multiplied by a constant to model the more challenging turbulence scenarios. The most common approach is to use a factor of two, which yields what is commonly called the "2×Clear-1" model. Using this same notation, the original Clear-1 model given by (2.54) is sometimes called "1×Clear-1" for clarity. H-V$_{5/7}$, 1×Clear-1, and 2×Clear-1 are plotted in Figure 2.1 for altitude ranging from 0 to 30 km above sea-level.

2.2.4 Temporal Statistics. A majority of published material addressing optical turbulence deals with spatial statistics. Temporal statistics are also important as they drive (temporal) bandwidth requirements for real-time compensation systems. Analysis of atmospheric temporal dynamics is greatly simplified via Taylor's "Frozen Flow" hypothesis, which is now summarized [20:174-6].

Two underlying physical processes drive the temporal evolution of atmospheric turbulence. The first is motion of the atmosphere (advection) across the path of interest, and is best visualized by a fixed (Eulerian) frame of reference. The second process is the motion of individual eddies, which is best visualized by a moving (La-

grangian) frame of reference. These internal eddy dynamics would be seen by an observer moving with the flow at the mean rate.

The time constant describing advection of turbulence (τ_{adv}) across the Field of View (FOV) is estimated as

$$\tau_{adv} \approx \frac{L_0}{V_\perp} \quad , \tag{2.56}$$

where L_0 is the outer scale of turbulence and $V_\perp$ is the effective wind velocity perpendicular to the optical axis (due to the atmosphere and/or telescope motion). The time scale of internal eddy dynamics (τ_{int}) is described by

$$\tau_{int} \approx \frac{L_0}{V_{fluc}} \quad , \tag{2.57}$$

where V_{fluc} is the velocity of fluctuations about the mean flow rate. Velocity fluctuations are small compared to the average and can be estimated as 10% of the mean wind speed [20:175]. Temporal evolution of turbulence is therefore assumed to be driven by the mean motion of the atmosphere.

The basic concept resulting from Taylor's hypothesis is that turbulence can be thought of as a relatively frozen phase screen blowing across the telescope FOV. For a turbulence variable depending on both space and time, $\xi(\vec{r}, t)$, Taylor's hypothesis gives the following relationship:

$$\xi(\vec{r}, t + \tau) = \xi(\vec{r} - V_\perp \tau, t) \quad . \tag{2.58}$$

However, applicability of Taylor's hypothesis should be questioned in scenarios where wind is nearly parallel to the observation (propagation) path and the perpendicular component is therefore small.

2.3 Free-Space Propagation

In a linear, dielectric, isotropic, homogeneous, and nondispersive propagation medium, Maxwell's equations yield the scalar wave equation:

$$\nabla^2 U(P,t) - \frac{n^2}{c^2}\frac{\partial^2 U(P,t)}{\partial t^2} = 0 \quad , \tag{2.59}$$

where $k = 2\pi/\lambda$ is the radiation wavenumber, and U represents any component of the electric or magnetic field at a position, P, and time, t. By further assuming the solution to be a monochromatic wave with sinusoidal time variations, (2.59) becomes the time-independent reduced wave equation, also known as the Helmholtz equation:

$$(\nabla^2 + k^2)U(P) = 0 \quad . \tag{2.60}$$

The complex optical field resulting from diffraction by a finite aperture is found by solving (2.60) using the method of Green's functions. The result is a mathematical statement of the Huygens-Fresnel principle:

$$U(P_1) = \frac{1}{j\lambda}\iint_{\Sigma} U(P_0)\frac{\exp(jkr_{01})}{r_{01}}\cos\theta ds \quad , \tag{2.61}$$

where $U(P_0)$ and $U(P_1)$ are the incident and diffracted fields, respectively, θ is the angle between the aperture outward normal, $\hat{n}$, and the vector, $\vec{r}_{01}$, pointing from P_0 to P_1, and Σ defines the surface area of the aperture. Equation (2.61) is a fundamental relationship underlying modern optical scalar diffraction theory.

2.3.1 Fresnel Diffraction Integral. The Huygens-Fresnel principle can be expressed in cartesian coordinates:

$$U(x,y) = \frac{z}{j\lambda}\iint_{\Sigma} U(\xi,\eta)\frac{\exp(jkr_{01})}{r_{01}^2}d\xi d\eta \quad , \tag{2.62}$$

where the magnitude of the vector $\vec{r}_{01}$ is now given by

$$r_{01} = \sqrt{z^2 + (x-\xi)^2 + (y-\eta)^2} \quad . \tag{2.63}$$

Note that (2.62) was obtained by assuming scalar diffraction and that $r_{01} \gg \lambda$. The Fresnel diffraction integral is obtained by making one additional approximation. The binomial expansion of r_{01} is given by

$$r_{01} = z\left[1 + \frac{1}{2}\left(\frac{x-\xi}{z}\right)^2 + \frac{1}{2}\left(\frac{y-\eta}{z}\right)^2 + \cdots\right] \quad . \tag{2.64}$$

The numerator of the integrand of (2.62) is more sensitive to changes in r_{01} than the denominator. Therefore, only the first term of the binomial expansion is used to approximate r_{01} in the denominator, while the first two terms are retained in the numerator. The resulting Fresnel diffraction integral can be expressed as

$$U(x,y) = \frac{e^{jkz}}{j\lambda z} e^{j\frac{k}{2z}(x^2+y^2)} \mathcal{F}\left\{U(\xi,\eta) e^{j\frac{k}{2z}(\xi^2+\eta^2)}\right\}\Big|_{f_{X,Y}=\frac{x,y}{\lambda z}} \quad , \tag{2.65}$$

where $U(\xi,\eta)$ is the original field and $U(x,y)$ is the result of propagating a distance z. The diffracted field is now seen to be a scaled Fourier transform of the product of the original field and a quadratic phase factor.

2.3.2 Angular Spectrum. The propagation of optical fields through homogeneous media can also be formulated as a linear system [42:59-60]. A wave travelling in the positive z direction is described in any plane perpendicular to its path by its angular spectrum, which is simply the Fourier transform of the field with direction cosines substituted for spatial frequency variables. This formulation indicates that any field can be described in terms of a weighted sum of plane waves travelling in various directions. If a field is known at $z = 0$, then the effects of propagation through

the homogeneous media are described by the transfer function of wave propagation:

$$H\left(f_X, f_Y\right) = \begin{cases} \exp\left[j2\pi\frac{z}{\lambda}\sqrt{1-\left(\lambda f_X\right)^2-\left(\lambda f_Y\right)^2}\right] & \sqrt{f_X^2+f_Y^2} < \frac{1}{\lambda} \\ 0 & otherwise, \end{cases} \tag{2.66}$$

where λ is the optical wavelength, z is the propagation distance, and f_X and f_Y are the spatial frequencies in the x and y directions, respectively.

2.3.3 Fresnel Approximation to the Angular Spectrum. The Fresnel approximation to the propagation transfer function applies a binomial expansion and approximation to the exponent of (2.66). The binomial expansion of $\sqrt{1-x}$ is

$$1 - \frac{1}{2}x - \frac{1}{8}x_2 - \frac{1}{16}x_3 - \ldots \quad . \tag{2.67}$$

Using only the first two terms, the exponent is simplified:

$$\sqrt{1-(\lambda f_X)^2-(\lambda f_Y)^2} \approx 1 - \frac{(\lambda f_X)^2}{2} - \frac{(\lambda f_Y)^2}{2} \quad . \tag{2.68}$$

The Fresnel approximation to the angular spectrum propagator is thus [42:71-72]:

$$H\left(f_X, f_Y\right) = \begin{cases} e^{jkz}\exp\left[-j\pi\lambda z\left(f_X^2+f_Y^2\right)\right] & |\lambda f_X| \ll 1 \ \ and \ \ |\lambda f_Y| \ll 1 \\ 0 & otherwise. \end{cases} \tag{2.69}$$

2.4 Propagation Through Turbulence

2.4.1 Analytical Approaches. In turbulent media, propagation is described by the stochastic Helmholtz equation:

$$\left(\nabla^2 + k^2 n^2(\vec{p})\right) U(\vec{p}) = 0 \quad , \tag{2.70}$$

where $n(\vec{p})$ is a random field and an exact solution no longer exists. Several approaches have been taken to solve for statistical moments of the propagated field. The first

to show good agreement with empirical data in the weak fluctuations regime was the Rytov method, which followed the Born method. Both solutions use the method of small perturbations. First was the Born approach, which assumed a solution of the form $U = U_0 + U_1 + U_2 + \cdots$. However, Rytov theory begins by expressing the field as

$$U = e^{\psi} = e^{\chi} e^{iS} \quad , \tag{2.71}$$

where χ is the log-amplitude. The assumed solution is then expanded in terms of ψ:

$$\psi \approx \psi_0 + \psi_1 + \psi_2 + \cdots \quad , \tag{2.72}$$

where ψ_0 is the incident field, ψ_1 is the first-order scattered field, and so forth. The Rytov and Born solutions can be equated, but due to the assumed form, the Rytov solution is applicable under a wider range of conditions.

A third non-perturbation approach uses an extended Huygens-Fresnel theory [5, 20]. In contrast to the Born and Rytov methods, this approach provides a solution in terms of the complete field and allows a linear systems representation. The extended Huygens-Fresnel method has been shown applicable under all conditions of atmospheric turbulence for first and second-order field moments. However, the fourth-order field moment solution has only been shown accurate for weak fluctuations.

A fourth approach is the parabolic equation method [5:114], which is anticipated to be applicable under all conditions. A parabolic differential equation is generated for each statistical moment of the field. Exact solutions have only been derived for first and second-order field moments, and the second-order moment equation has only been solved for plane and spherical originating waves.

To garner final results using any of the above methods, some form of transmitted field must generally be assumed. The earliest solutions were for plane and spherical waves. More recently, Gaussian and other beam-wave shapes have also been studied. Also, the various approaches using perturbation theory share one primary drawback:

they are only valid in weak turbulence conditions. Due especially to the difficulty in deriving solutions applicable under all turbulence conditions, several heuristic approaches have been taken and simulations are often accomplished.

2.4.2 Effects Characterization (Derived Parameters). A plane wave travelling through an atmospheric slab of thickness Δz will experience an optical path difference given by [84:69]

$$\phi_i(\vec{r}) = k \int_{z_i}^{z_i+\Delta z_i} n_1(\vec{r}, z) dz \quad , \tag{2.73}$$

where k is the optical wavenumber, n_1 is the index fluctuation, and $\vec{r}$ is the transverse position vector. Assuming that n_1 is a Gaussian random field allows the transmitted field autocorrelation to be expressed in terms of the phase structure function:

$$\Gamma_{u_t}(\vec{r}) = E\left\{e^{j\phi(\vec{r_1})} e^{-j\phi(\vec{r_1}-\vec{r})}\right\} = e^{-\frac{1}{2}D_\phi(\vec{r})} \quad . \tag{2.74}$$

For a WSS random process, the phase structure function is defined as

$$D_\phi(\vec{r}) = E\left\{[\phi(\vec{r_1}) - \phi(\vec{r_1}+\vec{r})]^2\right\} \quad . \tag{2.75}$$

Substituting (2.73) into (2.75) and simplifying gives [44]

$$D_\phi(\vec{r}) = \frac{1}{3}\frac{6}{5}\frac{\Gamma(1/2)\Gamma(1/6)}{\Gamma(2/3)} k^2 r^{5/3} \int_0^L C_n^2(z) dz \quad , \tag{2.76}$$

where L is propagation path length.

One effect of turbulence on propagation of light is image blurring (beam spread) beyond the diffraction limit. As an example, imagine a plane wave entering the Earth's atmosphere with an arbitrarily large spatial coherence. Propagation through turbulent atmosphere results in degraded spatial coherence in the aperture plane of a collecting telescope. This degradation is characterized by the transverse coherence length defined by the $1/e$ point of the field autocorrelation function. From (2.74), this

definition is equivalent to the separation r which causes the phase structure function to equal two. The resulting separation is given by

$$\rho_0 = \begin{cases} \left[1.46k^2 \int_0^L C_n^2(z)dz\right]^{-3/5}, & l_0 < \rho \leq L_0 \\ \left[1.64k^2 l_0^{-1/3} \int_0^L C_n^2(z)dz\right]^{-1/2}, & \rho \leq l_0 \end{cases} , \tag{2.77}$$

where ρ is magnitude of the radial position vector in the aperture plane, ρ_0 is the separation distance beyond which two points on the wavefront are uncorrelated, l_0 is the inner scale corresponding to the smallest eddy size, L_0 is the outer scale corresponding to the largest eddy size, and k is the optical wavenumber.

A much more common parameter used to describe the effect of turbulence on spatial coherence is the atmospheric coherence length (a.k.a., the Fried parameter), or $r_0 = 2.1\rho_0$. r_0 was defined in 1966 by David Fried to more specifically describe the effect of turbulence on resolution of an incoherent imaging system [34]. For a plane wave, r_0 is given by [84:72]

$$r_0 = 0.185\lambda^{6/5} \left(\int_0^L C_n^2(z)dz \right)^{-3/5} , \tag{2.78}$$

where z is position along the propagation path and λ is optical wavelength. Two key relationships should be noted from (2.78). First, the transverse coherence length (in the inertial range) is proportional to $\lambda^{6/5}$. Therefore, image degradation due to turbulence is somewhat less in the infrared region than in the visible region. Second, r_0 is inversely proportional to the integrated turbulence strength. Since much of the turbulence occurs at lower altitudes, major observatories around the world are built on high mountaintops to effectively reduce the integrated turbulence strength. The corresponding equation for a spherical wave is [84:72]

$$r_0 = 0.185\lambda^{6/5} \left(\int_0^L C_n^2(z) \left[\frac{L-z}{L}\right]^{5/3} dz \right)^{-3/5} , \tag{2.79}$$

where integration is from the pupil (observer) at $z = 0$ to the source located at $z = L$. The integration can also be done from source to observer:

$$r_0 = 0.185\lambda^{6/5} \left(\int_0^L C_n^2(z) \left[\frac{z}{L} \right]^{5/3} dz \right)^{-3/5} \quad . \tag{2.80}$$

When modelling atmospheric turbulence as a set of discrete layers, the Fried parameter is expressed as

$$r_0 = 0.185\lambda^{6/5} \left(\sum_{k=1}^{N} C_{n_i}^2 \frac{L}{N} \right)^{-3/5} \tag{2.81}$$

for a plane wave, and as

$$r_0 = 0.185\lambda^{6/5} \left(\sum_{k=1}^{N} C_{n_i}^2 \left[1 - \frac{k}{N} \right]^{5/3} \frac{L}{N} \right)^{-3/5} \tag{2.82}$$

for a spherical wave, where N is the number of layers. For the case of constant turbulence strength throughout the path, r_0 is given by

$$r_0 = 0.185\lambda^{6/5} \left(LC_n^2 \right)^{-3/5} \quad , \tag{2.83}$$

for a plane wave, and by

$$r_0 = 0.185\lambda^{6/5} \left(\frac{3}{8} LC_n^2 \right)^{-3/5} \quad , \tag{2.84}$$

for a spherical wave. One more note of interest concerning r_0 calculations. The structure parameter is often modelled as being solely a function of altitude, in which case (2.78) becomes [95:34]

$$r_0 = 0.185\lambda^{6/5} \left(\sec(\gamma) \int_0^L C_n^2(h) dh \right)^{-3/5} \quad , \tag{2.85}$$

where γ is the angle from Zenith and h is altitude.

The phase structure function for Kolmogorov turbulence (in the inertial range) can be expressed in terms of r_0 [84:71]:

$$D_\phi(r) = 6.88\left(\frac{r}{r_0}\right)^{5/3} \quad , \tag{2.86}$$

where r is magnitude of the radial position vector in a plane perpendicular to propagation direction and r_0 is calculated for either a plane or spherical wave. The generalized Wiener-Khintchine theorem gives the corresponding Kolmogorov PSD for phase fluctuations:

$$\Phi_\phi(f) = 0.023 r_0^{-5/3} f^{-11/3} \quad , \tag{2.87}$$

where $f = \sqrt{f_X^2 + f_Y^2}$ is spatial frequency in cycles per meter. The following simple relationship can also be used to find the PSD for phase fluctuations from a PSD for index of refraction fluctuations, see Martin [59:467] or Coles, et al. [30:2092]:

$$\Phi_\phi(\vec{K}) = 2\pi k^2 \Delta z \Phi_n(\vec{K}) \quad . \tag{2.88}$$

The PSD for index of refraction fluctuations $\Phi_n(\vec{K})$ is proportional to C_n^2. Therefore, the resulting $\Delta z C_n^2$ term in (2.88) can be replaced by an integral, allowing use of the r_0 equation for simplification. Note the requirement to multiply (2.88) by $(2\pi)^2$ when converting from spatial frequency in radians per meter to cycles per meter in order to maintain the correct area under the PSD surface (i.e., properly account for total energy in the random process).

Several other common forms of the PSD for phase fluctuations are now presented in a form used for later analysis. The modified von Karman spectrum is given by [20]

$$\Phi_\phi(f) = 0.023 r_0^{-5/3} \frac{\exp\left[-1.126(l_0 f)^2\right]}{\left[f^2 + \left(\frac{1}{L_0}\right)^2\right]^{11/6}} \quad , \tag{2.89}$$

where $f = \sqrt{f_X^2 + f_Y^2}$ is again the spatial frequency in cycles per meter, r_0 is the Fried parameter, and L_0 and l_0 are the outer and inner scales, respectively. Finally, the modified spectrum [5] can be expressed as

$$\Phi_\phi(f) = 0.023 r_0^{-5/3} \left[1 + 3.43 l_0 f - 0.538 (l_0 f)^{7/6}\right] \frac{\exp\left[-3.625 (l_0 f)^2\right]}{\left[f^2 + \left(\frac{1}{L_0}\right)^2\right]^{11/6}} \quad . \tag{2.90}$$

2.4.3 Modal Analysis of Perturbed Wavefront. Zernike polynomials have been used to expand the phase of a perturbed wavefront subsequent to propagation through atmospheric turbulence [64]. Such an approach is very useful from two standpoints. First, it provides an analytical tool for predicting the performance of wavefront compensation systems such as AO. Second, it provides a foundation for one of two primary methods used to numerically simulate the random phase distortions introduced by atmospheric turbulence (see Section 2.5.1.2). Noll's analysis also highlights the fact that variations in overall wavefront tilt are the predominant effect of optical turbulence.

Several key relationships resulting from Noll's analysis are now presented, all of which assume the Kolmogorov PSD. First, the aperture averaged mean square wavefront phase is defined as [84:93]

$$\epsilon^2 = \int W(\vec{r}) E\{\phi^2(\vec{r})\} d\vec{r} \quad , \tag{2.91}$$

where $W(\vec{r})$ is the aperture weighting function defined to be zero outside the aperture and normalized within the aperture such that

$$\int W(\vec{r}) d\vec{r} = 1 \quad . \tag{2.92}$$

As first published by Noll, for an uncompensated distorted wavefront (piston removed) the mean square phase within a circular aperture is given by

$$\epsilon^2 = 1.0299 \left(\frac{D}{r_0}\right)^{5/3} \quad , \tag{2.93}$$

where D is the circular aperture diameter and r_0 is the Fried parameter, which is related to turbulence strength. For the sake of brevity, ϵ^2 is often referred to simply as the *mean square phase*. Subsequent to removal of Zernike tip and tilt, the residual mean square phase, ϵ_R^2, is given by

$$\epsilon_R^2 = 0.134 \left(\frac{D}{r_0}\right)^{5/3} \quad . \tag{2.94}$$

Equation (2.94) is used to estimate performance for an ideal tracking scenario. The corresponding expression for a square aperture is

$$\epsilon_R^2 = 0.1748 \left(\frac{L}{r_0}\right)^{5/3} \quad , \tag{2.95}$$

where L is the length of an aperture edge.

2.4.4 Impact on Imaging Systems. Wavefront tilt is the dominant perturbation in any r_0 sized patch; the tilt-removed rms wavefront error is about $\lambda/17$ in an r_0 sized aperture. Therefore, a telescope of diameter r_0 will basically see a diffraction limited image move around the focal plane due to changes in wavefront tilt. r_0 ranges from 5 to 10 cm ($\lambda = 0.5$ μm) at locations near sea-level, to 20 to 30 cm on the best mountaintop astronomical sites. For telescopes with apertures larger than r_0, resolution is effectively limited by the atmospheric coherence length instead of the aperture diameter.

The Modulation Transfer Function (MTF) in the focal plane is given by [35]

$$MTF(\nu) = \exp\left[-3.44(\lambda f \nu / r_0)\right] \quad , \tag{2.96}$$

where f is the focal length of the system and ν is the spatial frequency. The effective MTF of an optical system looking through a turbulent atmosphere is simply the product of the system MTF and the atmospheric MTF. Therefore, turbulence has the effect of low-pass filtering and the elimination of higher frequencies results in image blurring.

2.4.5 Rytov Theory Predictions. As noted in Section 2.4.1, the Rytov approximation led to the first (useful) solutions giving good agreement with actual data. Rytov results are generally accepted as being valid in the weak turbulence regime, normally defined by the value of the Rytov variance [67:201]:

$$\sigma_1^2 = \exp\left\{4\sigma_\chi^2\right\} - 1 = 1.23 C_n^2 k^{7/6} L^{11/6} \quad , \tag{2.97}$$

where $k = 2\pi/\lambda$ is the optical wave number, λ is wavelength, L is propagation distance, and σ_χ^2 is variance of the log-amplitude (see (2.71)). The Rytov variance is the normalized irradiance variance of an unbounded plane wave in weak fluctuations, but is also used as an overall turbulence strength indicator (even outside the realm of weak turbulence). The various regimes of turbulence strength are often defined as follows [5:98]:

- $\sigma_1^2 < 1$, weak fluctuations,
- $\sigma_1^2 \sim 1$, moderate fluctuations,
- $\sigma_1^2 \gg 1$, strong fluctations, and
- $\sigma_1^2 \to \infty$, saturation regime.

The normalized irradiance variance, also called the scintillation index, is defined as

$$\sigma_I^2 = \frac{E\{I^2\} - E\{I\}^2}{E\{I\}^2} \quad , \tag{2.98}$$

where I is the intensity of the optical field.

The Fresnel approximation to the first-order Rytov solutions show that log-amplitude and phase are proportional to a sum of index fluctuations along the propagation path [20:180]. The index fluctuations are considered independent from eddy-to-eddy (layer-to-layer). The index fluctuations are also assumed to be zero-mean, which implies that the phase and log-amplitude means are also zero. Furthermore, the central limit theorem is invoked to predict that both PDFs will be Gaussian. Therefore, the PDFs of phase and log-amplitude are Gaussian while those for amplitude and intensity ($I = e^{2\chi}$) are log-normal.

Rytov results for the covariance, structure function, and 2-D spectrum are now presented for an unbounded plane wave [20:180-181]:

$$B_\zeta(\rho, L) = 4\pi^2 \int_0^L d\eta \int_0^\infty K J_0(K\rho) H_\zeta(L-\eta, K) \Phi_n(K, \eta) dK \quad , \tag{2.99}$$

$$D_\zeta(\rho, L) = 8\pi^2 \int_0^L d\eta \int_0^\infty K[1 - J_0(K\rho)] H_\zeta(L-\eta, K) \Phi_n(K, \eta) dK \quad , \tag{2.100}$$

and

$$F_\zeta(K, 0, L) = 2\pi \int_0^L H_\zeta(L-\eta, K) \Phi_n(K, \eta) d\eta \quad , \tag{2.101}$$

where propagation is from $z = 0$ to L, ρ is the magnitude of the radial position vector, k is the optical wavenumber, K is the three-dimensional spatial wavenumber, η is the variable of integration along the propagation path, and $\Phi_n(K, \eta)$ is the PSD describing index fluctuations. The parameter ζ is used to simplify the equations, and is either χ or S. H_χ and H_S are filter functions that depend on the form of the originating wave, and for a plane wave are given by

$$H_\chi(x, K) = \left\{ k \sin\left[K^2 x/(2k)\right] \right\}^2 \tag{2.102}$$

and

$$H_S(x, K) = \left\{ k \cos\left[K^2 x/(2k)\right] \right\}^2 \quad . \tag{2.103}$$

Returning to the discussion of scintillation statistics, the log-amplitude variance for an infinite plane wave source is expressed in terms of the propagation length by assuming the Komologorov spectrum and evaluating the covariance function (2.99) at $\rho = 0$ [20]:

$$\sigma_\chi^2(L) = \frac{-5\sqrt{3\pi}}{144}\frac{\Gamma(2/3)\Gamma(-5/12)}{\Gamma(11/12)}2^{1/6}k^{7/6}\int_0^L (L-z)^{5/6}\mathrm{C}_n^2(z)\,dz \quad , \tag{2.104}$$

where the source is located at $z = 0$ and the observer is located at $z = L$. The important physical interpretation of (2.104) is that for a given point along the integration path through the atmosphere, the strength of turbulence is weighted by a factor proportional to the remaining distance to the observation point. For a point source, the log-amplitude variance is given by

$$\sigma_\chi^2(L) = \frac{-5\sqrt{3\pi}}{144}\frac{\Gamma(2/3)\Gamma(-5/12)}{\Gamma(11/12)}2^{1/6}k^{7/6}\int_0^L \left[\frac{z(L-z)}{L}\right]^{5/6}\mathrm{C}_n^2(z)\,dz \quad . \tag{2.105}$$

If constant turbulence strength along the propagation path is assumed, simpler forms of the 2-D spectra for log-amplitude and phase result:

$$F_\chi(K,0,L) = \pi k^2 L\{1 - [k/(K^2L)]\sin(K^2L/k)\}\Phi_n(K) \tag{2.106}$$

and

$$F_S(K,0,L) = \pi k^2 L\{1 + [k/(K^2L)]\sin(K^2L/k)\}\Phi_n(K) \quad . \tag{2.107}$$

Plotting the two spectra given by (2.106) and (2.107) provides valuable insight into the cause of phase and log-amplitude fluctuations (see Figure 2.2). The spectral plots highlight two important facts. First, phase fluctuations are more influenced by large scale perturbations. This result basically corroborates the Zernike decomposition analysis described in Section 2.4.3, which indicates that a vast majority of phase perturbation energy is found in the lowest order modes (tip, tilt, etc.). Second, log-amplitude fluctuations are relatively insensitive to large-scale perturbations. The peak

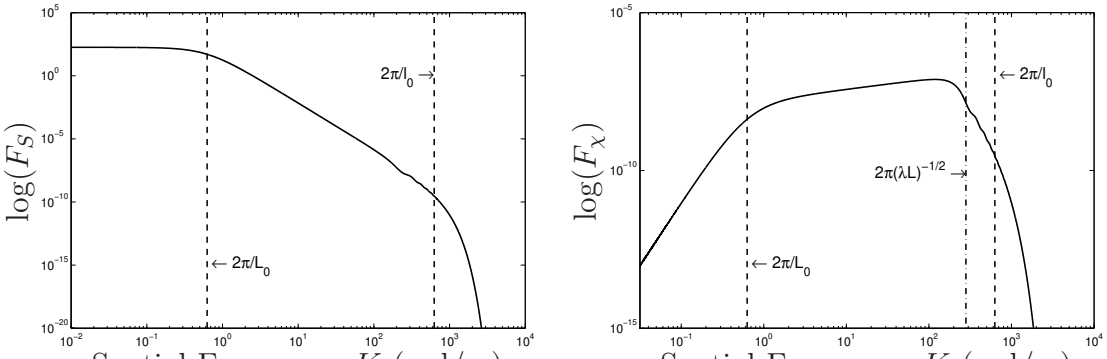

(a) Phase Spectrum of (2.107) (b) Log-Amplitude Spectrum of (2.106)

Figure 2.2: PSDs for phase and log-amplitude fluctuations as predicted by Rytov theory for a constant turbulence strength path. Propagation distance is $L = 1$ km and the wavelength is $\lambda = 0.5$ μm. The modified von Karman atmospheric PSD was used with $L_0 = 10$ m and $l_0 = 1$ cm.

of the spectrum occurs near a spatial frequency corresponding to the Fresnel zone: $2\pi/\sqrt{\lambda L}$. This frequency is 281 rad/m when $L = 1$ km, $\lambda = 0.5$ μm, $L_0 = 10$ m, and $l_0 = 1$ cm.

2.4.6 Probability Density of Irradiance. Considerable work has been done (going back to at least the 1960s) to investigate the PDF form for describing the irradiance of an optical wave subsequent to propagation through atmospheric turbulence. The log-normal PDF, one of the earlier results, is generally accepted as a good model for the weak turbulence regime. A majority of measurement data supports the lower order normalized moments of the irradiance as predicted by the log-normal model under weak turbulence conditions [69, 70]. However, some data also indicates that the log-normal PDF can underestimate the peak and the behavior of the tails [29,49], which can be important for LaserCom and laser radar applications [8:87]. As turbulence strength increases, measurements indicate greater deviations from log-normal statistics [29, 69]. Eventually, the optical wave (amplitude) approaches a zero-mean Gaussian distribution. Therefore, the intensity approaches a negative exponential distribution (far into the saturation regime).

The log-normal distribution for the irradiance results from the Rytov approximation, which implies that the logarithm of both amplitude and irradiance are Gaussian. The log-normal PDF for the irradiance is given by [8:87]

$$p(I) = \frac{1}{I\sigma_I\sqrt{2\pi}} \exp\left[-\frac{\left[\ln(I/E\{I\}) + \sigma_I^2/2\right]^2}{2\sigma_I^2}\right], \quad I > 0 \quad , \tag{2.108}$$

where σ_I^2 is the normalized irradiance variance (a.k.a., the scintillation index) given by (2.98). The normalized irradiance variance is also related to the log-amplitude variance according to [5:113]

$$\sigma_I^2 = \exp\left(4\sigma_\chi^2\right) - 1 \quad . \tag{2.109}$$

Due to the inadequacy of the log-normal model in strong turbulence scenarios, various other PDFs have been investigated, such as the K distribution, the I-K distribution, the log-normally modulated exponential, and the log-normal Rician (a.k.a., Beckmann's PDF). However, all of these PDFs have their own drawbacks. Some are not consistent with measured and simulation data or are only valid in certain regimes. Others such as the Beckmann PDF have displayed a close fit to measured and simulation data, but are difficult to work with. The Beckmann PDF contains an integral with no known closed-form solution and poor convergence properties. Further, the Beckmann PDF contains parameters which cannot be directly related to atmospheric turbulence parameters. Details of these PDFs are not presented here, but are concisely summarized by Al-Habash, et al. [3]. Several authors also published simulation results during the mid-1990s for the PDF of irradiance for plane waves [33] and spherical waves [49] subject to turbulence. The gamma-gamma PDF has been the subject of more recent work by Andrews, Phillips, and Al-Habash [3, 5], and is proposed to be a valid model in all turbulence strengths. Furthermore, the two free parameters of the gamma-gamma model can be calculated from C_n^2, path length (L), and wavelength (λ).

The gamma-gamma PDF is derived from a heuristic model of optical scintillation due to turbulence by assuming an underlying doubly stochastic process. It is assumed that small-scale intensity fluctuations are modulated by large-scale intensity fluctuations, both of which obey independent gamma distributions. The resulting gamma-gamma PDF is given by [8:90]

$$p(I) = \frac{2(\alpha\beta)^{(\alpha+\beta)/2}}{\Gamma(\alpha)\Gamma(\beta)} I^{(\alpha+\beta)/2-1} K_{\alpha-\beta}\left(2\sqrt{\alpha\beta I}\right), \quad I > 0 \quad , \tag{2.110}$$

where the positive parameter α represents the effective number of large-scale scattering cells, β represents the effective number of small-scale cells, and $K_\nu(x)$ is a modified Bessel function of the second kind. The two free parameters can be calculated using either measured or simulated values for C_n^2, path length (L), and wavelength (λ), as shown below. Note also that (2.110) has been normalized so that $E\{I\} = 1$ [8:91]. For a non-unity mean, the gamma-gamma PDF can be expressed as [8:236]

$$p(I) = \frac{2(\alpha\beta)^{(\alpha+\beta)/2}}{\Gamma(\alpha)\Gamma(\beta)E\{I\}} \left(\frac{I}{E\{I\}}\right)^{(\alpha+\beta)/2-1} K_{\alpha-\beta}\left(2\sqrt{\frac{\alpha\beta I}{E\{I\}}}\right), \quad I > 0 \quad . \tag{2.111}$$

For a negligible inner scale (i.e., $l_0 = 0$) and a spherical wave, the large-scale and small-scale variance are given by [7, 9]

$$\sigma_x^2 \cong \exp\left[\frac{0.49\beta_0^2}{\left(1 + 0.56\beta_0^{12/5}\right)^{7/6}}\right] - 1 \tag{2.112}$$

and

$$\sigma_y^2 \cong \exp\left[\frac{0.51\beta_0^2}{\left(1 + 0.69\beta_0^{12/5}\right)^{7/6}}\right] - 1 \quad , \tag{2.113}$$

where $\beta_0^2 = 0.496 C_n^2 k^{7/6} L^{11/6}$ is the spherical wave Rytov variance [67:201]. Accounting for aperture averaging effects from a receiving aperture of diameter D, the

spherical wave large and small-scale variance become [8]

$$\sigma_x^2 \cong \exp\left[\frac{0.49\beta_0^2}{\left(1+0.18d^2+0.56\beta_0^{12/5}\right)^{7/6}}\right]-1 \tag{2.114}$$

and

$$\sigma_y^2 \cong \exp\left[\frac{0.51\beta_0^2\left(1+0.69\beta_0^{12/5}\right)^{-5/6}}{1+0.90d^2+0.62d^2\beta_0^{12/5}}\right]-1 \quad , \tag{2.115}$$

where $d=\sqrt{kD^2/(4L)}$.

From the equations given above for the small and large-scale variance and the equation for the Rytov variance, the two parameters of the gamma-gamma PDF are calculated using

$$\alpha=\frac{1}{\sigma_x^2} \quad , \tag{2.116}$$

and

$$\beta=\frac{1}{\sigma_y^2} \quad . \tag{2.117}$$

The total scintillation index in terms of alpha and beta is now given by

$$\sigma_I^2=\frac{1}{\alpha}+\frac{1}{\beta}+\frac{1}{\alpha\beta} \quad . \tag{2.118}$$

Also, Al-Habash, et al. [3] actually use the gamma-gamma PDF in terms of the natural log of intensity to compare their work with existing simulation data published in the 1990s. Using transformation of a single random variable, where the transformation is one-to-one, the gamma-gamma PDF is expressed in terms of $y=\ln(I)$:

$$p(y)=\frac{2(\alpha\beta)^{(\alpha+\beta)/2}}{\Gamma(\alpha)\Gamma(\beta)}e^{y(\alpha+\beta)/2}K_{\alpha-\beta}[2(\alpha\beta e^y)^{1/2}], \quad y>-\infty \quad . \tag{2.119}$$

2.5 Wave-Optics Simulations

Monte Carlo wave-optics simulations are often used as a tool to analyze existing AO systems, predict the performance of new systems, and/or explore a parameter space in the design. This is due in part to the fact that analytical solutions to the stochastic wave equation are difficult to derive and do not exist for all turbulence regimes. Furthermore, the effects of a closed-loop control system on properties of the optical field compound the difficulties of an analytic approach. Simulations are also desirable from the standpoint that they are much cheaper than building and testing complex AO systems, as well as being much safer when high-energy lasers are involved.

From an optical turbulence standpoint, the atmosphere is typically modelled as one or more discrete 2-D phase-only perturbation layers, or "phase screens," coupled with free-space propagation between layers [84:66-67]. This approach assumes that a continuous atmosphere can be represented by a set of two-dimensional phase screen(s). This yields good results which closely match an extended turbulence analysis, provided the number, location, and relative strengths of the screens are chosen wisely [5]. For some weak turbulence scenarios such as astronomical imaging near zenith, a single phase screen at the pupil can serve as an accurate model because a vast majority of turbulence is located near the telescope (at the end of the propagation path), and thus the effects are primarily phase-only. For stronger turbulence regimes, multiple layers are required to model the amplitude distortions in the optical field that result from phase perturbations followed by significant additional propagation distance. Sampling constraints based on turbulence strength (and the associated diffraction) must also be considered and effectively limit the maximum propagation distance for a given screen size.

Vacuum (free-space) propagation between screens can be accomplished using either geometric or Fourier optics. Geometric optics is a valid approach for some weaker turbulence situations, but does not account for diffraction effects which be-

come increasingly important as strength of turbulence grows. There are several possible implementations of a numeric Fourier optics propagator; the Fresnel diffraction integral and the Fresnel approximation to the angular spectrum propagator are often used. The WaveTrain™ wave-optics code produced by MZA Associates Corporation actually uses both formulations, choosing intelligently between the two depending on propagation distance in order to ease sampling constraints [78].

Temporal evolution of turbulence is traditionally modelled using Taylor's frozen-flow hypothesis, which was discussed in Section 2.2.4. Taylor's hypothesis assumes that a given snapshot of the atmosphere's phase perturbation map remains nearly constant in the time it takes a section of the atmosphere to blow across a telescopes's FOV. Therefore, to model wind or target/platform motion, phase screens are simply shifted laterally during the course of the simulation.

2.5.1 Phase Screen Generation. Two distinct approaches have historically been taken to generate random screen realizations [65:162-164]. The first entails filtering white noise with a known PSD function describing the phase fluctuations. The second utilizes a modal decomposition of the distorted phase; summing randomly weighted modes where coefficients are forced to obey a known covariance (derived from optical turbulence theory). A multitude of variations on these two basic themes have been proposed over the past several decades, with primary goals being to decrease computational complexity and increase the accuracy of a necessarily discrete implementation. Several additional methods, including one based on fractals [65:164], have also been proposed in the literature but have not been implemented. The PSD and modal expansion methods are discussed in detail in Sections 2.5.1.1 and 2.5.1.2, respectively.

2.5.1.1 Power Spectral Density Method. The most straightforward and often used phase screen generation approach is to filter complex white noise with the square root of a PSD describing phase fluctuations. This forces the PSD of the random screen to match the known spectrum [61]. The main advantage of this

method is the speed afforded by the Fast Fourier Transform (FFT) implementation of the Discrete Fourier Transform (DFT); computational complexity is on the order of $N \log N$. Furthermore, the PSD approach is easily modified to use any one of several power spectra describing the phase perturbations. However, there exist at least two important drawbacks. First, phase screen periodicity is induced by use of the DFT, resulting in unwanted correlation between the outer edges. The second is an under-representation of low frequency content. The lowest spatial frequency represented in a given screen is $f_{X_{min}} = 1/N\Delta x$, where N is grid size (pixels) and Δx is sample spacing (meters per pixel). Thus, the minimum modelled frequency is inversely proportional to grid size. These drawbacks are typically countered by: 1) creating larger screens, 2) injecting additional low frequency content subsequent to initial screen generation, or 3) using only a center portion of the original screen. The basic PSD method is now described.

Subsequent to filtering in the spatial frequency domain and taking the inverse transform, the real and imaginary parts of the result represent independent random realizations, given by

$$\phi(x,y) = Re\left[\mathcal{F}^{-1}\left\{\sqrt{\Phi_\phi(f_X,f_Y)}\,[a(f_X,f_Y) + i\,b(f_X,f_Y)]\right\}\right] \quad , \tag{2.120}$$

and

$$\phi(x,y) = Im\left[\mathcal{F}^{-1}\left\{\sqrt{\Phi_\phi(f_X,f_Y)}\,[a(f_X,f_Y) + i\,b(f_X,f_Y)]\right\}\right] \quad , \tag{2.121}$$

where f_X and f_Y are spatial frequencies (m^{-1}) in the x and y directions, respectively, $\Phi_\phi(f_X, f_Y)$ is the power spectrum describing turbulence-induced phase distortions, and a and b are pseudo-random numbers generated from a zero-mean, unit-variance Gaussian distribution. In practice, the FFT is used to enforce this frequency domain constraint due to its computational efficiency. The corresponding discrete version of

(2.120) is

$$\phi(n\Delta x, m\Delta x) = Re\left[\mathrm{FFT}^{-1}\left\{\sqrt{P(l,k)}[a(l,k) + i\,b(l,k)]\right\}\right] \quad , \tag{2.122}$$

where Δx is the phase screen sample spacing, $P(l,k)$ is the power associated with the spatial frequency ($f_X = l\Delta f_X, f_Y = k\Delta f_X$), Δf_X is the sample spacing in Fourier space, m and k are matrix row indices, and n and l are column indices. Use of a square grid is assumed so that $\Delta f_X = \Delta f_Y$. Care must be taken to properly account for the power under the discretized PSD surface; the power associated with each sample in Fourier space is given by

$$P(l,k) = \Phi_\phi(l\Delta f_X, k\Delta f_X){\Delta f_X}^2 \quad . \tag{2.123}$$

The relationship between sample spacing in physical and Fourier space is given by

$$\Delta f_X = \frac{1}{N\Delta x} = \frac{1}{L} \quad , \tag{2.124}$$

where L is the physical extent of the screen and Δf_X is spatial frequency (cycles/meter). Using (2.123), (2.124), and the modified von Karman PSD for optical turbulence given by (2.50), the discrete phase screen is now described by

$$\phi(n,m) = \sqrt{0.023}\left(\frac{L}{r_0}\right)^{5/6} Re\left[\mathrm{FFT}^{-1}\left\{\left[l^2 + k^2 + \left(\frac{L}{L_0}\right)^2\right]^{-11/12} \exp\left[-0.5632\left(\frac{l_0}{L}\right)^2 (l^2+k^2)\right][a(l,k) + i\,b(l,k)]\right\}\right] \quad , \tag{2.125}$$

where the Δx's have been removed from the argument of ϕ to simplify notation. Depending on the particular FFT implementation used to calculate (2.125), multiplication by an additional scaling factor may be required (the MATLAB® $ifft2$ function requires an N^2 factor, where N is the matrix dimension in pixels). Note that use of *complex* white noise is unnecessary, but desirable as it allows generation of twice

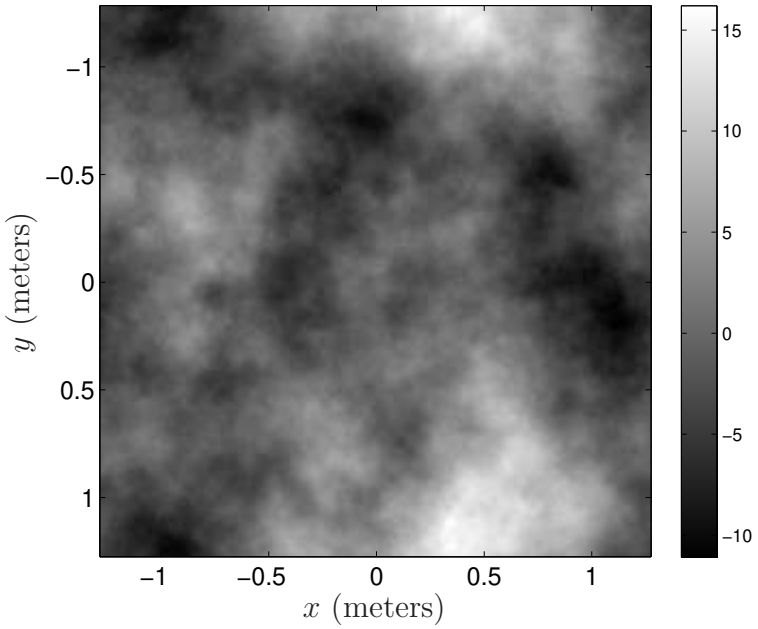

Figure 2.3: One phase screen realization created by filtering white noise with the modified von Karman PSD (typically referred to as the PSD method). The range of image values is in terms of radians. The parameter values used to generate the screen were: $r_0 = 10$ cm, $\Delta x = r_0/10$, $l_0 = 1$ mm, and $L_0 = 100$ m.

the number of screens for a fixed number of FFT operations. A representative screen generated using this process is displayed in Figure 2.3. Also note that Kolmogorov turbulence is self-similar; a given screen can be used to model various turbulence strengths via the $(L/r_0)^{5/6}$ factor.

2.5.1.2 Modal Decomposition/Covariance Methods. The modal expansion method [65, 84] has two main advantages. First, screens generated using this approach do not lack the appropriate low-frequency content. Second, the screens are not periodic. However, several drawbacks do exist. Modelling temporal evolution is less straightforward and computation is significantly less efficient than the PSD method. Truncation error (see Section 2.1.3) also results in a loss of high-frequency content. The basic method is now described.

Optical phase perturbations induced by atmospheric turbulence can be described as a weighted sum of Zernike polynomials (see Sections 2.1.4 and 2.4.3):

$$\phi(R\rho,\theta) \approx \sum_{i=1}^{N} a_i Z_i(\rho,\theta) \quad , \tag{2.126}$$

where N is the number of Zernike modes included and ρ is normalized position ranging from zero to one. Due to the fact that Zernikes are only orthogonal over the unit circle, the following transformation is made to allow implementation with an aperture of arbitrary diameter:

$$r = R\rho \quad , \tag{2.127}$$

where r is absolute position and R is the real aperture radius. Using this transformation, (2.126) becomes

$$\phi(r,\theta) \approx \sum_{i=1}^{N} a_i Z_i\left(\frac{r}{R},\theta\right) \quad . \tag{2.128}$$

To create a random phase screen realization, weighted Zernike modes are summed together. The weights, a_i, are random, but forced to satisfy correlation properties derived from a given PSD describing phase fluctuations due to atmospheric turbulence. Values of the desired covariance matrix derived from the Kolmogorov PSD are given by Noll [64]. However, the formulation of Noll's result as presented by Roggemann and Welsh [84:97-98] was used here, and is given by

$$\begin{aligned} E\{a_i a_j\} = 0.0072 \left(\frac{D}{r_0}\right)^{5/3} (-1)^{(n_i+n_j-2m_i)/2} \left[(n_i+1)(n_j+1)\right]^{1/2} \pi^{8/3} \delta_{m_i m_j} \\ \times \frac{\Gamma(14/3)\Gamma\left[(n_i-n_j-5/3)/2\right]}{\Gamma\left[(n_i-n_j+17/3)/2\right]\Gamma\left[(n_j-n_i+17/3)/2\right]\Gamma\left[(n_i+n_j+23/3)/2\right]} \end{aligned} \tag{2.129}$$

for $i-j = even$, and

$$E\{a_i a_j\} = 0 \tag{2.130}$$

for $i-j = odd$. Cholesky decomposition applied to the above covariance matrix is used to create random instances of the Zernike weight vector, $\mathbf{a}$. First, the covariance

matrix given by (2.129) and (2.130) is generated for the desired number of Zernike modes (excluding piston). The covariance matrix is then decomposed into the product of two square matrices using Cholesky factorization:

$$\mathbf{C} = \mathbf{R}\mathbf{R}^T \quad , \tag{2.131}$$

where T indicates the matrix transpose operator. Finally, the desired random weight vector (with the appropriate statistics) is given by

$$\mathbf{a} = \mathbf{R}\mathbf{b} \quad , \tag{2.132}$$

where $\mathbf{b}$ is a vector of uncorrelated, zero-mean, unit-variance, Gaussian random numbers. Several examples of Zernike phase screens are presented in Figure 2.4. Note the increase in the detail of screen structure as more Zernike modes are included. Phase screen statistics should also approach theoretical predictions with an increasing number of modes.

2.5.2 Phase Screen Validation. Phase screen validation results are now presented for both the PSD and Zernike generation methods. Aperture averaged mean square phase (ϵ^2) versus aperture size and structure function versus separation are often calculated and compared to theory for the purpose of validating discrete phase screens. For the PSD generation method, ϵ^2 is normally calculated for screens where tip and tilt have been removed, because it is known that basic PSD screens are lacking in low-frequency content. Further, these modes are normally removed by a beam steering mirror, while all higher-order modes are corrected by a deformable mirror at the heart of the AO system. 750 screen realizations were used in all cases to estimate both ϵ^2 and the structure function. All PSD phase screen validation results are based on the modified von Karman PSD, while results for the Zernike approach are based on the Kolmogorov PSD. For both methods, the Fried Parameter

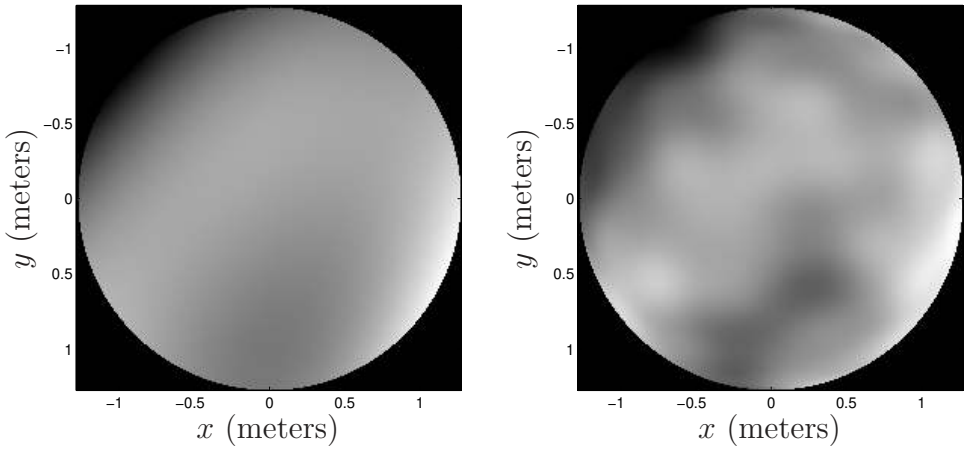

(a) Modes 2 through 10

(b) Modes 2 through 150

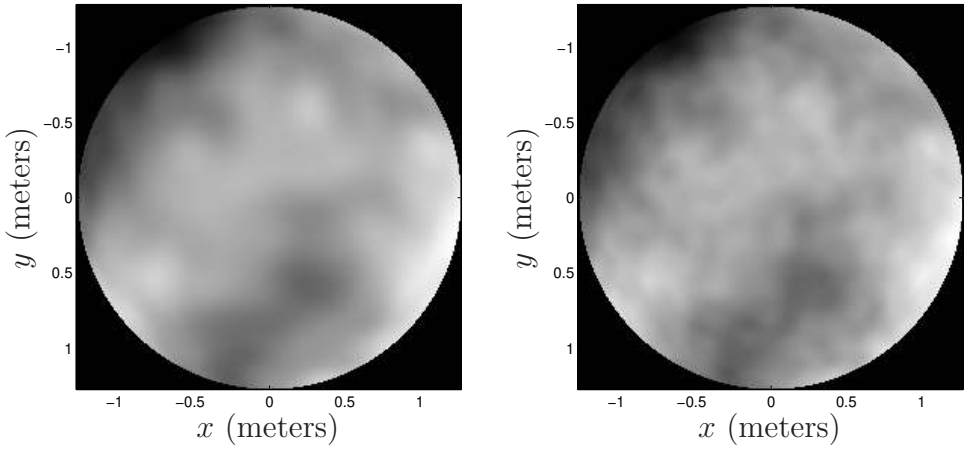

(c) Modes 2 through 300

(d) Modes 2 through 1000

Figure 2.4: Zernike phase screens created using an increasing number of modes, where the modal coefficients obey Kolmogorov statistics. The parameter values used to generate the screens were $r_0 = 10$ cm and $\Delta x = r_0/10$. The same random weight vector realization was used in all cases.

was $r_0 = 10$ cm and sample spacing was $\Delta x = r_0/10$. The PSD screens were generated using an outer scale of $L_0 = 100$ m and an inner scale of $l_0 = 1$ mm.

Theoretical results for the uncompensated (piston-removed) and Zernike tip/tilt-removed mean square phase as a function of D/r_0 were presented in (2.93) and (2.94). Also recall that with the assumption of homogeneous and isotropic conditions the

structure function is given by

$$D_\phi(r) = E\left\{[\phi(\vec{r_1}) - \phi(\vec{r_1} + r)]^2\right\} \quad , \tag{2.133}$$

where r is the scalar displacement. For each screen, the aperture averaged sum square phase was calculated for a set of increasing aperture dimensions by extracting the pixels captured by a given aperture (mask) and calculating their unbiased sample variance. The dynamically sized mask used to extract the desired portion of the phase was odd-dimensioned, such that it was symmetric about the on-axis pixel. For the case of tip/tilt-removed mean square phase, Zernike tip and tilt were also removed via projection for every aperture size. 750 vectors containing variance versus aperture size were thus created, and then averaged to garner a final estimate of ϵ^2. To estimate the structure function, (2.133) was implemented numerically by subtracting a phase screen from a shifted version of itself. The sample mean of the squared difference was then calculated. This was done as a function of an integer number of pixel shifts. The structure function was thus calculated twice for each phase screen, by shifting in the x and y-directions. These two results were then averaged, to obtain an intermediate estimate of the structure function. A series of 2-term averages was calculated for 750 independent screens, then averaged to garner a final structure function estimate. The estimated structure functions are compared to the theoretical curve for Kolmogorov turbulence given by (2.86). Also, the Zernike screens used to estimate statistics were first generated over a circular region. The maximum square matrix inscribed within the aperture was then extracted for estimating the structure function.

PSD screen validation results are presented in Figure 2.5 (a) through Figure 2.5 (f). Figures (b), (d), and (f) are identical to the results of Figures (a), (c), and (e), but are presented in logarithmic space. Figures (a) and (b) present results for uncompensated aperture averaged mean square phase versus D/r_0. This result demonstrates the underrepresentation of low-frequency content (i.e., large separations) in the PSD screens. For the tip/tilt-removed case presented in Figures (c)

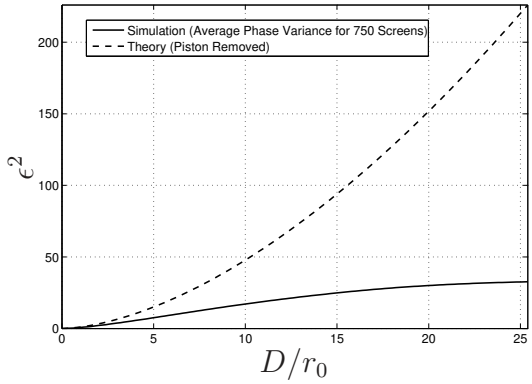

(a) Mean Square Phase

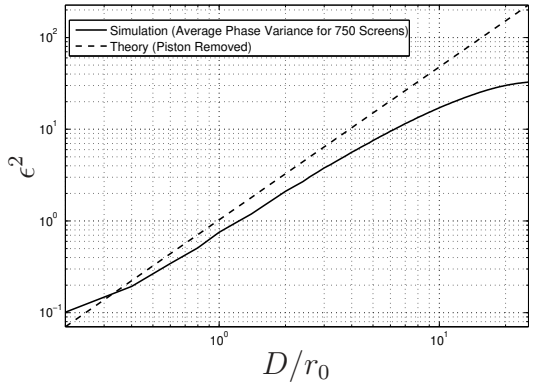

(b) Mean Square Phase (log-log)

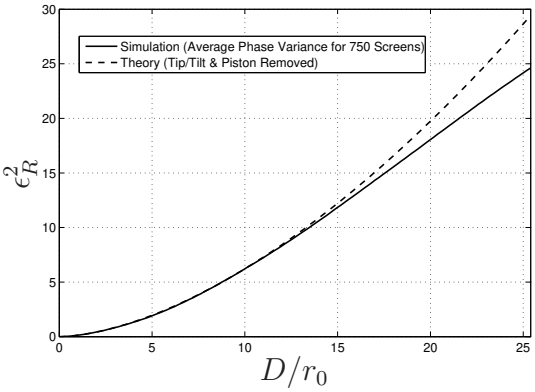

(c) Tip/Tilt-Removed Mean Square Phase

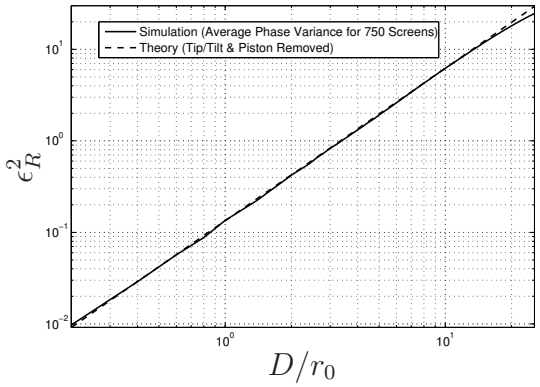

(d) Tip/Tilt-Removed Mean Square Phase (log-log)

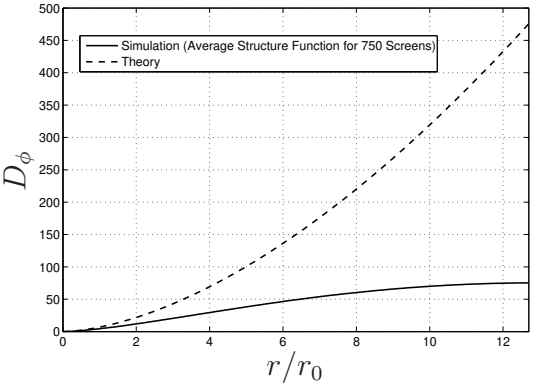

(e) Structure Function

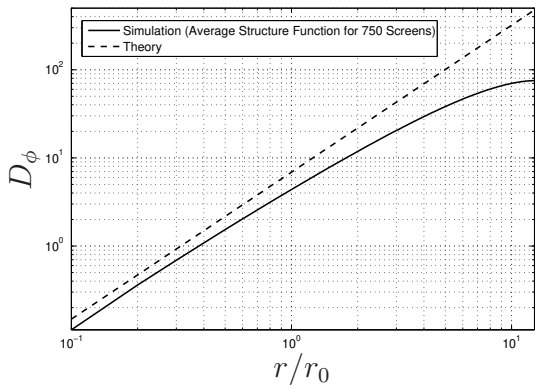

(f) Structure Function (log-log)

Figure 2.5: Mean square phase and structure function estimates vs. theory for PSD phase screens using the modified von Karman PSD ($r_0 = 0.1$ m, $\Delta x = r_0/10$, $L_0 = 100$ m and $l_0 = 1$ mm). 750 phase screen realizations were used to estimate statistics.

and (d) there is a much better match between simulation and theory, although there is some deviation for the largest aperture sizes. This may be due to the period nature of PSD screens. Structure function estimates are presented in Figures (e) and (f). As for the tip/tilt-included mean square phase, there is a considerable discrepancy between simulation and theory. Figure (e) corroborates the result of Lane, Glindemann, and Dainty [56:212]. The discrepancy between simulation and theory at small separation sizes seen in Figure 2.5(f) is probably due primarily to the loss of low-frequency content. The increasing discrepancy (roll-off) at large separations is due to the periodic nature of the FFT, and thus screen statistics. This is why the maximum shift presented for the structure function is half the width of the screen. The other half of the simulation result is simply a mirror image of the result presented in Figures 2.5 (e) and (f).

Zernike screen validation results are presented in Figure 2.6 (a) through Figure 2.6(d). Figures (b) and (d) are identical to the results presented in Figures (a) and (c), but are presented in logarithmic space. Figures 2.6(a) and (b) present results for uncompensated aperture averaged mean square phase versus D/r_0. Simulation results are very close to theory, which demonstrates that the Zernike method properly captures the low-frequency content which is lost in the PSD approach. Structure function estimates are presented in Figures (c) and (d) and closely match the theoretical curve.

As discussed above, one documented reason for the disparity between theory and simulation for PSD screens is the loss of low frequency content due to sampling [56,72]. The lowest frequency in the sampled spectrum to be modelled is $1/L$, where L is the physical width represented by an array of samples. This drawback can be offset to some degree by increasing the number of samples (for a constant spacing), but this increases the computational burden. The Zernike approach provides a much better match with theory, but is more computationally intensive and requires more computer RAM. Extending the Zernike approach to temporal simulation via Taylor's Frozen Flow Hypothesis (see Section 2.2.4) is also less straightforward than for the

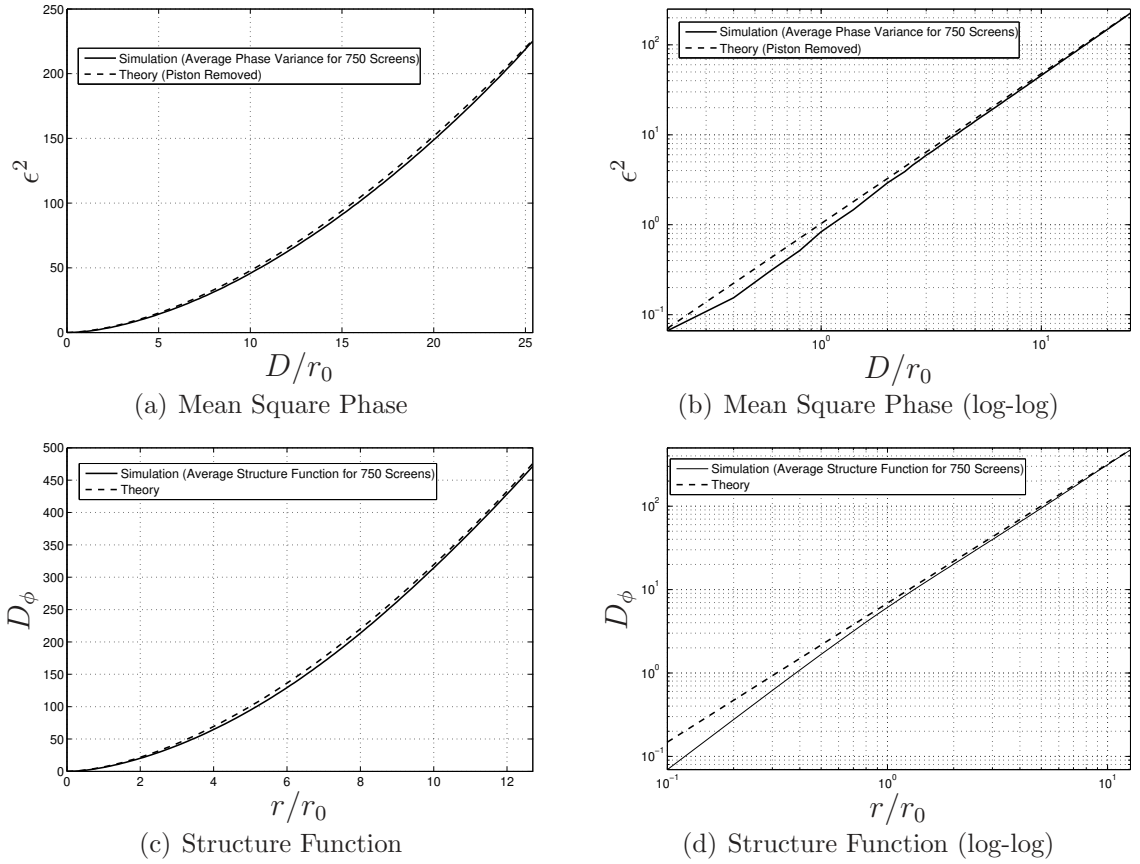

(a) Mean Square Phase

(b) Mean Square Phase (log-log)

(c) Structure Function

(d) Structure Function (log-log)

Figure 2.6: Mean square phase and structure function estimates vs. theory for phase screens created by summing randomly weighted Zernike polynomials 2 through 990, where the random weights obey Kolmogorov statistics ($r_0 = 0.1$ m and $\Delta x = r_0/10$). 750 phase screen realizations were used to estimate statistics.

PSD method. WaveTrain™, a wave-optics simulation software package developed by MZA Associates Corporation, was used during this research effort to produce some key research results presented in Chapters IV through VI. WaveTrain™ uses the PSD method by default, but includes an option which augments power in the tip/tilt Zernike modes. This approach combines, to some extent, benefits of both the PSD and Zernike methods.

III. LaserCom and Adaptive Optics

This chapter provides necessary background on LaserCom and Adaptive Optics (AO). Sections 3.1 through 3.6 address AO, while Sections 3.7 and 3.8 address LaserCom. Section 3.1 provides a brief history of AO and addresses relevance to Air Force applications. Section 3.2 describes a basic AO system applied to imaging. Section 3.3 provides further information on the major subsystems: beacon, Wavefront Sensor (WFS), wavefront computer, and Deformable Mirror (DM). Section 3.4 discusses Strehl ratio - the typical performance metric for AO systems. First, the mathematical relationship between pupil and focal plane fields for monochromatic light is reviewed. Several forms of the Strehl ratio are then defined. Section 3.5 reviews several potential sources of performance degradation: scintillation and branch-points, anisoplanatism, and DM/wavefront fitting error. Section 3.6 describes one type of advanced AO system currently being investigated to improve performance in very challenging atmospheric scenarios. Section 3.7 provides a brief history of LaserCom. Section 3.8 describes digital communication and a basic direct detection LaserCom system. Last, Section 3.9 is a literature review describing relevant current research in wavefront control and signal processing for LaserCom.

3.1 Brief History of Adaptive Optics

Like many ideas realized for the first time in the twentieth century due to technological and manufacturing advances, the concept of AO is not particularly new. Horace Babcock was the first to suggest, in the early 1950s, a system for improved astronomical imaging [10]. His approach used an electrostatically controlled thin layer of oil to introduce corrective phase delays. In 1957 a Russian, Vladimir P. Linnik, independently described the same concept in a Soviet Journal [58]. Several decades later, when the space programs of Russia and the U.S. were in full swing, the DoD took the lead in advancing AO technology. The first fully operational AO system was built and installed in a surveillance telescope at Haleakala Observatory on Maui, Hawaii, for the purpose of imaging Russian satellites launched during the Cold War [94].

Today, AO is an important technology for improving the performance of both military and commercial systems that image or propagate optical sources through the atmosphere. AO is an enabling technology for the multi-billion dollar ABL program [80] and the U.S. government has made a large investment in technology development at several sites: the Starfire Optical Range (SOR) on Kirtland AFB, NM; White Sands Missile Range, NM; and the Air Force Maui Optical and Supercomputing Site (AMOS) in Hawaii. Both SOR and AMOS are capable of capturing near diffraction-limited images of space objects from the ground. Since the unveiling in the early 1990s of classified work accomplished by the DoD, AO technology has also found its way into many astronomical telescopes [65:5]. Newer applications for AO continue to emerge, such as retinal imaging and laser welding [28,39]. AO should also improve the performance of LaserCom systems in many scenarios [57, 96–98, 100].

3.2 Basic AO System for Compensated Imaging

It has long been known that turbulence in the atmosphere distorts images of heavenly bodies as seen from Earth. Operation of a single deformable mirror AO system to compensate for these distortions in real-time is conceptually quite simple. The standard design includes a Beam Steering Mirror (BSM) to correct for global wavefront motion (i.e., phase tilt) and a DM to correct higher-order phase aberrations. The basic AO system for compensated space object imaging is depicted by Figure 3.1. Light waves from a distant star (i.e., point source) are essentially planar as they enter the Earth's atmosphere. Propagating downward, a spatially coherent plane wave encounters pockets of air that vary in temperature and pressure, resulting in slight variations in refractive index. Therefore, different portions of the wavefront are subject to slightly different optical path lengths between the top of the atmosphere and the collecting aperture of a telescope. The distorted phase of the wavefront arriving at the telescope is visualized as being "wrinkled."

The incoming distorted wavefront is captured by the primary mirror, re-imaged onto the beam steering and deformable mirrors, and then passed on to a WFS.

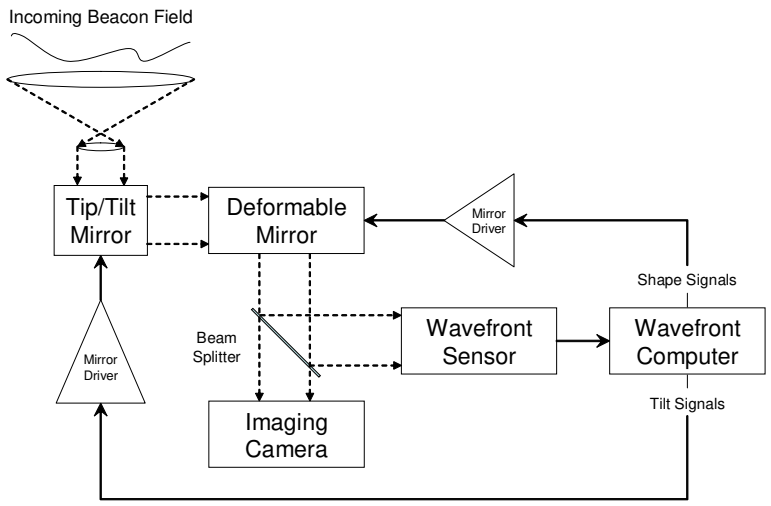

Figure 3.1: Adaptive optics system for compensated space object imaging.

Phase distortions are monitored in real-time by the wavefront sensor. The Shack-Hartmann (S-H) sensor is typically used and actually measures wavefront slopes over an array of sub-apertures. Signals from the WFS are processed and used to control a deformable mirror on a millisecond timescale - leveling the wavefront and increasing spatial coherence. In the case of the S-H WFS, the slope data is passed to a computer that employs an algorithm (such as least-squares) to reconstruct an estimate of the continuous phase, which is then used to provide control commands to the deformable mirror. The wavefront sensor is normally placed "downstream" from the deformable mirror so the control system can perform in a closed-loop fashion. Also, the DM is normally placed downstream from the BSM due to dynamic range limitations of current DM hardware. For observations near zenith the sensed wavefront contains primarily phase-only distortions, and thus nearly diffraction-limited results may be obtained.

3.3 Major AO System Components

As seen in Figure 3.1, the major components required for AO system operation, in addition to a telescope, include a beacon (i.e., reference source), wavefront sensor, (real-time) wavefront computer, deformable mirror, and imaging cameras. A beacon

is required to sense the atmosphere-induced phase distortions. The wavefront sensor provides an estimate of either the field, or the first or second derivative of the wavefront phase. Dedicated real-time computing then processes the WFS measurements and delivers appropriate control signals to the deformable mirror. The deformable mirror imposes the required perturbation to the phase of the incoming field such that the reflected field is approximately planar. A flat tip-tilt mirror, commonly called a beam steering mirror, is also normally included in the system "upstream" from the DM to correct for overall tilt in the distorted wavefront, thus removing what appears as jitter to the human eye. The corrected field is then imaged by science cameras for the purpose of astronomy, satellite surveillance, etc.

3.3.1 Beacon. Beacons come in two basic varieties: natural and man-made [44:70-71]. As might be guessed, a natural beacon simply uses starlight as a reference source. A natural beacon is commonly termed a Natural Guide Star (NGS), and utilizes either direct starlight or sunlight reflected by a satellite to probe the atmosphere. Natural guide stars have several key limitations. First, when using a star as a reference, it must either be the object to be imaged, or be close enough such that correlation exists between the atmosphere along the two lines of sight. A larger angular separation clearly leads to a decrease in correlation of atmospheric fluctuations and performance. De-correlation due to angular separation is mathematically described by the isoplanatic angle, θ_0, which is discussed in Section 3.5. The NGS must also be bright enough to provide sufficient SNR in the WFS. This requirement severely limits the number of stars or satellites that can be imaged using this approach.

Two types of man-made beacons, or Laser Guide Stars (LGS), have been investigated and demonstrated: Rayleigh and sodium. Rayleigh beacons are created by focusing a laser-beam at approximately 15 to 20 km above the Earth. The backscatter (due to Rayleigh scattering) in the visible or Near Infrared (NIR) can be collected and used as a beacon field. The sodium beacon utilizes a layer of atomic sodium located in the upper atmosphere at an altitude of approximately 90 km. A laser source with

a wavelength of $\lambda = 589$ nm can be used to excite the sodium atoms, resulting in resonant fluorescence that is collected by the telescope. Whereas a range of wavelength sources can be used for a Rayleigh beacon, the sodium beacon requires one specific wavelength. One major benefit of a LGS is that it can be positioned at the optimal location in the sky. However, the Rayleigh beacon exists at a relatively low altitude and therefore fails to sense all of the atmospheric fluctuations. Furthermore, the addition of a LGS adds significant complexity to system design.

3.3.2 Wavefront Sensor. Several types of wavefront sensors have been utilized in practice, and several more have been discussed in the literature. The two designs typically seen in actual systems are the Shack-Hartmann and the Shearing Interferometer (SI) WFSs. Both of these designs sense the average wavefront slope in each of an array of subapertures. More recently, the Self-Referencing Interferometer (SRI) WFS has been explored and is expected to outperform both the S-H and SI in strong turbulence (high scintillation) conditions [16–19, 74]. The SRI WFS is currently being investigated both analytically and experimentally by the Air Force Research Laboratory [73, 74]. The primary difference between the SRI WFS and the S-H and SI WFSs is that it provides an estimate of the actual field.

3.3.3 Wavefront Computer and Control Algorithms. High speed Digital Signal Processors (DSPs) are required to analyze the WFS measurements and create appropriate control signals for the phase correcting device. This must be done in near real-time. For the continuous face-sheet DMs typically used in practice, the DM should be commanded with a smooth and continuous function in order to avoid stressing/damaging the mirror. A "reconstructor" algorithm is used to produce an estimate of the continuous phase. A Least-Squares (LS) reconstructor combined with a S-H WFS is the most straightforward and common implementation. The time scale for adjusting the AO system is about r_0/ν, where ν is the wind velocity. A typical value of r_0/ν at visible wavelengths is 30 msec. To sense and remove the turbulence induced phase differences, the AO control system must operate at approximately 10

times the rate of atmosphere change. This implies a system bandwidth of approximately 300 Hz.

3.3.4 Deformable Mirror. This section could also be more generally termed "Phase Correction Devices." However, continuous face-sheet piezo-electric deformable mirrors have been the dominant implementation used in astronomical and military systems. As stated before, the goal of this component is to impart phase changes onto an optical field in order to reverse the effects of atmospheric turbulence. In addition to continuous face-sheet DMs, Micro Electro-Mechanical System (MEMS) mirrors [39] and liquid crystal Spatial Light Modulators (SLMs) [63] have also been investigated and are beginning to receive more attention. The continuous face-sheet deformable mirrors must be protected from being commanded to shapes that are highly abrupt, as they can be damaged by very high spatial frequencies. A beam steering mirror is also typically required due to dynamic range limitations of current DM hardware technology.

3.4 Focal Plane Metrics

3.4.1 Propagation between Pupil and Focal Planes. For coherent light such as a laser, optical fields in the pupil and focal planes are related by a Fourier transform. Following Goodman [42:102-4], the basic development is now presented. The Fresnel diffraction integral is given by

$$U(x,y;z) = \frac{e^{jkz}}{j\lambda z} e^{j\frac{k}{2z}\left(x^2+y^2\right)} \iint_{-\infty}^{\infty} \left\{ U(\xi,\eta) e^{j\frac{k}{2z}\left(\xi^2+\eta^2\right)} \right\} e^{-j\frac{2\pi}{\lambda z}(x\xi+y\eta)} d\xi d\eta \quad , \tag{3.1}$$

where (ξ,η) are coordinates in the pupil plane and (x,y) are coordinates in the focal plane. Assuming the more general case of strong turbulence, monochromatic light incident on the telescope aperture can be described by

$$U_l(\xi,\eta) = A(\xi,\eta) e^{j\phi_a(\xi,\eta)} \quad . \tag{3.2}$$

Making the typical paraxial approximation allows the phase transformation imparted by a converging lens to be described as

$$t_l(\xi,\eta) = e^{-j\frac{k}{2f}\left(\xi^2+\eta^2\right)} \quad . \tag{3.3}$$

The complex amplitude distribution behind the lens is now given by

$$U_l'(\xi,\eta) = A(\xi,\eta)e^{j\phi_a(\xi,\eta)}P(\xi,\eta)e^{-j\frac{k}{2f}\left(\xi^2+\eta^2\right)} \quad , \tag{3.4}$$

where $P(\xi,\eta)$ defines the aperture area. Propagation of the incoming field from the pupil plane to the focal plane is now described using Fresnel diffraction:

$$U_f(x,y) = \frac{e^{jkf}}{j\lambda f}e^{j\frac{k}{2f}\left(x^2+y^2\right)} \iint_{-\infty}^{\infty} \left\{U_l'(\xi,\eta)e^{j\frac{k}{2f}\left(\xi^2+\eta^2\right)}\right\} e^{-j\frac{2\pi}{\lambda f}(x\xi+y\eta)}d\xi d\eta \quad . \tag{3.5}$$

Substituting (3.4) for U_l' gives

$$\begin{aligned} U_f(x,y) = {} & \frac{e^{jkf}}{j\lambda f}e^{j\frac{k}{2f}\left(x^2+y^2\right)} \\ & \times \iint_{-\infty}^{\infty} \left\{A(\xi,\eta)e^{j\phi_a(\xi,\eta)}P(\xi,\eta)e^{-j\frac{k}{2f}\left(\xi^2+\eta^2\right)}e^{j\frac{k}{2f}\left(\xi^2+\eta^2\right)}\right\} e^{-j\frac{2\pi}{\lambda f}(x\xi+y\eta)}d\xi d\eta \quad . \end{aligned} \tag{3.6}$$

The two quadratic phase factors in the integrand of (3.6) exactly cancel, leaving

$$U_f(x,y) = \frac{e^{jkf}}{j\lambda f}e^{j\frac{k}{2f}\left(x^2+y^2\right)} \iint_{-\infty}^{\infty} \left\{A(\xi,\eta)e^{j\phi_a(\xi,\eta)}P(\xi,\eta)\right\} e^{-j\frac{2\pi}{\lambda f}(x\xi+y\eta)}d\xi d\eta \quad . \tag{3.7}$$

The focal plane field is now seen to be the two-dimensional Fourier transform of that part of the incoming field captured by the pupil (aperture), with some additional phase factors out front. Using operator notation for the Fourier transform gives a

more compact expression:

$$U_f(x,y) = \frac{e^{jkf}}{j\lambda f} e^{j\frac{k}{2f}\left(x^2+y^2\right)} \mathcal{F}\left\{A(\xi,\eta)e^{j\phi_a(\xi,\eta)}P(\xi,\eta)\right\}|_{f_{X,Y}=\frac{x,y}{\lambda f}} \quad . \tag{3.8}$$

The field intensity is the quantity of interest because it can be directly measured. The instantaneous focal plane intensity is described as

$$\begin{aligned} I_f(x,y) &= U_f(x,y)U_f^*(x,y) = |U_f(x,y)|^2 & (3.9)\\ &= \frac{1}{\lambda^2 f^2}\left|\iint_{-\infty}^{\infty}\left\{A(\xi,\eta)e^{j\phi_a(\xi,\eta)}P(\xi,\eta)\right\}e^{-j\frac{2\pi}{\lambda f}(x\xi+y\eta)}d\xi d\eta\right|^2 & (3.10)\\ &= \frac{1}{\lambda^2 f^2}\left|\mathcal{F}\left\{A(\xi,\eta)e^{j\phi_a(\xi,\eta)}P(\xi,\eta)\right\}|_{f_{X,Y}=\frac{x,y}{\lambda f}}\right|^2 \quad . & (3.11) \end{aligned}$$

3.4.2 Strehl Ratio. The metric typically used to assess performance of AO systems is the Strehl ratio, which is defined as the on-axis intensity in the focal plane (i.e., far-field) produced by the aberrated system divided by the on-axis intensity for the unaberrated (diffraction-limited) case:

$$S = \frac{I_f(0,0)}{I_{f,DL}(0,0)} \quad . \tag{3.12}$$

Using (3.10), the Strehl ratio becomes

$$\begin{aligned} S &= \frac{\frac{1}{\lambda^2 f^2}\left|\iint_{-\infty}^{\infty}\left\{A(\xi,\eta)e^{j\phi_a(\xi,\eta)}P(\xi,\eta)\right\}e^{-j\cdot 0}d\xi d\eta\right|^2}{\frac{1}{\lambda^2 f^2}\left|\iint_{-\infty}^{\infty}\left\{A_0(\xi,\eta)P(\xi,\eta)\right\}e^{-j\cdot 0}d\xi d\eta\right|^2} & (3.13)\\ &= \frac{\left|\iint_{-\infty}^{\infty}A(\xi,\eta)e^{j\phi_a(\xi,\eta)}P(\xi,\eta)d\xi d\eta\right|^2}{\left|\iint_{-\infty}^{\infty}A_0(\xi,\eta)P(\xi,\eta)d\xi d\eta\right|^2} \quad , & (3.14) \end{aligned}$$

where $A_0(\xi,\eta)$ is the amplitude profile resulting from vacuum propagation. For a single DM AO system applying a single phase modulation in the pupil plane, the

"corrected" Strehl is given by

$$S = \frac{\left| \iint_{-\infty}^{\infty} A(\xi,\eta) e^{j[\phi_a(\xi,\eta)+\phi_c(\xi,\eta)]} P(\xi,\eta) d\xi d\eta \right|^2}{\left| \iint_{-\infty}^{\infty} A_0(\xi,\eta) P(\xi,\eta) d\xi d\eta \right|^2} \quad , \tag{3.15}$$

where $\phi_c(\xi,\eta)$ represents the phase correction imparted by the deformable mirror (or other device).

For this research, two forms of Strehl ratio are defined: absolute Strehl (S_A) and relative Strehl (S_R). Absolute Strehl is defined to be the result given by (3.14), and is repeated here:

$$S_A = \frac{\left| \iint_{-\infty}^{\infty} A(\xi,\eta) e^{j\phi_a(\xi,\eta)} P(\xi,\eta) d\xi d\eta \right|^2}{\left| \iint_{-\infty}^{\infty} A_0(\xi,\eta) P(\xi,\eta) d\xi d\eta \right|^2} \quad . \tag{3.16}$$

The term *absolute* is indicative of the fact that the denominator of (3.16) provides a constant normalization; the power in $A_0(\xi,\eta)$ depends only on vacuum propagation parameters. Relative Strehl is defined to be the value of on-axis intensity in the far-field, normalized by the on-axis intensity for a uniform phase with the same amplitude profile:

$$S_R = \frac{\left| \iint_{-\infty}^{\infty} A(\xi,\eta) e^{j\phi_a(\xi,\eta)} P(\xi,\eta) d\xi d\eta \right|^2}{\left| \iint_{-\infty}^{\infty} A(\xi,\eta) P(\xi,\eta) d\xi d\eta \right|^2} \quad . \tag{3.17}$$

The term *relative* is indicative of the fact that the denominator of (3.17) provides a relative normalization; the total power in $A(\xi,\eta)$ varies due to scintillation. Therefore, S_R provides a measure of improvement relative to the total power currently captured by the aperture. Also note that (3.17) is sometimes referred to as the "phasor sum Strehl."

3.4.3 Power-in-the-Bucket. For some applications, it may be useful to consider the energy captured by a disk of given radius in the focal plane. This metric is typically called either "Encircled Strehl" or "Power-in-the-Bucket" (PIB) [95], and can be expressed as

$$PIB = \frac{\iint\limits_{\sqrt{x^2+y^2}\leq R} I_f(x,y)dxdy}{\iint\limits_{\sqrt{x^2+y^2}\leq R} I_{f,DL}(x,y)dxdy} \quad , \tag{3.18}$$

where R is the radius of the circular area of interest in the focal plane, centered on the optical axis.

3.5 Error Sources (Partial List)

3.5.1 Scintillation. Strong turbulence conditions result in temporal and spatial fluctuations in the intensity of the received optical field. The characterization of these fluctuations is discussed in Chapter II. Scintillation causes problems for AO systems. As an example, a drop in intensity on some of the wavefront sensor subapertures can lead to phase estimation errors. These errors may propagate through the system causing the closed-loop control system to become unstable. Scintillation can also cause problems with tracking. Branch points are related to scintillation and WFS performance, and are discussed in greater detail in the following section.

3.5.2 Branch Points. Wavefront sensors in use today typically provide data that indirectly describes the wavefront phase. In the case of the Shack-Hartmann and shearing interferometer sensors, quantities proportional to wavefront slopes are obtained. The slopes are related to the phases by

$$\mathbf{g} = \mathbf{G}\phi \quad , \tag{3.19}$$

where $\mathbf{g}$ is a vector of wavefront phase differences, ϕ is a vector of actual phase values (or DM actuator positions), and $\mathbf{G}$ is a matrix describing the geometric configuration of wavefront sensor and phase determination positions [95:258]. In a closed-loop

implementation accounting for the effect of a deformable mirror, $\mathbf{G}$ is often referred to as the *influence* or *poke* matrix. Typically, there are more equations than unknowns yielding an overdetermined system. The least-squares estimate for the phase is then given by

$$\hat{\phi} = (\mathbf{G}^T\mathbf{G})^{-1}\mathbf{G}^{\mathbf{T}}\mathbf{g} \quad . \tag{3.20}$$

Propagation of a coherent monochromatic optical field through a turbulent atmosphere (where the field is subject to spatially varying phase perturbations) results in constructive and destructive interference in the amplitude (intensity) of the field. Locations in the optical field where amplitude goes to zero indicate the presence of a Branch Point (BP). In practice, BPs are located by summing the principal value gradients around the smallest possible closed contour [40], where the principal value operator $PV\{\cdot\}$ produces an equivalent phase in the range $-\pi$ to π. If a BP is enclosed, then the contour integral of principal value phase gradients equals $\pm 2\pi$. Likewise, if a BP is not enclosed, the contour integral equals zero. The LS estimator for the phase does not correctly reconstruct the phase if BPs are present, because it assumes that measured slopes are indicative of the gradient of a scalar phase function. Actually, the function describing the gradient of the perturbed phase must be treated as the sum of the gradient of a scalar potential and the curl of a vector potential [37, 40]:

$$g(\vec{r}) = \nabla s(\vec{r}) + \nabla \times \vec{H}(\vec{r}) \quad , \tag{3.21}$$

where $\vec{r}$ is a position vector of x and y components, $s(\vec{r})$ is a scalar potential, and $\vec{H}(\vec{r})$ is a vector potential. Since $g(\vec{r})$ only has components in the x and y directions, $\vec{H}(\vec{r})$ clearly has non-zero components only in the z direction. In going from a discrete space to a continuous formulation, the $\mathbf{G}$ matrix above can be equated to the gradient operator (∇), $\mathbf{G}^T$ can be equated to the divergence operator ($\nabla\cdot$), and $\mathbf{G}^T\mathbf{G}$ can be equated to the Laplacian operator (∇^2) [37]. A continuous formulation allows additional insight into the operation of the LS reconstructor. Equation (3.20)

describing the LS estimate is recast in a continuous space formulation as

$$\nabla^2\hat{\phi}(\vec{r}) = \nabla \cdot [\nabla s(\vec{r}) + \nabla \times \vec{H}(\vec{r})] \quad . \tag{3.22}$$

Recall the vector identity stating that the divergence of the curl of a vector is equal to zero [91], and (3.22) becomes

$$\nabla^2\hat{\phi}(\vec{r}) = \nabla \cdot [\nabla s(\vec{r})] \quad , \tag{3.23}$$

which indicates that the LS estimate for the phase has completely ignored the contribution from the vector potential. The actual phase can now be defined as

$$\phi(\vec{r}) = \phi_{LS}(\vec{r}) + \phi_{HID}(\vec{r}) \quad , \tag{3.24}$$

where $\phi_{HID}(\vec{r})$ is the "hidden" phase unaccounted for in the LS reconstruction [37,73].

The intensity and principal value (i.e., wrapped) phase of one scintillated pupil plane field are displayed in Figures 3.2(a) and 3.2(b), respectively. The image values in Figure 3.2(a) are in terms of irradiance (watts/m^2). The field contains three branch points whose locations are indicated in Figure 3.2(b). An open square indicates a positive BP where the contour integral yields a value near 2π, while the open circle indicates a negative BP corresponding to a contour integral value near -2π. This example was produced in a wave-optics simulation supporting research for Chapters IV and V. The scenario is a 100 km path with a constant turbulence strength of $C_n^2 = 2 \times 10^{-17}$ m$^{-2/3}$ and a 10 m/s uniform crosswind. The optical wavelength is 1.5 μm and the log-amplitude variance for this case is $\sigma_\chi^2 = 0.19$. Note that all branch points are located in regions of low intensity. The focal plane intensity corresponding to this pupil plane field is displayed in Figure 3.2(c). The focal plane image is broken into two separate spots, both near in size to the Airy disk. This example of spot breakup is a preview of important results in Chapters IV and V.

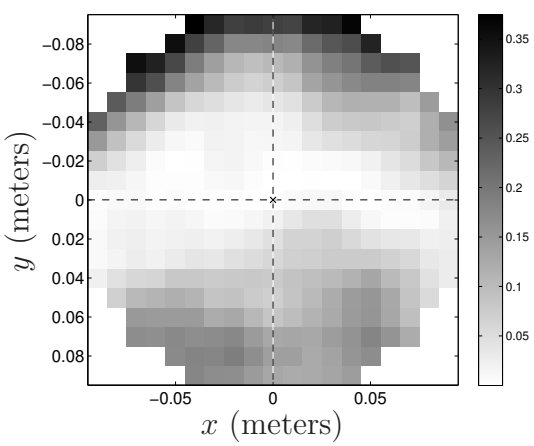

(a) Pupil plane intensity

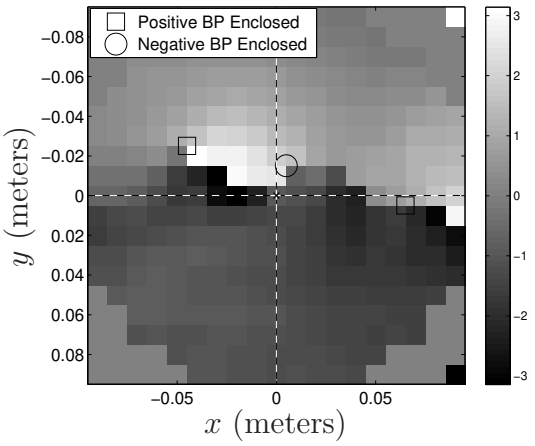

(b) Pupil plane phase (wrapped)

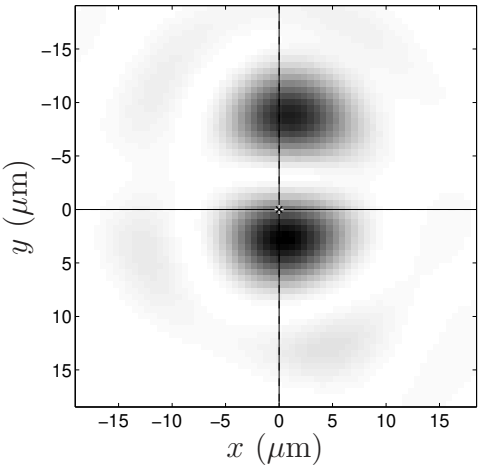

(c) Focal plane intensity

Figure 3.2: A scintillated pupil plane field example generated in wave-optics simulation which contains three branch points. Pupil plane intensity is plotted in (a), while pupil plane principal value phase is plotted in (b). The corresponding focal plane intensity is presented in (c). The scenario is a 100 km path with a 10 m/s uniform crosswind at a wavelength of 1.5 μm. The turbulence strength is a constant $C_n^2 = 2 \times 10^{-17}$ m$^{-2/3}$.

The LS and hidden components of the phase according to (3.24) are plotted in Figure 3.3. Figure 3.3(a) shows the LS reconstruction of the phase; this surface is a form that is realizable by a continuous face-sheet deformable mirror. The hidden phase (containing branch points) is displayed in Figure 3.3(b) and contains abrupt changes that are difficult for a continuous face-sheet deformable mirror to realize in

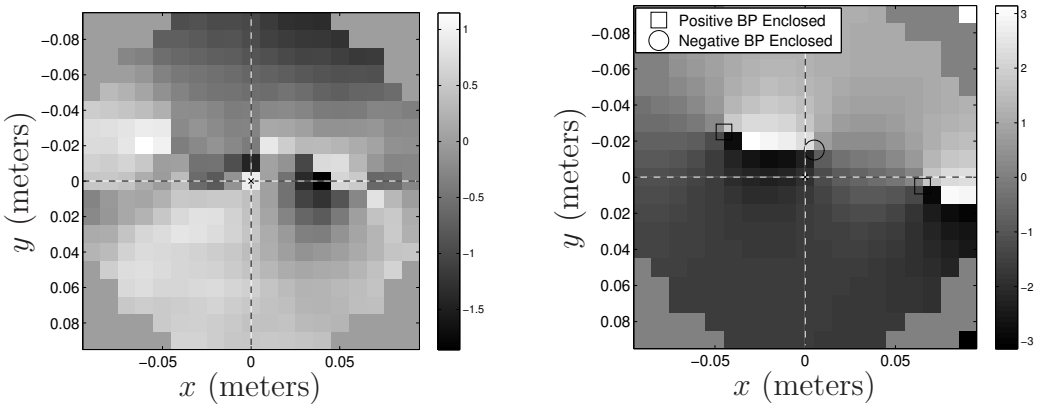

(a) Least-squares unwrapped phase (b) Hidden phase (wrapped)

Figure 3.3: The LS and hidden portions of the scintillated phase profile presented in Figure 3.2. The scenario is a 100 km path with a 10 m/s uniform crosswind at a wavelength of 1.5 μm. The turbulence strength is a constant $C_n^2 = 2 \times 10^{-17}$ m$^{-2/3}$ and log-amplitude variance is $\sigma_\chi^2 = 0.19$.

practice. Note that no BPs were observed in wave-optics simulation data generated for the results of Chapters IV and V when C_n^2 was less than 2×10^{-17} m$^{-2/3}$.

3.5.3 Anisoplanatism. Anisoplanatism is used to describe a series of potential error sources for AO systems. In general, the word anisoplanatism is used to describe errors resulting from a difference or nonuniformity in a parameter. The Greenwood frequency describes the temporal effect of finite correction system bandwidth [44:337-339]:

$$f_G = \left[0.102k^2 \int_0^L C_n^2(z) v_w^{5/3}(z) dz\right]^{3/5} \quad , \tag{3.25}$$

where $v_w(z)$ is wind velocity as a function of path position and integration is from observer to source. For typical scenarios of interest, f_G is in the range of tens to hundreds of Hz [95:44]. In terms of the typical aperture averaged mean square phase error metric, the impact of Greenwood frequency is modelled as [99:25]

$$\epsilon^2_{\text{temporal}} = \left(\frac{f_G}{f_{3dB}}\right)^{3/5} \quad , \tag{3.26}$$

where f_{3dB} is the closed-loop control bandwidth. A rule of thumb for determining bandwidth requirements for an AO system is described below [104]:

1. Calculate f_G,
2. Assume AO system bandwidth is $\approx 2 \times f_G$ (Strehl ≈ 0.7), and
3. Sample at about $10 \times$ the AO system bandwidth for loop stability.

Another anisoplanatic error is introduced when the AO beacon and the imaging object (or propagation target) of interest are not the same and separated by a finite angle. The isoplanatic angle is used to describe this effect and is given by [36]

$$\theta_0 = \left[2\sqrt{\pi} \frac{\Gamma(1/6)}{5\Gamma(2/3)} k^2 \int_0^L C_n^2(z) z^{5/3} dz \right]^{-3/5} \quad , \tag{3.27}$$

where z is path position and integration is from observer to source. θ_0 is the approximate angle beyond which the optical turbulence becomes uncorrelated. The mean square phase error due to angular anisoplanatism can be expressed as [44]

$$\epsilon^2_{\text{angular}} = \left(\frac{\theta}{\theta_0} \right)^{5/3} \quad , \tag{3.28}$$

Additional errors can also be described in this fashion, such as tilt, focus, and chromatic anisoplanatism [44].

3.5.4 Wavefront Measurement and Fitting Errors. For an N degree-of-freedom deformable mirror, the greatest reduction in mean square wavefront error is achieved by fully compensating the first N Karhunen-Loeve modes. However, given a real DM with finite actuator spacing and dynamic range, there will be some residual error between the actual wavefront and mirror surface. Hudgin analyzed the error between a LS fit and Kolmogorov turbulence for several different forms of the influence function [53]. His result for the wavefront error variance after correction is given by

$$\epsilon^2_{\text{fitting}} = \alpha \left(\frac{r_s}{r_0} \right)^{5/3} \quad , \tag{3.29}$$

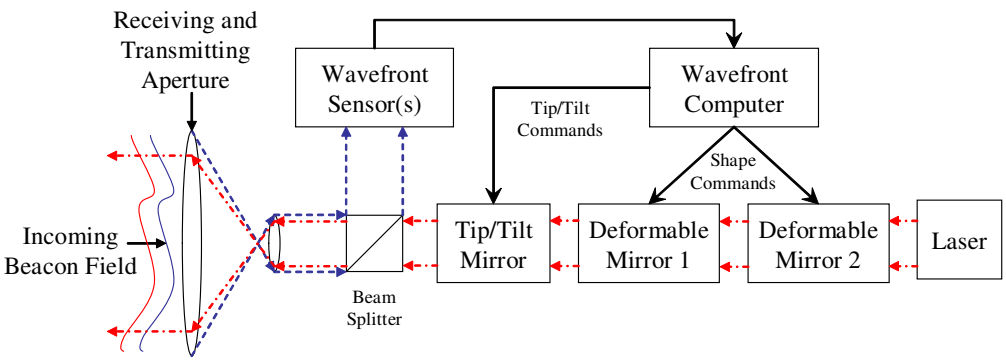

Figure 3.4: Example of an advanced AO system, where two DMs are used to correct both amplitude and phase distortions.

where r_s is the actuator spacing, r_0 is the atmospheric coherence length (Fried parameter), and α depends on the form of the influence function. Published values include $\alpha = 0.23$ for a Gaussian influence function and $\alpha = 1.26$ for piston-only control [95:71].

Likewise, error is introduced from the WFS due to a finite number of subapertures. In other words, the wavefront is more accurately measured as the number of subapertures increases. In terms of mean square phase error, this degradation is modelled by [99:30]

$$\epsilon^2_{\text{WFS}} = 0.17 \left(\frac{d_{sub}}{r_0} \right)^{5/3} \quad , \tag{3.30}$$

where d_{sub} is the subaperture size and all subapertures are of equal dimension.

3.6 Advanced AO Concepts

The addition of a second deformable mirror to a transmitting system, as shown in Figure 3.4, allows pursuit of full-wave conjugation. This concept is often referred to as Multi-Conjugate Adaptive Optics (MCAO). Wave conjugation is achieved by taking advantage of the fact that phase modulation followed by propagation results in changes to the field amplitude distribution. By employing a phase-retrieval type algorithm, the second deformable mirror can be driven to a shape that results in an amplitude field equal to that of the sensed field after propagation of a laser from DM-2 to DM-1.

A two-DM AO system with the second deformable mirror conjugate to infinity (i.e., the far-field) was studied by Roggemann and Lee and shown to provide an increase in on-axis field amplitude at the target by a factor of 1.4 to 1.5, as compared with a one-DM phase-only correction system [83]. Additional investigations of the MCAO concept have been accomplished by Barchers, Ellerbroek, Fried, and Link [11–15].

3.7 Brief History of LaserCom

Best known for the telephone, Alexander Graham Bell also invented optical wireless communication. Bell actually viewed the "photophone" (see Figure 3.5) as his most important invention, saying [1] "It's the greatest invention I have ever made; greater than the telephone!" Dr. Bell was the sole owner of 18 patents and shared 12 more with collaborators; of these 30, four were for the photophone [21–24]. His device first demonstrated wireless communication on 3 Jun 1880 using intensity (analog) modulated sunlight. The following year, Dr. Bell and his assistant, Charles Sumner Tainter, used the photophone to successfully transmit the human voice through approximately 200 m of free-space [1].

Bell's invention was a precursor to modern fiber optic and LaserCom systems. However, the photophone was highly susceptible to the weather, given that sunlight was used as the source and no compensation techniques were implemented to combat

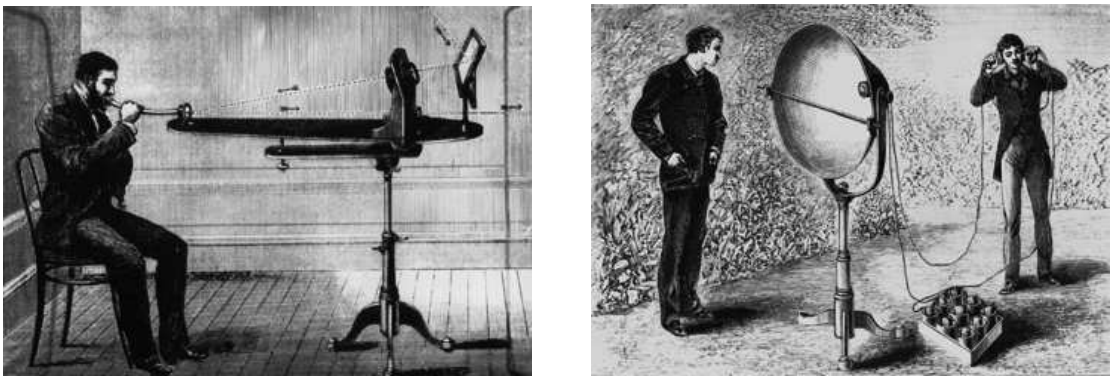

Figure 3.5: Illustrations of Alexander Graham Bell's photophone transmitter (left) and receiver (right) (courtesy of the Bell-Labs website).

Table 3.1: Pros and cons of a LaserCom system.

Challenges	**Advantages**
Atmospheric turbulence, absorption, and scattering	More compact (e.g., smaller antenna) and lighter weight components
Acquisition, tracking, and pointing are more difficult	Increased security via narrow beam
Building sway and seismic activity	Increased bandwidth/data-rate
Physical obstructions	Rapid deployment
Fog, clouds, rain	No FCC and construction licenses/fees

challenges such as poor weather and atmospheric turbulence. The advent of fiber optics overcame virtually all of the environmental drawbacks to Bell's original design - optical fiber communication is immune to adverse weather and electro-magnetic interference. However, fiber optics has some of its own drawbacks. Many of these are addressed in a complementary fashion by free-space LaserCom. A summary of pros and cons of free-space LaserCom is presented in Table 3.1 [8:201-203].

Today, LaserCom is envisioned as a value-added tool in the overall communication network for both commercial and military applications: a rapidly deployable, high-bandwidth, line-of-sight connection. In fact, commercial LaserCom components were installed within days of the terrorist attack on the World Trade Center, successfully re-establishing high-speed data links used by Merrill Lynch Brokerage [54]. In this case, LaserCom demonstrated its potential to temporarily patch a high-speed connection, but it is also being developed and utilized for permanent connections. Commercial terrestrial LaserCom vendors have their sights set on the market segment described by the so-called "Last Mile" problem, aiming to serve telecom providers with a cheaper, rapidly deployable pipeline from buildings connected to fiber to nearby buildings that are not [54]. From a military perspective, LaserCom technology is of interest as a replacement and/or complement to existing and future RF based links [79]. USAF and DoD leadership have highlighted the importance of communication on the battlefield and outlined technology transformations being pursued to create a more

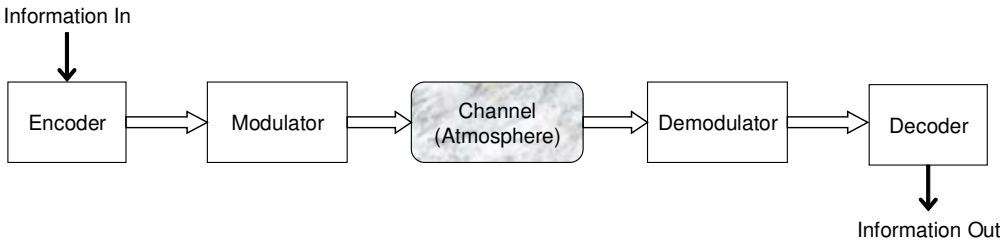

Figure 3.6: Major components of a digital communication system.

agile force able to meet new and emerging threats [81, 87]. LaserCom is identified as a specific technology being explored to provide more secure, higher bandwidth connections with the goal of providing decision makers with near real-time access to data collected anywhere [80,81]. LaserCom research for military applications is being conducted and sponsored by the Air Force Research Laboratory, the Air Force Institute of Technology, and other federal agencies such as the Defense Advanced Research Projects Agency [50].

3.8 LaserCom System Overview

The major components of a digital communication system are presented in Figure 3.6 [90]. The modulator converts bits to symbols prior to transmission through the channel. In the case of LaserCom, the channel is the stochastic atmosphere, whereas in fiber optics it is a well characterized glass fiber. For the On-Off Keyed (OOK) direct-detection system considered in this research, the relationship between bits and symbols is one-to-one. The symbols for a 1 and 0 are simply the on and off states of the laser source, respectively. The encoder and decoder implement Forward Error-Correction Coding (FEC) to decrease BER for a fixed transmitter power. Examples include linear block, convolutional, Reed-Solomon, and turbo codes [43,90]. FECs are not considered in this research for the following reasons. First, the focus of this work is on channel characteristics. Second, convolutional and turbo-codes are capable of providing significant performance improvement, but suffer from decoding delays - a drawback for real-time communication [43].

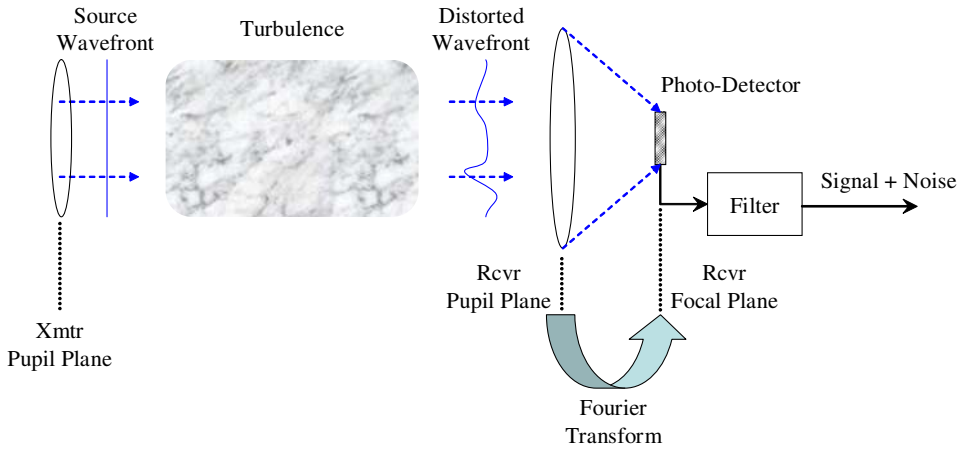

Figure 3.7: Optical receiver for direct-detection digital LaserCom.

The optical receiver model used for this research is described by Figure 3.7. The source wavefront originates from the transmitter's pupil plane. The primary aperture of the receiving telescope corresponds to the receiver's pupil plane, while the detector lies in the receiver's focal plane. Since the transmitter and receiver are separated by a significant distance for all scenarios of interest, the receiver's focal plane corresponds to the image plane. Thus, an image of the transmitting source is produced at the telescope focus. For coherent light, the (complex) optical field in the focal plane is related to the optical field in the pupil plane by a two-dimensional Fourier transform.

In a basic LaserCom system as described by Figure 3.7, a detector is placed in the receiver's focal plane. A filter follows the detector, where the filter's bandwidth is chosen to match the frequency content of the incoming signal. The filter output is the sum of signal and noise currents. Some applications require coupling into a single mode fiber (SMF) [73], which would replace the detector in the focal plane. Fiber coupling provides increased bandwidth, optical amplification, and flexibility in detector placement. The core diameter for SMFs is on the order of 9 μm [60].

3.9 Literature Review

A variety of approaches have been studied for the purpose of mitigating fluctuations in the received optical field subsequent to propagation through atmospheric turbulence. For this literature review, the large body of existing work is broadly divided into two major categories: wavefront control and signal processing. First, wavefront control techniques involve physically changing the optical field. Second, signal processing techniques are those which can be implemented solely in software or firmware. Important concepts from this body of work are now summarized.

3.9.1 Wavefront Control.

- Partial Spatial Coherence (transmitter)

  The degree of fluctuations in an optical field subsequent to propagation through turbulence depends on both strength of turbulence and the degree of spatial coherence at the transmitter. This has led to investigations of partial coherence for decreasing intensity fluctuations and improving (decreasing) bit-error rate [76, 77]. One simple approach to decrease spatial coherence is placing a phase diffuser in front of the transmitting beam [77]. However, by partially destroying spatial coherence at the transmitter, the beam size is increased and average power at the receiver is reduced. Also, Ricklin and Davidson [77] note that gains from partial coherence diminish with increasing turbulence strength, as the turbulence itself begins to dominate the degree of spatial coherence in the optical field.

- Adaptive Beam Size (transmitter)

  Adaptive adjustment of the transmitter beam size has been investigated and shown to mitigate intensity fluctuations at the receiver for a ground-to-satellite configuration. From a system design standpoint, Yenice and Evans [105, 106] suggest that controlling the beam size by a factor of two over relatively long time scales should be feasible. Nevertheless, this technique requires real-time

knowledge of atmospheric statistics and a more complicated architecture for the transmitter.

- Spatial Diversity (transmitter and/or receiver)

  The optical power captured by a real aperture will experience smaller fluctuations than a point receiver. A noticeable reduction occurs as the dimension of the receiving telescope increases beyond the spatial coherence of intensity. In this case, multiple patches of intensity are summed together and thus reduce the overall level of fluctuations. For tactical applications, this approach is limited due to size constraints on the receiving telescope. Furthermore, the SNR benefit from large apertures may be offset by increased background noise [8:226]. Variations on this theme include spatial diversity at the receiver via multiple smaller apertures [8], and at the transmitter via multiple source beams [48, 68, 88].

Implementing any of the above three wavefront control techniques requires hardware modification. Also, the first two techniques, partial coherence and adaptive beam size, pertain solely to the transmitter. This research only addresses receiver-based techniques and focuses on solutions that allow incorporation onto tactical platforms such as UAVs. Thus, the research approach is fundamentally different from those above.

- Adaptive Optics (transmitter and/or receiver)

  Tyson, et al. [98, 100] have experimentally demonstrated AO wavefront control as a means to improve BER performance of LaserCom systems. However, for strong scintillation scenarios, obtaining valid wavefront measurements is difficult. The S-H WFS degrades considerably in the presence of strong scintillation [17], which motivated the current development of the SRI WFS [73] by the Air Force Research Laboratory. The SRI WFS has been demonstrated to provide superior performance over the S-H in the presence of strong scintillation. An advanced MCAO system, as described in Section 3.6, could utilize the SRI WFS to yield a more robust AO system. This research presents a tracking-only

solution and demonstrates why it is optimal in the scenarios studied for the relevant error metric, BER.

AO technology has been thoroughly studied for HEL and space object imaging applications. However, the past five years have seen growing interest in using AO for improving LaserCom performance. Researchers have demonstrated BER reduction due to AO through both analysis [96] and experiment [98, 100]. However, a system design approach based on mean square phase [44], which is related to average Strehl ratio [47], continues to dominate the literature. This research is unique in that system optimization and design are driven by specific failure mechanisms instead of the standard design equations based on mean square phase.

3.9.2 Signal Processing.

- Forward Error-Correction Codes and Interleaving (transmitter and receiver)

  FECs have recently been considered for free-space LaserCom systems. Zhu and Kahn [110] developed an approximate upper bound on error-correction coding for LaserCom, assuming weak turbulence. Block, convolutional, and turbo coding performance was considered, as well as varying the interleaver length for block and turbo codes. Zhu and Kahn [108, 109] also studied maximum-likelihood and Markov model detection techniques. Ohtsuki [66] showed that turbo-codes outperform convolutional codes for certain LaserCom scenarios. Yu, Li, and Ricklin [107] studied Reed-Solomon codes and demonstrated improved performance for log-normal (i.e., weak turbulence) atmospheric statistics. FECs are not considered in this research for the following reasons. First, the focus of this work is on channel characteristics. Second, convolutional and turbo-codes are capable of providing significant performance improvement, but suffer from decoding delays - a drawback for real-time communication [43]. However, FECs are not incompatible with the work presented. In fact, they are complementary,

and results from Chapter IV guide the design of FECs and interleaving for the air-to-air scenarios studied.

- Adaptive Thresholding (receiver)

  An adaptive detection threshold has recently been explored as a method to decrease BER in the presence of scintillation. Burris, et al. [26, 27, 45] have focused on the problem of parameter estimation. Kalman filters [26,27,45], least mean square adaptive predictors [45], and maximum likelihood techniques [45] have been evaluated for estimating the mean and variance of bit levels over time. These techniques have been shown to be capable of improving BER by an order of magnitude or greater [25, 52]. This same group of researchers are currently implementing a system to experimentally evaluate adaptive thresholding in a maritime environment at a Naval Research Laboratory facility. The propagation path is a 10 mile ground-to-ground link across the Chesapeake Bay. Current system design and initial results were presented in August 2005 [52].

  The existing work of Burris, et al. has focused on the detection/estimation aspect of the adaptive thresholding problem, as well as experimental evaluation of performance in a maritime environment. The results of this research both complement and extend these published results. Chapter VI provides a new analytic expression for BER using an adaptive threshold, given an arbitrary PDF describing turbulence-induced intensity fluctuations. Furthermore, current published results are based on data from a 10 mile ground-to-ground maritime scenario. These results are not directly applicable to a moderate to long-distance air-to-air scenario due to the shorter propagation length and ground-layer turbulence considerations. The gamma-gamma PDF has received significant attention in recent work and currently provides the best analytic description of turbulence-induced intensity fluctuations. In fact, the gamma-gamma PDF has been recently utilized to produce analytic BER predictions describing the effect of AO [96] and aperture averaging [8] on LaserCom performance. The gamma-gamma PDF is proposed for use in extending the analytic BER expressions for

optimal fixed and adaptive thresholds derived in Chapter VI to a wide variety of turbulence and propagation scenarios. The new BER expressions, including the gamma-gamma PDF, provide the first analytic performance predictions for an adaptive threshold applied in a moderate to long-distance air-to-air scenario of interest.

IV. Alternate Tracking Techniques for Fade Mitigation

A majority of Adaptive Optics (AO) research and development has focused on maximizing average Strehl by minimizing residual mean square phase aberration. Furthermore, most (if not all) currently operational AO systems are ground based. However, AO has more recently been considered as a means to improve performance of LaserCom systems operating through the atmosphere. For communication performance, the probability of fade and the associated tail of the signal power's PDF are more important than average signal power. Small airborne platforms face size, weight, power, and other limitations which are not a primary concern for ground based systems. Optimization for fade probability versus average Strehl and the constraints imposed on small airborne platforms motivated a metric-driven, critical mode approach to wavefront control.

Section 4.1 addresses relevant Air Force applications and presents the results of a basic engagement analysis for a 100 km propagation path. Propagation effects and system performance were investigated further using a wave-optics simulation constructed in WaveTrain™ and executed from `Matlab`®. Details of the simulation setup and model validation are provided in Section 4.2. A first-order Strehl analysis is presented in Section 4.3.1. Spot breakup in the focal plane image is demonstrated in Section 4.3.2 and identified as the primary failure mechanism. Peak tracking was investigated as a means to limit the impact of spot breakup on fade probability and was found to outperform both centroid tracking and AO in the air-to-air scenario. Initial peak tracking simulation results are presented in Section 4.3.3. The impacts of a higher fidelity receiver model are explored in Section 4.3.4. Fidelity was increased by including mirror dynamics and a model of the Shack-Hartmann wavefront sensor. Performance impacts were minimal for peak tracking, but considerable for traditional AO. The possibility of a peak tracker jumping from one distinct bright region to another during a single period of spot breakup was also considered, and possible modifications to the basic algorithm are proposed for future research. The duration of signal fades and periods of focal plane image breakup are then characterized in

Table 4.1: Air and space platforms for potential LaserCom links [55, 62].

	(feet)	(km)
Airborne Platform	**Approximate Ceiling**	
Predator A	25,000	7.62
Predator B	50,000	15.24
Airborne Laser (ABL)	40,000	12.19
Global Hawk	65,000	19.81
Airship (low)	70,000	21.34
Airship (high)	100,000	30.48
Spaceborne Platform	**Approximate Altitude**	
LEO Satellite	3.28×10^6	1000
GEO Satellite	114.8×10^6	35000

Sections 4.3.5 and 4.3.6, respectively. From a system design standpoint these results are important for both sensor frame-rate and system bandwidth requirements, as well as optimizing error-correction codes. Final conclusions from this effort and directions for future research are presented in Sections 4.4 and 4.5, respectively.

4.1 Introduction and Air-to-Air Engagement Analysis

Potential LaserCom links of military interest would connect ground, air, and space-based assets [50]. A list of potential air and space platforms is presented in Table 4.1 [55, 62]. In particular, UAVs on reconnaissance/surveillance missions can produce large amounts of imaging data. In the air-to-space scenario, a LaserCom uplink to a communication satellite in Geosynchronous Orbit (GEO) is a potential solution for high bandwidth offload and data dissemination. Another possibility is an air-to-air scenario where one UAV is reconnoitering over enemy lines and a second UAV is deployed some distance away and used to relay real-time imagery to fixed or mobile positions on the ground. The second UAV would provide a flexible, quickly deployed high-speed link over obstacles such as mountainous terrain, as well as limiting the effects of atmospheric turbulence for a potential air-to-ground optical connection. Other possible links include ground-to-air, space-to-space, and space-to-ground. Due to the increasing role of UAVs on the battlefield [50] and their probable requirement for

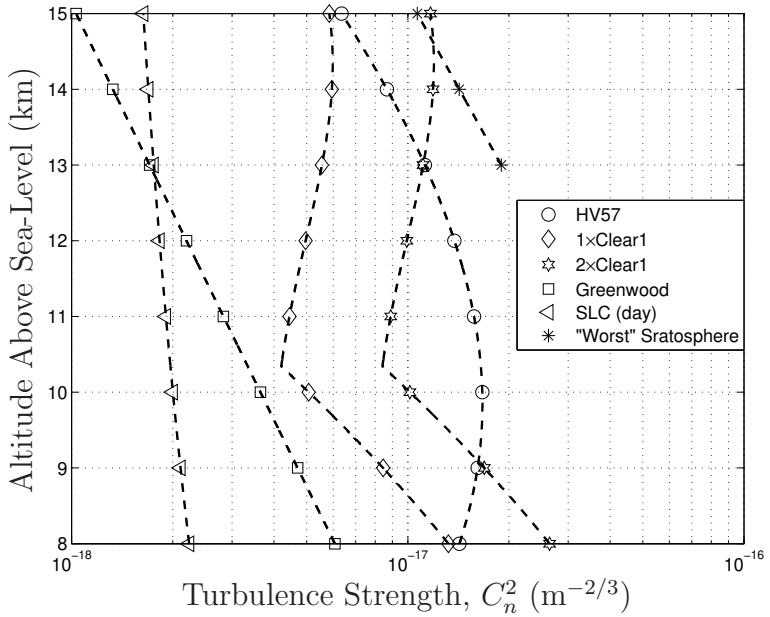

Figure 4.1: Models of turbulence strength as characterized by the refractive index structure parameter, C_n^2, for altitude ranging from 8 to 15 km.

simple and compact wavefront control systems, the air-to-air scenario was identified as the focus of this study.

The scenario used to study LaserCom fades and fade mitigation is modelled after a theoretical UAV-to-UAV optical communication link. The maximum ceiling of the Predator is approximately 8 or 15 km, depending on the model [62]. The nominal scenario for this research is a 100 km crosslink with each platform at an altitude of 10 km. The minimum altitude of the line-of-sight between the two UAVs is approximately 9.8 km. Therefore, the path is modelled as having constant turbulence strength. Several models of the refractive index structure parameter C_n^2 are plotted in Figure 4.1 for altitudes ranging from 8 to 15 km [20,51]. C_n^2 values are seen to vary from approximately 1×10^{-18} to 3×10^{-17} $m^{-2/3}$ over this altitude range. In reality, C_n^2 varies with altitude, location (geography), and time of day [84:61]. These models are based on curve fitting to the average of many measurements. Furthermore, this work is concerned with LaserCom performance under difficult conditions, so turbulence strength was allowed to range from 1×10^{-18} to 1×10^{-16} $m^{-2/3}$. Note that the worst-

Table 4.2: Optical turbulence parameters describing a 100 km air-to-air LaserCom scenario at a wavelength of 1.5 μm. Both the transmitting and receiving apertures have a diameter of 20 cm.

		Plane Wave			Spherical Wave		
C_n^2 ($m^{-2/3}$)	θ_0 (μrad)	r_0 (cm)	σ_χ^2	D/r_0	r_0 (cm)	σ_χ^2	D/r_0
1×10^{-18}	6.77	119.8	0.02	0.17	215.8	0.01	0.09
2×10^{-18}	4.47	79.0	0.05	0.25	142.4	0.02	0.14
3×10^{-18}	3.50	62.0	0.07	0.32	111.6	0.03	0.18
4×10^{-18}	2.95	52.1	0.10	0.38	93.9	0.04	0.21
5×10^{-18}	2.58	45.6	0.12	0.44	82.2	0.05	0.24
6×10^{-18}	2.31	40.9	0.14	0.49	73.6	0.06	0.27
7×10^{-18}	2.11	37.3	0.17	0.54	67.1	0.07	0.30
8×10^{-18}	1.95	34.4	0.19	0.58	62.0	0.08	0.32
9×10^{-18}	1.81	32.1	0.22	0.63	57.7	0.09	0.35
1×10^{-17}	1.70	30.1	0.24	0.67	54.2	0.10	0.37
2×10^{-17}	1.12	19.9	0.48	1.01	35.8	0.19	0.56
3×10^{-17}	0.88	15.6	0.72	1.29	28.0	0.29	0.71
4×10^{-17}	0.74	13.1	0.96	1.53	23.6	0.39	0.85
5×10^{-17}	0.65	11.5	1.20	1.75	20.6	0.48	0.97
6×10^{-17}	0.58	10.3	1.44	1.95	18.5	0.58	1.08
7×10^{-17}	0.53	9.4	1.68	2.14	16.9	0.68	1.19
8×10^{-17}	0.49	8.6	1.92	2.32	15.6	0.78	1.29
9×10^{-17}	0.46	8.1	2.16	2.49	14.5	0.87	1.38
1×10^{-16}	0.43	7.6	2.40	2.65	13.6	0.97	1.47

case of 1×10^{-16} $m^{-2/3}$ matches what was used by Roggemann and Koivunen [82] in a study of wavefront sensing and deformable mirror control in strong scintillation.

Table 4.2 presents values of the isoplanatic angle (θ_0), Fried parameter (r_0), and log-amplitude variance (σ_χ^2) for a wavelength of 1.5 μm and C_n^2 values ranging from 1×10^{-18} to 1×10^{-16} $m^{-2/3}$. Corresponding values of D/r_0 are also provided for a 20 cm diameter aperture. Because this scenario assumes constant turbulence strength, these parameter values apply to both propagation directions: outbound and inbound. Equations for θ_0, r_0, and σ_χ^2 are presented in Chapters II and III and are

repeated here for reference. The well known result for log-amplitude variance is [67]

$$\sigma_\chi^2(L) = 0.5632\, k^{7/6} \int_0^L \left[\gamma(L-z)\right]^{5/6} C_n^2(z)\, dz \quad , \tag{4.1}$$

where $\gamma = 1$ for a plane wave or $\gamma = z/L$ for a spherical wave, and integration is from source to observer. For constant turbulence strength, the integrals can be evaluated due to the resulting constancy of C_n^2. For spherical wave log-amplitude variance, the integral over the C_n^2 weighting factor is not trivial, but can be solved in terms of Gamma functions [67:197]. For plane and spherical waves, the simplified expressions for log-amplitude variance are given by [67]

$$\begin{aligned} \sigma_{\chi,\text{plane}}^2 &= \frac{-5\sqrt{3}}{33}\left(\frac{\pi}{2}\right)^{5/3} \frac{\Gamma(2/3)\Gamma(-5/12)}{\Gamma(11/12)} \lambda^{-7/6} L^{11/6} C_n^2 \\ &\approx 2.62\lambda^{-7/6} L^{11/6} C_n^2 \end{aligned} \tag{4.2}$$

and

$$\begin{aligned} \sigma_{\chi,\text{sph}}^2 &= \frac{-5\sqrt{3}}{96}\left(\frac{\pi}{2}\right)^{5/3} \frac{\Gamma(2/3)\Gamma(-5/12)\Gamma(5/6)\Gamma(11/6)}{\Gamma(11/12)\Gamma(5/3)} \lambda^{-7/6} L^{11/6} C_n^2 \\ &\approx 1.06\lambda^{-7/6} L^{11/6} C_n^2 \quad . \end{aligned} \tag{4.3}$$

The corresponding expressions for the Fried parameter are [84]

$$\begin{aligned} r_{0,\text{plane}} &= \left(\frac{5}{4}\right)^{1/10} \left[\frac{6\Gamma(6/5)}{\pi^3}\right]^{1/2} \left[\frac{\Gamma(2/3)}{\Gamma(1/6)}\right]^{3/5} \lambda^{6/5} \left(LC_n^2\right)^{-3/5} \\ &\approx 0.185\lambda^{6/5} \left(LC_n^2\right)^{-3/5} \end{aligned} \tag{4.4}$$

and

$$\begin{aligned} r_{0,\text{sph}} &= \left(\frac{5}{4}\right)^{1/10} \left[\frac{6\Gamma(6/5)}{\pi^3}\right]^{1/2} \left[\frac{\Gamma(2/3)}{\Gamma(1/6)}\right]^{3/5} \lambda^{6/5} \left(\frac{3}{8} LC_n^2\right)^{-3/5} \\ &\approx 0.185\lambda^{6/5} \left(\frac{3}{8} LC_n^2\right)^{-3/5} \quad . \end{aligned} \tag{4.5}$$

The simplified expression for the isoplanatic angle (which is independent of plane versus spherical wave propagation) is [89]

$$\begin{aligned} \theta_0 &= \pi^{-3/2} \left[\frac{3}{5} \frac{\Gamma(1/6)}{\Gamma(2/3)} \right]^{-3/5} \lambda^{6/5} \left(L^{8/3} C_n^2 \right)^{-3/5} \\ &\approx 0.104 \, \lambda^{6/5} \left(L^{8/3} C_n^2 \right)^{-3/5} \quad . \end{aligned} \tag{4.6}$$

Using the outcome of this basic analysis, specific engagements were identified as candidates for further study using wave-optics simulation. The main concern of this research is communication performance under difficult conditions, so attention was focused on engagements resulting in moderate to strong turbulence [20:186]. This is the point where conventional techniques become inadequate, both in terms of understanding system failure and ability to mitigate the fades.

4.2 Simulation Methodology

4.2.1 Simulation System Overview. The wave-optics simulation used for this study was constructed in WaveTrain™. Once the model was created and debugged, the simulation code was saved as a *.dll file. `Matlab`® was then used to both run the simulation (via the mex-file interface) and analyze results. The top-level block diagram as viewed in WaveTrain™ is presented in Figure 4.2. Basically, the simulation consists of a laser source, the atmosphere, data sensors, and several compensation schemes. The source is a 1 watt collimated Gaussian beam. A near infrared wavelength of 1.5 μm was chosen for this study based on existing source and sensor technologies developed for commercial telecommunications. The atmosphere is modelled by 10 phase screens which are equally spaced over the 100 km path. The first screen is located 10 km from the source and the last screen lies in the pupil plane of the receiver. The inner and outer scales of turbulence were assumed to be 1 mm and 100 m, respectively. An identical set of random seeds was used to generate screens for each C_n^2 value to allow comparisons of instantaneous Strehl across turbulence strength and provide experimental repeatability. According to available documentation, WaveTrain™ uses

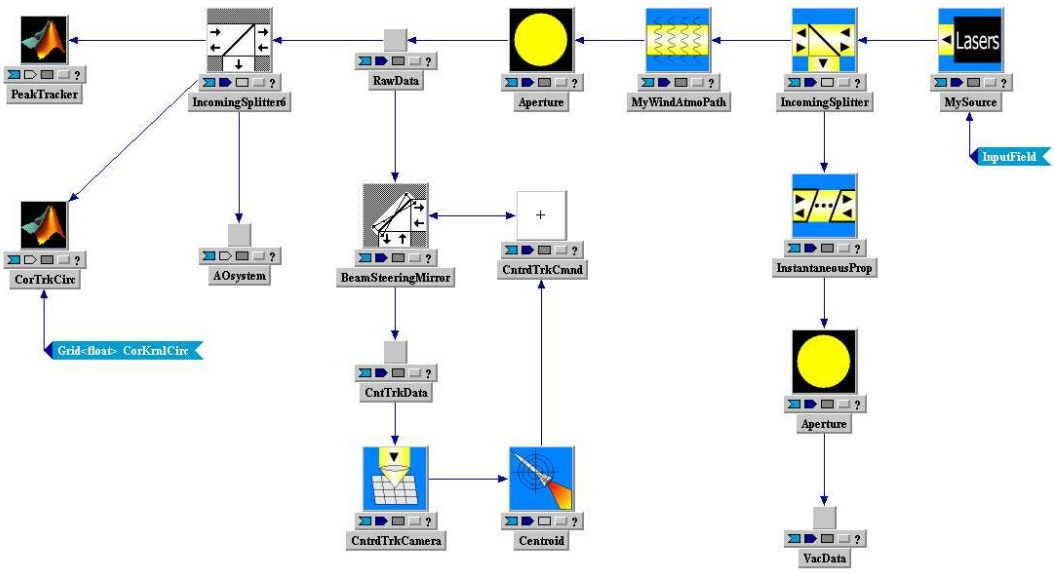

Figure 4.2: The WaveTrain™ model used to generate a wave-optics simulation for studies of deep fade phenomenology and fade mitigation.

the standard FFT phase screen generation method. However, an optional switch *locFlag* [71] initiates augmentation of tip/tilt power, which is underrepresented in the basic FFT approach [72]. Subsequent to initial model validation efforts, all phase screens for this research were generated using $locFlag = 1$ which corresponds to a first-order (tip/tilt) Zernike boost. The variances of Zernike modes two and three (see Table 2.1) are increased to match Noll's theoretical result [64], which assumes Kolmogorov turbulence.

A sample spacing of 1 cm was used for all propagation grids. For this grid spacing, the chosen wavelength, and screen-to-screen propagation distance, the minimum grid size to avoid aliasing of the fresnel angular spectrum propagator [42] is $n_{min} = 300$ pixels. The next highest power of two is 512 which is the propagation grid size used for all results presented here. Also note that r_0 values at $C_n^2 = 1 \times 10^{-16}$ m$^{-2/3}$ are 7.6 cm and 13.6 cm for plane and spherical waves, respectively. These values imply that for the strongest turbulence strength studied, there are somewhere between 7 and 14 samples per r_0. Parameter values for the initial WaveTrain™ simulation are

Table 4.3: Initial WaveTrain™ parameter values for the wave-optics simulation.

SOURCE	
Type	Collimated Gaussian beam
Beam Waist ($1/e$ point of amplitude)	7.5 cm
Power	1 watt
Wavelength	1.5 μm
Aperture Diameter	20 cm (no central obscuration)
ATMOSPHERE	
Engagement Scenario	Air-to-Air
C_n^2 Profile	Uniform
Path Length	100 km
Phase Screen Profile	10 uniformly spaced screens
Phase Screen Generation Method	FFT with low-order correction
Wind Speed (uniform crosswind)	10 m/s
TRACKING	
Receiver Aperture Diameter	20 cm (no central obscuration)
Beam Steering Mirror (BSM) Dynamics	2-axis critically damped harmonic oscillator
BSM Time Constant	1×10^{-4} sec
Track Camera Size	256×256 pixels
Pixel Size	0.586 μm ($\sim$ 31 pixels across Airy disk)
Camera Frame Rate	1 kHz
Integration Time	1 μsec
System Latency	0 sec
ADAPTIVE OPTICS (AO)	
Receiver Aperture Diameter	20 cm (no central obscuration)
Deformable Mirror (DM) Dynamics	Critically damped harmonic oscillator
Actuator Time Constant	1×10^{-4} sec
Number of DM Actuators	21
Number of HWFS Subapertures	16
Wavefront Sensor Camera Size	257×257 (64 samples per subaperture)
Pixel Size	2.34 μm ($\sim$ 31 pixels across Airy disk)
Camera Frame Rate	1 kHz
Integration Time	1 μsec
System Latency	0 sec

given in Table 4.3 and basically describe an idealized model with no latency, no noise, and oversampling of the focal plane.

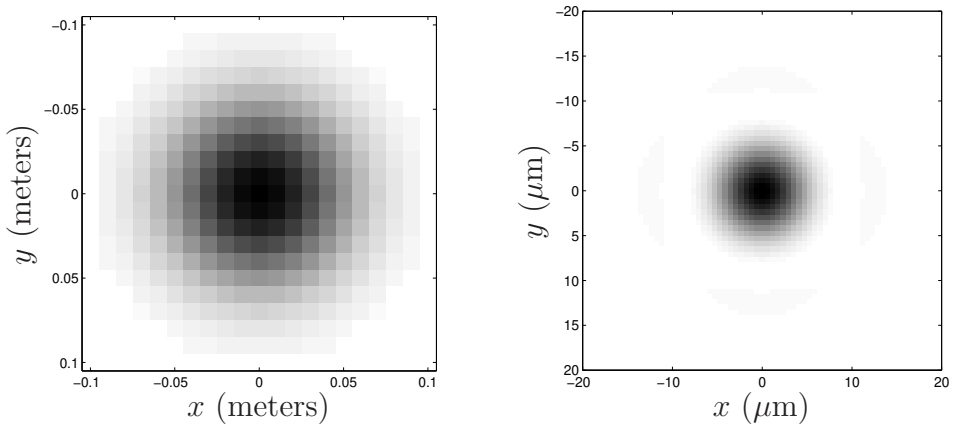

(a) Transmitter Pupil Plane Intensity (b) Receiver Focal Plane Intensity

Figure 4.3: Vacuum propagation results used for model validation and performance-metric normalization.

4.2.2 Vacuum Propagation Results. The following data were collected in the case of no atmosphere to verify normalization, particularly for calculation of log-amplitude variance (σ_χ^2) and performance metrics:

1. Source field at transmitter pupil plane,
2. Pupil plane field at receiver, and
3. Focal plane intensity at receiver.

Images of vacuum propagation results are displayed in Figure 4.3. The source transmits 1.0 w (0 dB) of optical power through a 20 cm aperture. In a perfect vacuum with performance limited only by diffraction effects, 34.9 mw (-14.57 dB) of optical power is captured at the receiver by a 20 cm aperture. In the focal plane, the power in the on-axis pixel is 41.8 μw (-43.79 dB). For a focal length of $f = 1$ m, the power within a circular area matching the size of the Airy disk (diameter $= 2.44\lambda f/D = 18.3$ μm) is 29.3 mw (-15.34 dB). This is 83.8% of the power captured by the pupil and matches well with the 84% predicted by diffraction theory [46:461].

4.2.3 Atmospheric Model Design. Several points should be considered when setting up a layered atmospheric model in a wave-optics simulation. One primary con-

Table 4.4: Simulated and theoretical log-amplitude variance for a 100 km uniform turbulence path at a wavelength of 1.5 μm. 100 independent atmospheric realizations were used to estimate σ_χ^2 for each value of C_n^2.

	$\hat{\sigma}_\chi^2$ from Simulation		σ_χ^2 from Theory	
C_n^2 ($\mathrm{m}^{-2/3}$)	$locFlag = 0$	$locFlag = 1$	Plane Wave	Spherical Wave
2×10^{-17}	0.16	0.19	0.48	0.19
3×10^{-17}	0.24	0.30	0.72	0.29
4×10^{-17}	0.31	0.40	0.96	0.39

cern is that sampling requirements are satisfied, which is discussed in Section 4.2.1. The focus here is on four other considerations impacting the choice of number, generation method, and placement of phase screens:

- The impact of phase screen low-order correction on simulated irradiance fluctuations at the receiver.
- The minimum screen separation must be greater than L_0 to allow use of independent phase screens for each layer.
- The modelling accuracy for most optical turbulence parameters depends on the number of screens.
- Wave-optics simulations inherently assume that each segment represents a phase only perturbation, so the amplitude fluctuations introduced by any single layer should be small.

As stated in Section 4.2.1, WaveTrain™ uses the basic FFT method for generating statistically independent phase screens. This method suffers from a well-documented underrepresentation of low-frequency variations [72]. To determine whether or not the optional low-order Zernike boost has a noticeable impact on simulated irradiance fluctuations, log-amplitude variance was estimated for several turbulence strengths and for both $locFlag = 0$ and $locFlag = 1$ conditions. The on-axis pixel was used to estimate σ_χ^2 from 100 independent realizations of the atmosphere. Results are presented in Table 4.4. Note that by including low-order phase correction,

the simulated log-amplitude variance increased on the order of 20 to 30%. Often, the underrepresentation of low frequencies is ignored by assuming their removal by a closed-loop system. Published results exploring the impact of the cumulative effects of missing low-frequency content (in multiple layers) on statistics of the received field were not found during the literature review. Due to the focus of this research on the impact of intensity fluctuations on fade probability, $locFlag = 1$ was used for all subsequent simulations.

Assuming that the simulation will generate statistically independent phase screens, an upper limit on the number of screens is imposed by the outer scale of turbulence, L_0. In order to allow screen independence, the following is required:

$$\Delta L = \frac{L}{N} \geq L_0 \tag{4.7}$$

where L is the total propagation distance, N is the number of screens, L_0 is the outer scale, and uniform screen spacing is assumed. An upper limit for the number of phase screens can be expressed as

$$N_{max} = \frac{L}{L_0} \quad . \tag{4.8}$$

For the scenario studied here with $L = 100$ km and $L_0 = 100$ m, the maximum number of screens is 1000. In practice, available computing resources must also be considered in choosing a value for N. Typically, 4 to 20 screens are used [71, 84] with the low end of this range coinciding with astronomical applications where a significant portion of the total turbulence is located near the aperture [84:66-7]. For paths yielding moderate to strong scintillation, such as the extended turbulence path studied in this research, 10 to 20 screens is typical [15]. As stated previously, this research used 10 screens over a 100 km path, matching that used by Roggemann and Koivunen [82].

The third consideration for setting up a wave-optics simulation is to ensure that enough screens are used to properly model the parameters of interest. For the metric of interest (fade probability), intensity fluctuations are of ultimate concern, but pupil

plane phase is directly related to focal plane intensity and thus important for wavefront compensation techniques. Many parameters describing optical turbulence effects are proportional to moments of the C_n^2 profile. In most cases, error is introduced by including a necessarily finite number of layers. Often, this effect is studied, if at all, by increasing the number of screens and seeing if results change. However, better analytic quantification is sought here by examining the difference between continuous and layered C_n^2 profiles, and the resulting impact on parameters of interest. Results are now presented for both σ_χ^2 and r_0.

The discretization error in modelling the log-amplitude variance and Fried parameter is now quantified. The equation for log-amplitude variance as a function of a continuous C_n^2 profile is given in (2.105) for the spherical wave case. These equations were derived from Rytov theory by assuming the Kolmogorov spectrum and a specific form of the source wavefront. By further assuming that the turbulence lies in layers separated by $\Delta L = L/N$, (2.105) can be rewritten as [82, 84]

$$\sigma^2_{\chi,layered}(L) = \frac{-5\sqrt{3\pi}}{144}\frac{\Gamma(2/3)\Gamma(-5/12)}{\Gamma(11/12)}2^{1/6}k^{7/6}\frac{L^{11/6}}{N^{8/3}}\sum_{m=1}^{N}\left[m(N-m)\right]^{5/6}\mathrm{C}^2_{\mathrm{n}_m} \quad . \tag{4.9}$$

The expression in (4.9) assumes uniform screen spacing with the first screen located ΔL from the source and the last screen located in the receiver's pupil plane. By also assuming constant turbulence strength, (4.9) becomes

$$\sigma^2_{\chi,layered}(L) = \frac{-5\sqrt{3\pi}}{144}\frac{\Gamma(2/3)\Gamma(-5/12)}{\Gamma(11/12)}2^{1/6}k^{7/6}\frac{L^{11/6}}{N^{8/3}}\,\mathrm{C}^2_{\mathrm{n}}\sum_{m=1}^{N}\left[m(N-m)\right]^{5/6} \quad . \tag{4.10}$$

For the case of non-uniform turbulence, C_n^2 could be modelled as piecewise-constant. The discretization error for log-amplitude variance is now expressed as

$$\varepsilon_{\sigma^2_\chi} = \frac{|\sigma^2_\chi - \sigma^2_{\chi,layered}|}{\sigma^2_\chi} \quad . \tag{4.11}$$

Substituting (4.3) and (4.10) into (4.11) gives the following error expression for spherical wave log-amplitude variance as a function of the number of screens:

$$\varepsilon_{\sigma_\chi^2,sph}(N) = 1 - \frac{16}{3}\frac{\Gamma(5/3)}{\Gamma(5/6)\Gamma(11/6)}N^{-8/3}\sum_{m=1}^{N}\left[m(N-m)\right]^{5/6} \quad . \tag{4.12}$$

The corresponding expression for a plane wave source is given by

$$\varepsilon_{\sigma_\chi^2,pln}(N) = 1 - \frac{11}{6}N^{-11/6}\sum_{m=1}^{N}(N-m)^{5/6} \quad . \tag{4.13}$$

An identical approach can be taken to describe the error in modelling phase fluctuations. The resulting discretization error for the spherical wave Fried parameter is given by

$$\varepsilon_{r_0,sph}(N) = 1 - \left(\frac{8}{3}N^{-8/3}\sum_{m=1}^{N}m^{5/3}\right)^{-3/5} \quad . \tag{4.14}$$

Note that in the plane wave case, there is no discretization error for the Fried parameter because there is no weighting factor on the C_n^2 profile.

Analytic results of (4.12), (4.13), and (4.14) are plotted in Figure 4.4 for $N = 1, 2 \ldots 50$. Although Roggemann and Koivunen [82] did compare the numerical values of the layered and continuous formulations of log-amplitude variance for their chosen value of N [82:913], the results in Figure 4.4 provide a general result to guide the selection of N. Roggemann and Koivunen published (spherical wave) values of $\sigma^2_{\chi,layered} = 0.155$ and $\sigma_\chi^2 = 0.158$ corresponding to ten layer and continuous C_n^2 profiles, respectively. These values correspond to a discretization error of 1.9% per Equation (4.11), which matches well with the result of Figure 4.4 for $N = 10$. Equations (4.12), (4.13), and (4.14) provide a compact tool to assist an analyst in choosing the appropriate number of phase screens in a constant turbulence strength scenario, and with simple extensions non-constant C_n^2 as well.

Last, the extent to which the model has maintained a phase-only effect from each individual layer is considered. For the worst case scenario of $C_n^2 = 1 \times 10^{-16}$ m$^{-2/3}$,

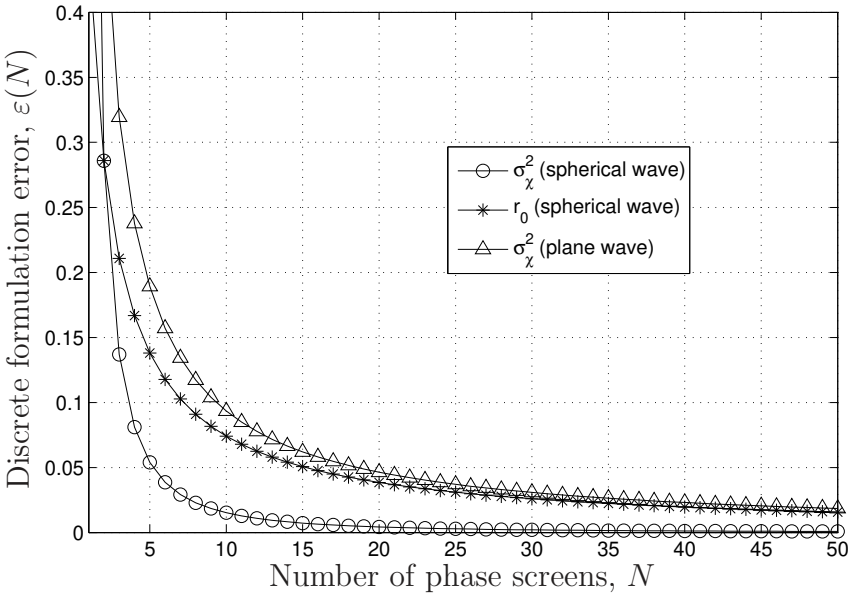

Figure 4.4: Log-amplitude variance and Fried parameter formulation error due to a layered C_n^2 profile. The scenario is a constant turbulence strength path with N uniformly spaced phase screens. The first screen is ΔL away from the source and the last screen is located $N \times \Delta L$ from the source, lying in the receiver's pupil plane.

the single (10 km) layer log-amplitude variance is 0.0352 and 0.0142 for plane and spherical wave sources, respectively. This corresponds to a spherical wave Rytov variance of 0.057, which corresponds to the weak irradiance fluctuation regime as desired [5:98-99].

4.3 Results

Fade probability is the performance Metric of Interest (MOI). This can be calculated for various quantities describing the received signal, such as Strehl, power-in-the-bucket, and optical fiber coupling efficiency. Strehl ratio was chosen for the results presented here based on its historical precedence. Strehl is typically defined as the ratio of the aberrated on-axis focal plane intensity to that for the case of unaberrated phase. This quantity is termed the *relative* Strehl ratio (S_R) because it describes performance relative to the power captured by the telescope at a given point in time and does not account for power lost due to scintillation. The fade rate calculations

presented here are in terms of *absolute* Strehl (S_A), which is defined as the ratio of the aberrated on-axis focal plane intensity to that resulting from vacuum propagation. Absolute Strehl is more useful for describing performance of a communication system, but relative Strehl may provide additional insight into the reasons for performance degradation.

4.3.1 First-Order Performance Analysis. Estimates of log-amplitude variance from simulation data (see Table 4.4) indicate that the Gaussian beam source is behaving much like a point source. Therefore, spherical wave Rytov theory results for the Fried parameter are also assumed to be indicative of the simulation. Corresponding values of D/r_0 were presented in Table 4.2. Note that $D/r_0 < 1$ until C_n^2 exceeds 5×10^{-17} m$^{-2/3}$. Even for the strongest turbulence considered (1×10^{-16} m$^{-2/3}$), $D/r_0 < 1.5$. These results indicate that atmosphere-induced phase perturbations in the receiver pupil plane are largely dominated by tip and tilt, even in the strongest turbulence conditions. From a system design perspective, this leads to consideration of a tracking-only solution as a primary option. Simple beamsteering is especially attractive for mobile tactical platforms where simplicity, compactness, and low power consumption are critical.

Performance is further explored using analytic results for Strehl. The "extended Marechal approximation" to the average relative Strehl ratio is given by [44, 89]

$$E\{S_R\} \simeq e^{-\epsilon^2} \tag{4.15}$$

where ϵ^2 is the aperture averaged mean square phase error in radians^2. Equation (4.15) is valid when ϵ is less than about two radians, assumes that amplitude fluctuations are negligible, and is often used for top-level analysis and design of wavefront control systems (see Section 3.5). This approximation yields a simple formula that can be combined with the results of Noll [64] to theoretically estimate performance as a

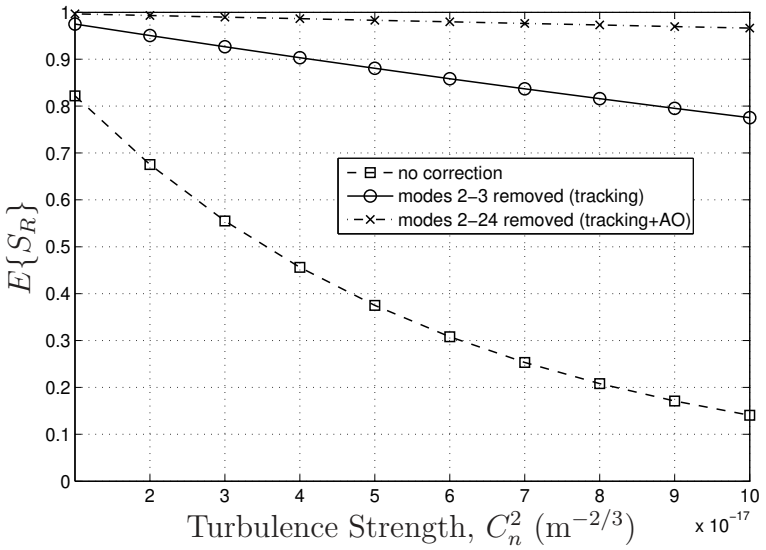

Figure 4.5: Analytic results for mean relative Strehl ratio using the extended Marechal approximation and the results of Noll.

function of D/r_0 and an assumed number of perfectly removed Zernike modes:

$$E\{S_R\} \simeq e^{-\alpha(D/r_0)^{5/3}} \tag{4.16}$$

where the value of α depends on which modes are removed. Three cases were evaluated: uncompensated ($\alpha = 1.0299$), tracking-only with removal of modes 2 and 3 ($\alpha = 0.134$), and tracking plus AO with removal of modes 2 through 24 ($\alpha = 0.0180$) [84]. The second case models an ideal tracking system, while the third case approximates an ideal AO system with tracking and a 21 actuator higher-order correcting element. Resulting average Strehl values are plotted in Figure 4.5. For the strongest turbulence case of $C_n^2 = 1 \times 10^{-16}$ $\mathrm{m}^{-2/3}$, (4.16) predicts worst case Strehls of 0.14 for an uncompensated system, 0.77 for tracking-only, and 0.97 for tracking plus AO. These results imply that tracking-only is a good solution, increasing S_R by a factor of 5.5. While tracking plus AO improves S_R more, it comes with significant added cost and complexity. Also, this is a first-order analysis and thus ignores scintillation effects which will decrease S_R averages stated above.

4.3.2 Initial Simulation Results. Based on the discussion presented in Section 4.3.1, a tracking-only system is an attractive alternative. At the same time, the given path distance and turbulence strengths correspond to the region of moderate to strong scintillation and the results of Marechal and Noll are not definitive. Therefore, a series of wave-optics simulations was undertaken to better understand performance under these challenging conditions.

After several exploratory simulation runs, a database of temporally correlated pupil fields was generated, encompassing 10 values of C_n^2: $[1, 2 \ldots 10] \times 10^{-17}$ m$^{-2/3}$. A uniform crosswind of 10 m/s (22.4 mph) in the x-direction and 0 m/s in the y-direction was applied. The Gaussian beam source was propagated through the 100 km (10 screen) path and receiver pupil fields were captured at 10 kHz. For a 1024×1024 pixel "atmosphere," 512×512 propagation grid, and 10 m/s wind, the maximum shift of the 10 screen atmosphere is 512 pixels without phase screen wrapping. Shifts greater than 512 pixels would result in repeated atmospheric statistics and degrade simulation accuracy. Pupil plane sample spacing is 1 cm per pixel, resulting in the following calculation for number of samples per atmospheric realization:

$$\frac{512 \text{ pixels} \times 1 \text{ cm/pixel}}{10 \text{ m/s}} \times 10 \text{ kHz} = 5120 \text{ samples per atmosphere} \quad . \tag{4.17}$$

Thirty such 5120 sample (i.e., 0.512 sec) runs were accomplished for each value of C_n^2, giving a total of $30 \times 5120 = 153,600$ (complex) pupil fields per turbulence strength. In other words, thirty independent realizations of the atmosphere were generated for each turbulence strength prior to propagation and screen shifting based on Taylor's frozen flow hypothesis (see Section 2.2.4). This approach provides multiple independent sets each containing temporally correlated pupil fields, which allows for investigation of temporal effects of turbulence and the ability to estimate various statistical quantities. Because this investigation is only considering wavefront control at the receiver, this pupil field database can be subsequently used as input to the receiver portion of the WaveTrain™ model without having to re-propagate through the phase screens. This

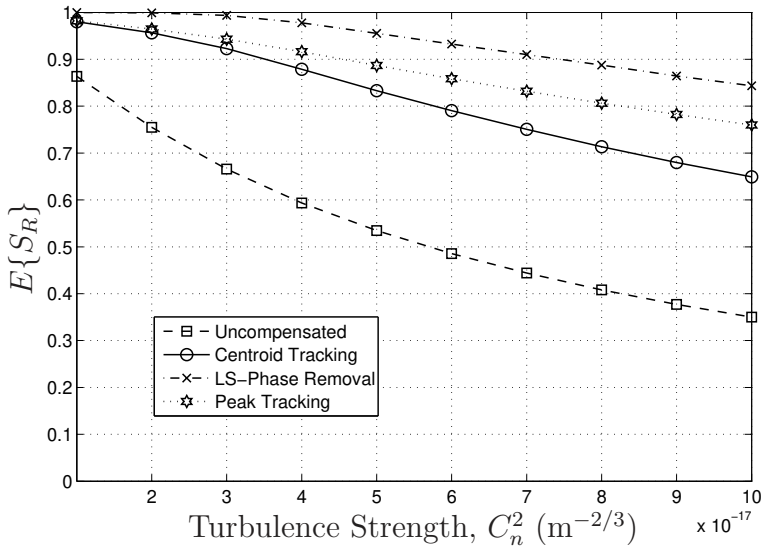

Figure 4.6: Simulation results for *mean relative Strehl ratio* calculated from wave-optics simulation. Approximately 153,600 data points from 30 0.512 sec simulation runs were used to estimate each $E\{S_R\}$ value. The scenario is a 100 km constant turbulence path with a 10 m/s uniform crosswind at a wavelength of 1.5 μm.

alleviates some of the computational burden each time a new wavefront control scheme is investigated. A receiver model written solely in `Matlab`® is also an option at this point, and was the approach taken next.

As the first step beyond analytic results of Section 4.3.1, the simulated pupil fields were propagated to the focal plane and metrics were calculated. This approach yields quicker results than WaveTrain™ at the expense of fidelity. First, mirror dynamics and signal processing latency are ignored. Second, the modelling of AO performance is based on perfect LS phase correction. This approach essentially provides an upper bound for the typical Shack-Hartmann/least-squares reconstructor system. In anticipation of upcoming results, this section also presents results for a peak intensity tracker.

Estimates of mean relative Strehl ratio are plotted in Figure 4.6. Simulation results are more optimistic than the Marechal/Noll approximation in the uncompensated case, but more pessimistic for centroid tracking and AO, which now yield improvement factors of less than 2 and 2.5, respectively. Simulation results for com-

plete LS-phase removal and centroid tracking both display a more rapid falloff in relative Strehl once turbulence strength exceeds $C_n^2 = 3 \times 10^{-17}$ m$^{-2/3}$, which is the region where the scenario enters the moderate amplitude fluctuation regime [5]. However, results for peak tracking in Figure 4.6 are very close to analytic predictions for ideal tracking in Figure 4.5. This result is at least partially explained by observations described in the next paragraph. Also note that relative Strehl for LS-phase removal and peak tracking both drop off at the nearly the same rate as turbulence strength increases, while centroid tracking drops off more rapidly.

In terms of communication system performance, deep signal fades are the greatest concern. BER for OOK direct-detection communication systems depends on the area under the PDF tail for signal-plus-noise conditions. For a closed-loop system operating in moderate to strong turbulence, the distribution average and variance may not have significant impact on BER. Therefore, the entire temporal set (30×0.512 sec $= 15.36$ sec per C_n^2 value) of absolute Strehl data for the centroid tracking case was examined and some of the deepest fades identified. Starting with the weakest turbulence explored in the simulation, $C_n^2 = 1 \times 10^{-17}$ m$^{-2/3}$, one deep fade was observed which clearly stood out from the rest of the data. The corresponding focal plane images were generated and a well-formed Airy-sized spot was observed throughout the fade period. Values of total power captured by the 20 cm telescope during the same period were then examined and a corresponding drop in power entering the aperture was observed. This type of fade cannot be addressed by the receiver alone. Next, the two deepest fades for $C_n^2 = 2 \times 10^{-17}$ m$^{-2/3}$ were investigated, which both standout visually as being much deeper than any others at this C_n^2 value, and are both significantly deeper than the minimum of the entire data set for $C_n^2 = 1 \times 10^{-17}$ m$^{-2/3}$. The focal plane images corresponding to the minimum of each fade are presented in Figures 4.7(a) and (b).

In both cases, the focal plane image has completely separated into two distinct regions, each comparable in size and shape to an Airy pattern. The occurrence of this degree of spot breakup is somewhat counterintuitive because D/r_0 is less than

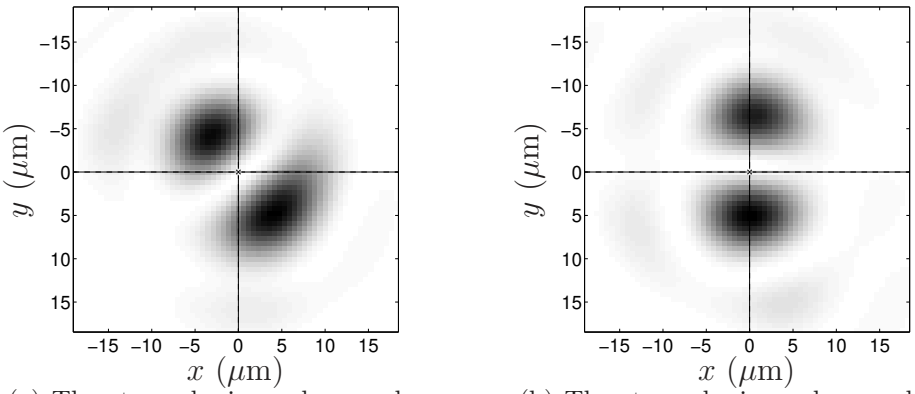

(a) The atmospheric random seed is 3 and the image is frame 2719 of 5120. The value of absolute Strehl is $S_A = 0.0014$ (-28.7) dB.

(b) The atmospheric random seed is 0 and the image is frame 3726 of 5120. The value of absolute Strehl is $S_A = 0.0023$ (-26.4) dB.

Figure 4.7: Two examples of focal plane image spot breakup for centroid tracking and a uniform turbulence profile of $C_n^2 = 2 \times 10^{-17}$ m$^{-2/3}$. The image in (a) corresponds to the minimum in S_A during the deepest fade at this turbulence strength, while (b) corresponds to the minimum of the second deepest fade. The scenario is a 100 km path with a 10 m/s uniform crosswind at a wavelength of 1.5 μm.

one (≈ 0.6). However, the spherical wave Rytov variance is 0.8, indicating that the scenario is approaching moderate scintillation conditions. In Chapter V, a greater understanding of the root cause of image breakup is pursued. For now, simply note that spot breakup occurs (if only rarely) for values of D/r_0 less than 1 and is identified as a failure mechanism for LaserCom, where extremely low bit-error rates are typically desired [67].

4.3.3 Benefit of Peak Tracking. The occurrence of spot breakup is not a great concern if there exists a fast enough detector that is also large enough to capture the entire image plane. For moderate bandwidths, such detectors exist and could be placed at the telescope focus. However, for current bandwidth requirements, this is not the case. Thus, an alternate approach is considered whereby captured energy is coupled into a SMF. The SMF is then coupled to a detector. For this set-up, spot breakup becomes a significant concern from the standpoint of fade probability. Coupling into an optical fiber may also be desirable for amplification purposes, such

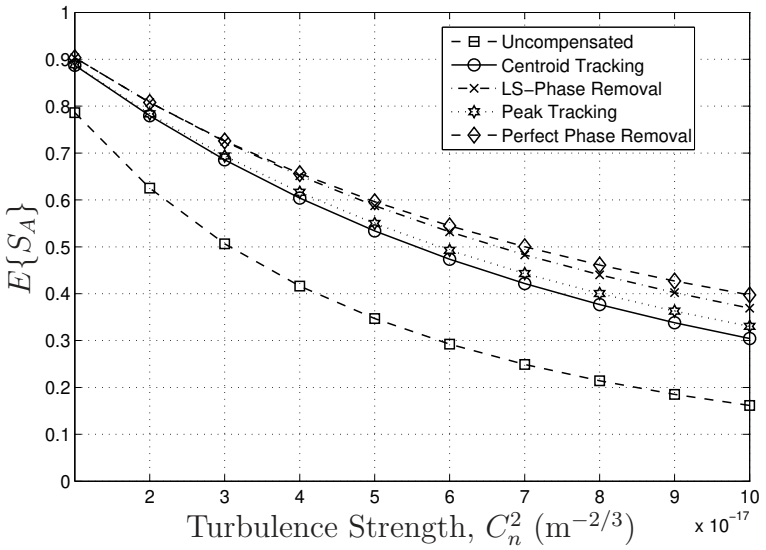

Figure 4.8: Simulation results for *mean absolute Strehl ratio* calculated from wave-optics simulation. Approximately 153,600 data points from 30 0.512 sec simulation runs were used to estimate each value of mean Strehl. The scenario is a 100 km path with a 10 m/s uniform crosswind at a wavelength of 1.5 μm.

as in the self-referencing interferometer wavefront sensor currently being developed by the Air Force Research Laboratory [73]. Flexibility in detector placement is another potential advantage. For this research, fiber-coupled detection is assumed. The core diameter for SMFs is on the order of 9 μm [60]. The diameter of the Airy disk for the chosen system parameters (see Table 4.3) and a focal length of $f = 1$ m is $2.44\lambda f/D = 18.3$ μm. Therefore, a traditional centroid tracking approach may force a low point between two peaks onto the fiber head and may remain there for the duration of spot breakup. A peak tracker could provide an increase in fade rate performance by forcing an intensity peak onto the fiber during image breakup.

From this point forward, performance results are presented in terms of *absolute Strehl*, which is more descriptive of the true communication system. Values of mean absolute Strehl are plotted in Figure 4.8. In addition to the four schemes presented in Figure 4.6, results are also included for perfect phase removal. Perfect phase removal is defined as replacing the distorted phase of the raw pupil field with uniform phase before propagating to the focal plane. In this case, the fluctuations in absolute Strehl

are due entirely to scintillation, both in terms of energy scattered out of the pupil and imperfections in the Airy pattern caused by pupil plane amplitude variations. While perfect phase correction is never achievable, it provides an informative upper bound on performance. Overall, wavefront control at receiver appears less effective in terms of absolute Strehl because energy scattered out of the pupil is accounted for by this metric. However, all wavefront control techniques are still providing some level of improvement. For turbulence strength less than $C_n^2 = 3 \times 10^{-17}$ m$^{-2/3}$, LS-phase removal results are indistinguishable from those for ideal phase removal, while for $C_n^2 < 2 \times 10^{-17}$ m$^{-2/3}$, centroid tracking results are indistinguishable from those for peak tracking. As turbulence strength increases, however, perfect phase removal begins to outperform LS-phase removal, and peak tracking begins to outperform centroid tracking. The increasing separation between LS and perfect phase removal is due to the hidden (i.e., branch point) portion of the phase which becomes non-zero as amplitude fluctuations increase. The increasing separation between centroid and peak tracking is due to periods of image breakup when the centroid is located in an intensity null between two bright spots. Also note that in terms of mean absolute Strehl, LS-phase removal outperforms peak tracking regardless of turbulence strength.

Attention is now turned to the metric of interest: fade probability. Fade probability results are presented in Figure 4.9 for a threshold defined as 2% (-17 dB) of the on-axis focal plane power in vacuum. This threshold value is representative of a detection threshold corresponding to realistic values of BER. Additionally, computation requirements for estimating fade probability increase as the threshold decreases. Results in Figure 4.9 show that peak tracking is providing a significant increase in performance over all techniques except perfect phase removal. For the strongest turbulence case and the given threshold, peak tracking is fading 79% less often than an uncompensated system, and 54% and 29% less often than centroid tracking and LS-phase removal, respectively. This result is in contrast to both the analytic first-order analysis and simulation results for mean relative and absolute Strehl, where tracking-only systems always performed poorer than AO (LS-phase removal). The

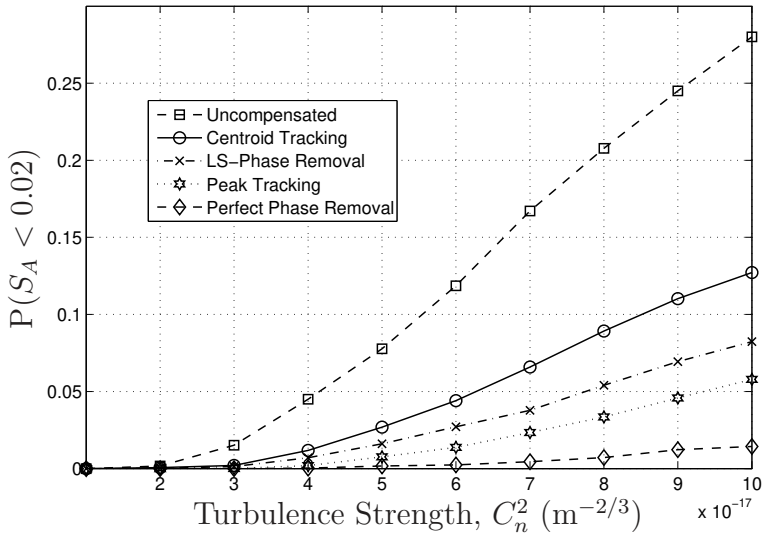

Figure 4.9: Fade probability results calculated using the lower fidelity `Matlab`® receiver model. Approximately 153,600 data points from 30 0.512 sec simulation runs were used to calculate each value of fade probability using a threshold of $S_A = 0.02$. The scenario is a 100 km path with a 10 m/s uniform crosswind at a wavelength of 1.5 μm.

fact that peak tracking (control of only two Zernike phase modes) is outperforming perfect removal of the entire LS-phase is remarkable, and emphasizes the importance of comparing performance using the appropriate metric. These results are also encouraging for potentially smaller, mobile platforms where higher-order wavefront sensing and control would add significant cost and complexity. Additionally, performance of the most widely used higher-order wavefront sensing approach, the Shack-Hartmann, drops off in high scintillation scenarios [17], which implies an inability to achieve perfect LS-phase correction.

The gain in fade rate performance from peak tracking is due to the fact that it prevents the system from dwelling in a valley between two peaks during periods of image breakup. Of course, in an actual system, the peak tracker may at times transition from the peak of one subspot to the peak of another during a single period of image breakup. The finite response time of the mirror and the high rate at which communication systems operate may result in dropouts during these transition

periods, a problem that was ignored up to now by assuming instantaneous mirror response. This potential problem is investigated further in Section 4.3.4.

4.3.4 Impact of Finite Mirror Bandwidth. To better understand the impact of hardware dynamics on fade probability, receiver propagations were recalculated using the WaveTrain™ model. As discussed in Section 4.3.2, the main differences between the `Matlab®` and WaveTrain™ receiver simulations are hardware dynamics and AO model fidelity. WaveTrain™ models both BSM and DM actuator dynamics as critically damped harmonic oscillators with a response time of 1×10^{-4} sec. Track camera and wavefront sensor frame rates are also reduced to 1 kHz in the WaveTrain™ model, giving nine data points between track camera and wavefront sensor images to observe the impact of finite mirror bandwidth. Another difference between the two models is that the `Matlab®` code uses a 128×128 grid to propagate the pupil field to the focal plane, whereas the WaveTrain™ model uses a 256×256 grid. This difference does not impact Strehl results because pupil plane sampling is constant.

Fade probability results for the higher fidelity WaveTrain™ model are plotted in Figure 4.10. As in the previous section, peak tracking outperforms both AO and centroid tracking. The only significant difference between results in Figure 4.10 and Figure 4.9 is that the AO curve has increased noticeably reflecting poorer performance. AO and centroid tracking now yield nearly identical performance. The effect of scintillation on the more realistic Shack-Hartmann wavefront sensor is the main contributor to this change. However, fitting error between the wavefront and a DM with a limited number of compensated modes is also now included in the simulation. For the strongest turbulence case of $C_n^2 = 1 \times 10^{-16}$ m$^{-2/3}$ and the given threshold, peak tracking is fading 78% less often than an uncompensated system, and 54% and 52% less often than centroid tracking and AO, respectively.

Comparing the results in Figure 4.9 and Figure 4.10 shows that peak tracking performance is not significantly changed by the more realistic sensor frame rate and BSM dynamics included in the WaveTrain™ receiver model. However, the data used

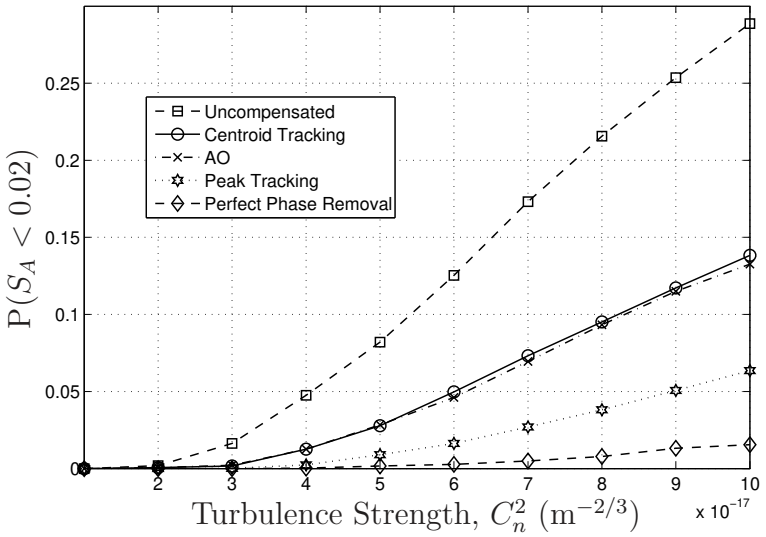

Figure 4.10: Fade probability results for a higher fidelity WaveTrain™ receiver model. Approximately 153,600 data points from 30 0.512 sec simulation runs were used to calculate each value of fade probability using a threshold of $S_A = 0.02$. The scenario is a 100 km path with a 10 m/s uniform crosswind at a wavelength of 1.5 μm.

to calculate the fade probability results in Figure 4.10 does include cases where the mirror jumps from one subspot to another during a single period of image breakup, causing the on-axis point to experience a brief yet significant drop in power. An example of jump-induced fades is presented in Figure 4.11. This result shows S_A for each compensation technique during one occurrence of spot breakup. Note that both centroid tracking and AO suffer the deepest fade due to placement of the central null. Perfect phase removal provides the best performance and serves as an informative upper bound. Peak tracking experiences two abrupt fades in S_A during this period, with both jump-induced fades causing S_A to fall below that of the uncompensated case. However, for this particular example, peak tracking Strehl never falls below that of centroid tracking or AO. The minimum in S_A during the fade for the uncompensated case is significantly greater than the minimum for either centroid tracking or AO. This is due to the on-axis point in the uncompensated case coinciding with the edge of one of two subspots versus near the midpoint. However, in general the uncompensated

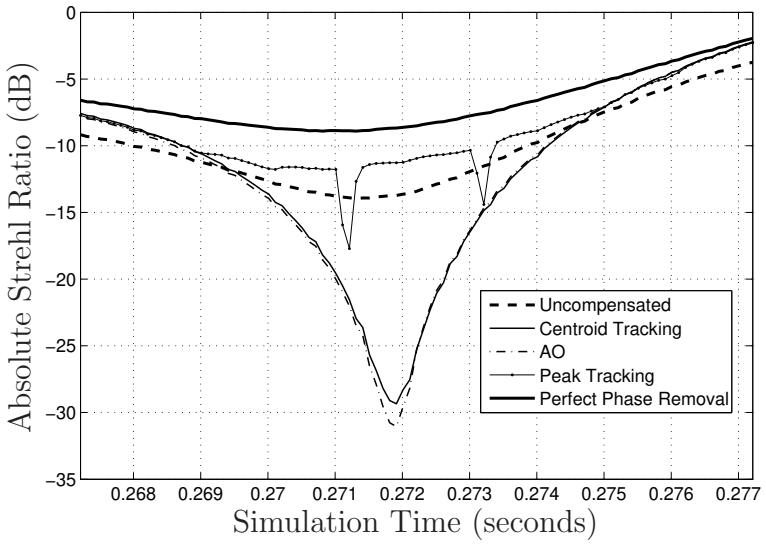

Figure 4.11: Absolute Strehl ratio for a higher fidelity WaveTrain™ receiver using various compensation schemes at a uniform turbulence strength of $C_n^2 = 2 \times 10^{-17}$ m$^{-2/3}$. The scenario is a 100 km path with a 10 m/s uniform crosswind at a wavelength of 1.5 μm. The minimum of the centroid tracking curve corresponds to the focal plane image in Figure 4.7(a).

system provides significant degradation in fade probability performance as seen by the results in Figure 4.10.

A variety of other cases of jump-induced fades have been observed where a jump causes peak tracking S_A to either (a) fall below that of all other compensation techniques, or (b) decrease, but remain higher than all other methods. Overall, it appears that the mirror response time relative to the typical duration of spot breakup is such that jump-induced fades experienced by the peak tracker are not as significant as spot breakup induced fades for centroid tracking and AO. This is the primary reason for the excellent peak tracker performance seen in Figure 4.10 even when more realistic mirror dynamics are incorporated.

4.3.5 Duration and Number of Fades. Up to now, results presented in this chapter demonstrate two important points. First, results in Figures 4.5, 4.6, 4.8, and 4.9 demonstrate that mean Strehl ratio (absolute or relative) is not valid for comparing performance of wavefront control systems when fade probability is the performance

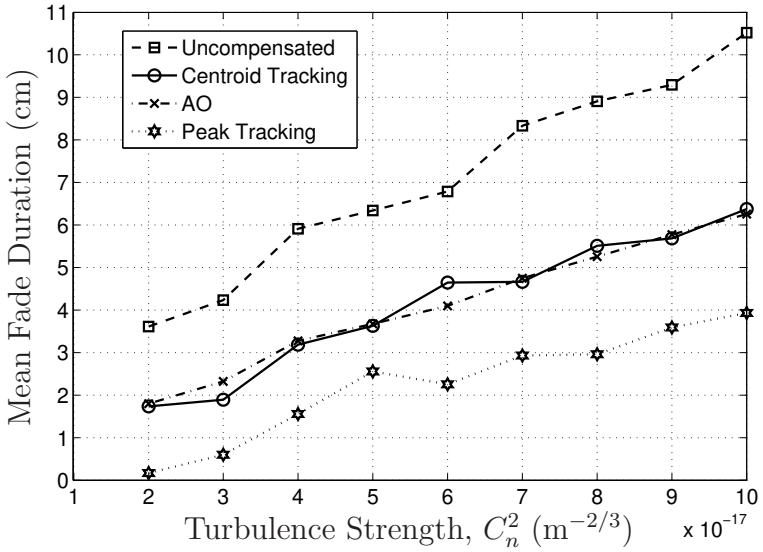

Figure 4.12: Mean fade duration versus turbulence strength for a detection threshold of $S_A = 0.02$. Fade duration results were calculated using data from the higher fidelity WaveTrain™ receiver model.

metric of interest. Second, Figures 4.9 and 4.10 demonstrate that in terms of fade probability, peak intensity tracking outperforms typical centroid tracking and AO systems. This means that metric-driven control of two Zernike modes outperforms MSE-driven control of 23+ modes, i.e., a simpler system yields superior performance.

Results in Figures 4.12 through 4.15 provide additional insight into performance gains afforded by peak tracking, as well as results that will guide the interleaving length selection for FECs. These results were calculated using data from the higher-fidelity WaveTrain™ receiver model. Individual fade periods were identified using an absolute Strehl threshold of 0.02. The duration of each continuous fade period (disjoint from other fade periods) was calculated to the temporal resolution of the simulation. Thus, a vector of fade durations was generated, one for each value of turbulence strength and each compensation technique. Various fade duration statistics were then calculated.

Figures 4.12, 4.13, and 4.14 present average, standard deviation, and maximum fade duration versus turbulence strength, respectively. These results are presented in

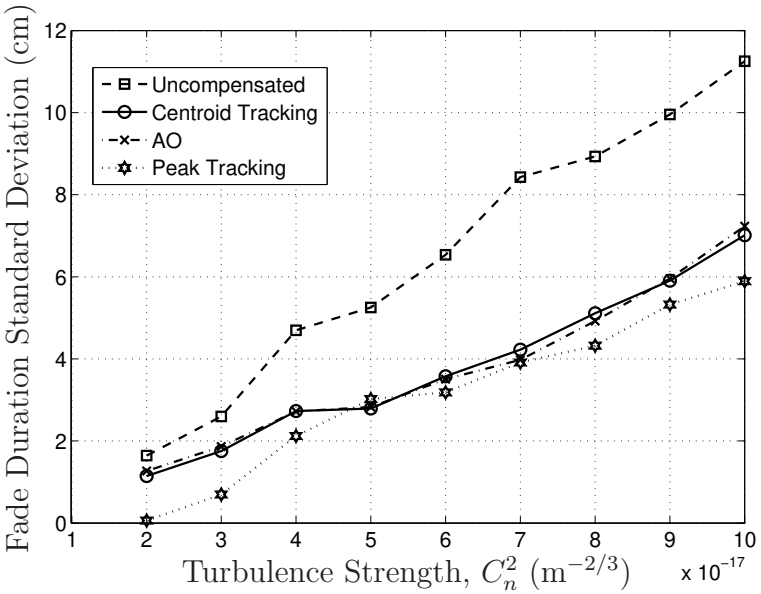

Figure 4.13: Standard deviation of fade duration versus turbulence strength for a detection threshold of $S_A = 0.02$. Fade duration results were calculated using data from the higher fidelity WaveTrain™ receiver model.

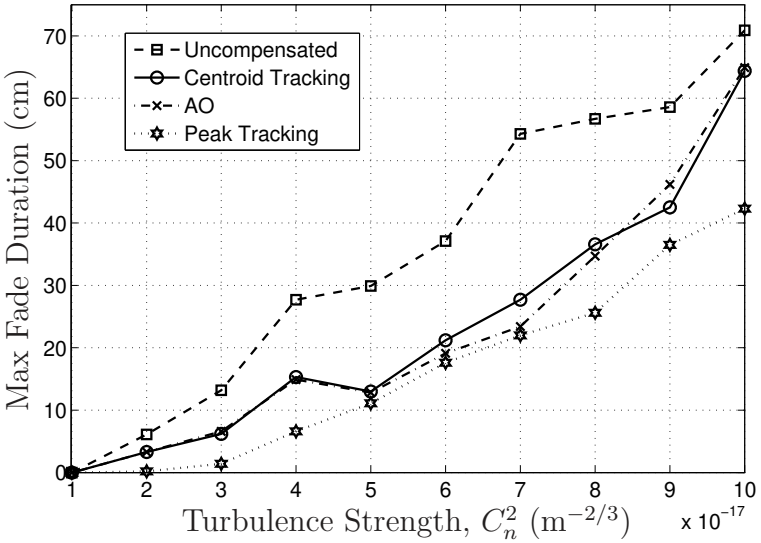

Figure 4.14: Maximum fade duration versus turbulence strength for a detection threshold of $S_A = 0.02$. Fade duration results were calculated using data from the higher fidelity WaveTrain™ receiver model.

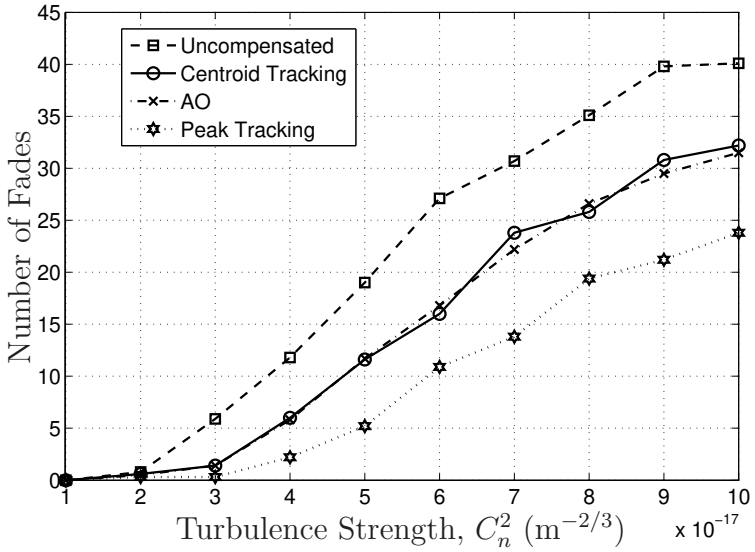

Figure 4.15: Number of fades versus turbulence strength for a detection threshold of $S_A = 0.02$. Results were calculated using data from the higher fidelity WaveTrain™ receiver model. Approximately 153,600 data points from 30 0.512 sec simulation runs were used to calculate each value of fade probability. This corresponds to 15.351 sec of real time per C_n^2 value for a 10 m/s uniform crosswind.

terms of the corresponding amount of (uniform) atmospheric shift relative to the line-of-sight between transmitter and receiver. This distance estimate can be converted to a temporal fade duration by dividing by the (uniform) wind speed. The results in Figures 4.12, 4.13, and 4.14 provide additional insight into the fade probability performance gains due to peak intensity tracking. Figure 4.12 shows that for the peak tracker, the mean fade duration is significantly less than either centroid tracking or AO, as well as the uncompensated case. Figure 4.13 shows that for the peak tracker, the standard deviation of fade duration is less than either centroid tracking or AO for all but one of the C_n^2 values considered. Figure 4.14 indicates that maximum fade duration is somewhat less for the peak tracker than for the other techniques regardless of turbulence strength. The reduction in maximum fade duration due to peak tracking is most apparent for the strongest turbulence scenarios.

Figure 4.15 shows number of fades versus turbulence strength. The number of fades is defined as the number of negative (or positive) threshold crossings. As stated

previously, a threshold of $S_A = 0.02$ was used for all fade results presented in this chapter. The amount of data generated for each value of C_n^2 corresponds to 15.351 seconds of real time. Thus, results for the number of fades in Figure 4.15 could be normalized to give a result in terms of fades per seconds, as is sometimes seen in the literature [8]. This result, combined with the results of Figures 4.12 through 4.14, will guide the interleaving length selection for FECs.

The problem of contiguous bit errors due to atmosphere-induced signal power fades is similar to burst errors in RF wireless communication. Convolutional FEC coding and Viterbi decoding are capable of significant bit error correction capability, but assume random noise, i.e, uncorrelated bit errors. Therefore, data interleaving is used in RF wireless system to effectively change correlated bit error into uncorrelated bit errors. However, a realistic upper limit (near 20 ms) on the interleaving length exists for real-time voice communication to avoid problems such as echo [2]. For LaserCom, the interleaving length would be calculated based on the mean fade duration plus several fade duration standard deviations to provide effective FEC performance. Once again, fade duration results presented in this section are in terms of the corresponding amount of (uniform) atmospheric shift relative to the line-of-sight between transmitter and receiver. This distance estimate is converted to a temporal fade duration by dividing by the (uniform) wind speed. Thus, the results in this section are easily scaled to wind speeds greater than the nominal 10 m/s used in the wave-optics simulations and imply a minimum relative wind speed such that the required interleaving length is less than 20 ms (to maintain effective real-time voice communications). Therefore, for the valid range of wind speeds, the reductions in mean, standard deviation, and maximum fade duration seen in Figures 4.12 through 4.14 imply that peak tracking would reduce decoding delays due to interleaving and FECs. Thus, real-time communication performance would be improved.

4.3.6 Spot Breakup Dynamics. Spot breakup duration is important for system design from the standpoint of sensor frame rate and mirror bandwidth re-

Table 4.5: Characterization of focal plane spot breakup dynamics, where μ_d and σ_d are the mean and standard deviation of breakup duration, respectively, and d represents breakup duration for a threshold of $\lambda/(4D) = 1.875$ μm. The number of breakup periods refers to the number of contiguous periods in time where the centroid-to-peak separation was above threshold. The optical wavelength (λ) is 1.5 μm and the tracking aperture diameter (D) is 20 cm.

C_n^2 ($m^{-2/3}$)	Number of Breakup Periods	μ_d (cm)	σ_d (cm)
1×10^{-17}	N/A	N/A	N/A
2×10^{-17}	27	3.1	3.2
3×10^{-17}	145	3.1	3.5
4×10^{-17}	322	3.6	4.2
5×10^{-17}	478	4.1	4.8
6×10^{-17}	615	4.4	5.1
7×10^{-17}	723	4.8	5.4
8×10^{-17}	798	5.3	6.3
9×10^{-17}	917	5.3	6.7
1×10^{-16}	994	5.4	6.9

quirements, as well as for optimizing FEC performance. Periods of spot breakup were identified by first calculating the difference between centroid and peak intensity locations for all uncompensated focal plane images. This metric provides a single scalar quantity for classifying periods of breakup because visual inspection of more than one million focal plane images is both unrealistic and subjective. Periods when the separation was greater than a given threshold were identified as regions of spot breakup. A threshold of $\frac{\lambda}{4D}$ was chosen as a fraction of the diffraction limit and based on observations of focal plane data showing spot breakup. Contiguous periods of spot breakup were identified, and the duration of each breakup period was recorded. Breakup periods in progress at the beginning or end of a given 0.512 sec continuous data stream were discarded so as not to corrupt results. The mean (μ_d) and standard deviation (σ_d) of breakup duration are presented in Table 4.5.

Similar to fade duration results presented in Section 4.3.5, spot break duration results presented here are in terms of the corresponding amount of (uniform) atmospheric shift relative to the line-of-sight between transmitter and receiver. This

distance estimate can then be converted to a temporal breakup duration by dividing by wind speed for the given scenario. Both breakup duration and number of breakups increase with turbulence strength. This result helps explain the increasing performance of peak tracking relative to centroid tracking seen in Figures 4.9 and 4.10. Clearly, assumptions as to maximum expected wind velocity and platform speed must be made in order to finalize sensor frame rate and FEC selections.

4.4 Closing Remarks

This chapter detailed an investigation of a moderate range air-to-air LaserCom scenario using a performance-metric driven approach to wavefront control. Focal plane spot breakup was identified as the dominant failure mechanism, which occurred even when $D/r_0 < 1$. The impact of spot breakup on average absolute and average relative Strehl was low, but was considerable for fade probability. This demonstrates that optimization of a wavefront control system requires consideration of the performance-metric of interest. Metric-driven design led to exploration of peak intensity tracking as a method to minimize fade probability. Peak tracking provided a significant advantage over both centroid tracking and AO for scenarios studied. When the added fidelity of finite mirror response time and imperfect wavefront sensing was included, peak tracking continued to show excellent benefit, while AO performance degraded considerably. Peak tracking reduced fade probability by greater than 50% over conventional centroid trackers and AO systems. However, a tracking only system is much simpler and smaller, which is an important consideration for tactical systems. At times, the peak tracker jumped from one subspot to another during a single period of image breakup, leading to fade conditions. Modifications to the basic peak tracking algorithm are proposed as future work. Initial investigations show promise for further performance gains. Last, spot breakup dynamics were characterized. For the given uniform crosswind scenario, spot breakup duration is described by the corresponding amount of uniform atmospheric shift. Ultimately, sensor frame rate and mirror

bandwidth requirements for a peak tracking system are largely governed by relative platform speed and wind speed along the propagation path.

4.5 Future Work

There are several promising areas for extending the research. The first is enhancement of the peak tracking algorithm to mitigate the impact of spot jumping on fade probability. The objective is to maximize the minimum power occurring along the path connecting the peak of one subspot to the peak of another. There are basically two approaches that could be taken:

- Adjust the time at which the mirror jumps, and
- Adjust the path taken by the mirror.

This is not a trivial problem because the morphology of spot breakup varies both within a given turbulence strength and across turbulence strength. Further work could be done to understand and characterize aspects of spot breakup morphology relevant to the design of advanced tracking algorithms. Initial work has yielded an algorithm which works well during some breakup conditions, but poorly during others. The ability to predict breakup morphology from previous focal plane images could be very useful. Estimating the location of peak intensity in continuous space from discrete sampling could also be further explored.

Second, incorporation of a peak tracking algorithm with an AO system should be considered. The SRI WFS would be of particular interest for distributed turbulence scenarios of interest. Coupling Efficiency (CE) into a SMF can be estimated by an overlap integral of the incoming complex field and the fundamental mode field of the fiber [102:2447] which can be approximated as Gaussian under certain conditions [85]. Therefore, the optimal pupil plane field to maximize CE is the Fourier transform of the fiber's fundamental mode, which causes CE to exhibit a spatial dependence on the pupil plane phase [86:146]. Accounting for this spatial dependence in system design should result in further performance gains for fiber-coupled systems.

Last, additional work should be done to characterize signal fade and image breakup duration in non-constant C_n^2 scenarios and for non-uniform wind profiles. The entire analysis process used in this chapter could be repeated for a UAV-to-GEO engagement, where an optical communication link may provide an additional means for disseminating surveillance imagery in near real-time.

V. Fade Phenomenology Considerations for System Design

Chapter IV focused on metric-driven control of Zernike tilt modes for fade mitigation. This chapter takes a higher-level system approach to metric-driven wavefront control. A methodology is presented which uses atmospheric turbulence complexity to drive wavefront compensation technique selection.

Section 5.1 provides motivation for this research. Section 5.2.1 describes the focal plane intensity as a convolution of various pupil plane amplitude and phase terms. The relative importance of, and system complexity implied by, each convolution term is addressed in Sections 5.2.2 and 5.2.3. This convolution decomposition leads to the fade classification method presented in Section 5.2.4, which is based on complexity of the required compensation technique. Section 5.3 identifies regions of superior performance, in terms of fade probability, for compensation techniques studied. This section addresses the broader applicability of results presented in Chapter IV. Final conclusions from this effort and directions for future research are presented in Sections 5.4 and 5.5, respectively.

5.1 Motivation and Introduction

Traditional AO systems modify pupil plane phase to improve the focal plane image (satellite imaging) or increase energy on target in the far-field (HEL weapons). Strehl ratio is typically used as the primary performance metric in designing such systems. The "extended Marechal approximation" [44, 89] to the average relative Strehl ratio was presented in (4.15), and is repeated here for reference:

$$E\{S_R\} \simeq e^{-\epsilon^2} \quad . \tag{5.1}$$

The expression in (5.1) assumes that amplitude fluctuations are negligible and is valid when the aperture averaged mean square phase error, ϵ^2, is less than about 4 rad^2. The extended Marechal approximation implies that maximizing average Strehl corresponds to minimizing residual ϵ^2. This result has motivated investigations of AO system optimization based on minimizing residual ϵ^2 [84, 101, 103].

Strehl optimization based on mean square phase is a reasonable approach for imaging and HEL weapon applications, where high resolution imaging or maximum energy on target are desired. Multiple AO error sources have also been formulated in terms of mean square phase. Several examples were presented in Section 3.5, and two of these are repeated here for reference. First, the impact of finite correction system bandwidth on mean square phase error is described by

$$\epsilon^2_{\text{temporal}} = \left(\frac{f_G}{f_{3dB}}\right)^{3/5} \quad , \tag{5.2}$$

where f_G is the Greenwood frequency defined by (3.25) and f_{3dB} is the closed-loop control bandwidth. Second, the impact of a finite degree-of-freedom Deformable Mirror (DM) on mean square phase error is described by

$$\epsilon^2_{\text{fitting}} = \alpha \left(\frac{r_s}{r_0}\right)^{5/3} \quad , \tag{5.3}$$

where r_s is the actuator spacing; r_0 is the Fried parameter, which is related to turbulence strength; and α depends on the form of the actuator influence function. Equation (5.3) was derived based on the error between a LS fit and Kolmogorov turbulence.

Based on (5.2), (5.3), and other results of similar form, advanced systems today often focus on increasing the number of DM actuators and the bandwidth at which corrections can be applied. However, imaging and HEL applications are not typically concerned with very brief drops in power. For applications such as LaserCom, preventing the received power from falling below a detection threshold (during transmission of a 1) is the relevant issue. As an example, for a 1 Gbps LaserCom system, a 1 μs fade corresponds to a duration of 1,000 bits. Tactical LaserCom systems also face significant space, weight, and power limitations on smaller platforms such as UAVs: thus, lower-order, less complex systems are desired. Therefore, unlike many current

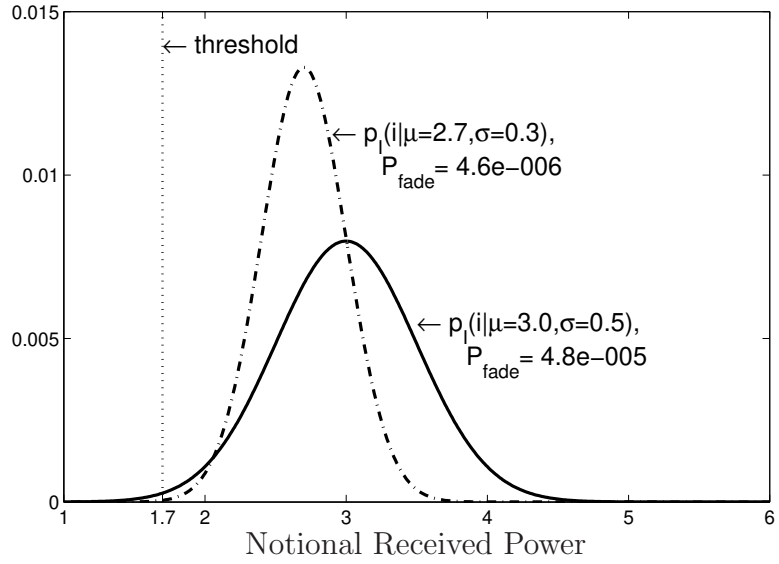

Figure 5.1: Conceptual example of research philosophy: the trade-off of average power and fade probability.

optical systems which are not similarly constrained, the goal is optimal control of a limited number of degrees-of-freedom, in terms of the performance metric of interest.

The divergence of design approaches based on minimizing MSE versus preventing deep signal fades (regardless of tactical system constraints) motivates this research, and leads to consideration of a potential trade-off between average Strehl ratio and fade probability [31]. To visualize this concept, assume that the received optical power is described by one of two Gaussian PDFs depicted in Figure 5.1. Fade probability is defined as the area under the PDF tail left of the threshold. In this conceptual example, the decrease in mean intensity is clearly advantageous (from a LaserCom perspective): A 10% decrease in mean intensity is accompanied by a 40% decrease in variance, resulting in more than an order of magnitude improvement (reduction) in fade probability. In reality, received intensity does not follow a Gaussian distribution. However, results presented in Chapter IV demonstrate that such a tradeoff can be made for the scenario of interest by using peak intensity tracking. This chapter pursues further insights into compensation technique selection based on system complexity, as a function of turbulence strength and detection threshold.

5.2 Complexity-Based System Design

Challenging propagation scenarios result in both amplitude and phase perturbations in the optical field. Values for Rytov variance and D/r_0 presented in Chapter IV indicate that pupil plane amplitude variations are more severe than phase variations for the 100 km air-to-air scenario of interest. For the strongest turbulence considered ($C_n^2 = 1 \times 10^{-16}$ m$^{-2/3}$), values for the Rytov variance and Fried parameter are $\sigma_1^2 = 3.9$ and $r_0 = 13.6$ cm, respectively. This value of σ_1^2 indicates that amplitude fluctuations are in the moderate-to-strong fluctuation range (see Section 2.4.5). For the $D = 20$ cm diameter telescope considered, this value of r_0 gives $D/r_0 = 1.5$. Based on (5.1) and the results of Noll (as in Section 4.3.1), ideal tracking (Zernike tilt removal) increases average S_R by 450% over the uncompensated case, while AO (removal of Zernike modes 2 through 24) increases average S_R by 25% over the tracking case. This indicates that phase variations in the scenario of interest are largely dominated by fluctuations in tip and tilt. Therefore, this is considered a relatively benign scenario in terms of phase fluctuations. However, rare higher-order phase aberrations are a potential concern.

This section mathematically describes the impact of pupil plane phase and amplitude on the instantaneous focal plane intensity profile. Focal plane image examples are presented to help the reader visualize and understand the relative impact of amplitude and phase errors on the focal plane energy distribution. The culmination of this section is a method for classifying fades based on complexity of the required wavefront compensation technique.

5.2.1 Convolution Decomposition of Focal Plane Field. Chapter III developed the mathematical relationship between optical fields in the pupil and focal planes. The result is given in (3.11), which indicates that the two fields are related by a Fourier transform. Fourier transform properties allow (3.11) to be rewritten as

$$I_f\left(\frac{f_X}{\lambda f}, \frac{f_Y}{\lambda f}\right) = \frac{1}{\lambda^2 f^2}\left|\mathcal{F}\left\{A(\xi,\eta)\right\} \circledast \mathcal{F}\left\{e^{j\phi_a(\xi,\eta)}\right\} \circledast \mathcal{F}\left\{P(\xi,\eta)\right\}\right|^2 \quad , \tag{5.4}$$

where ξ and η are coordinates in the pupil plane, f is focal length, λ is optical wavelength, and the focal plane intensity I_f is described in terms of normalized spatial coordinates to simplify notation. Equation (5.4) shows that focal plane intensity (for a coherent source) is proportional to the magnitude of the convolution of three terms. The first term, $\mathcal{F}\{A(\xi,\eta)\}$, is the Fourier transform of the amplitude profile within the pupil. This term accounts for the impact of scintillation, both in terms of spatial variations and fluctuations in total captured power. The second term, $\mathcal{F}\left\{e^{j\phi_a(\xi,\eta)}\right\}$, is the Fourier transform of the phase profile within the pupil. The third and final term, $\mathcal{F}\{P(\xi,\eta)\}$, accounts for the impact of diffraction from a finite aperture. Diffraction represents a physical limit on performance and is not discussed further.

The contribution from pupil plane phase can be decomposed using a modal expansion:

$$\phi(\xi,\eta) = \sum_{n=1}^{\infty} a_n f_n(\xi,\eta) \quad . \tag{5.5}$$

Using a finite sum to approximate the phase surface gives

$$\phi(\xi,\eta) \approx \sum_{n=1}^{N} a_n f_n(\xi,\eta) \quad , \tag{5.6}$$

where N is the number of modes. Truncation errors will depend on the choice of bases set $\{f_n\}$. Substituting (5.6) for ϕ_a in (5.4) gives the following expression for the instantaneous focal plane intensity pattern:

$$I_f(f_X,f_Y) = \frac{1}{\lambda^2 f^2}\left|\mathcal{F}\{A(\xi,\eta)\} \circledast \mathcal{F}\left\{e^{ja_1 f_1(\xi,\eta)}\right\} \circledast \mathcal{F}\left\{e^{ja_2 f_2(\xi,\eta)}\right\} \circledast \cdots \right.$$
$$\left. \circledast \mathcal{F}\left\{e^{ja_N f_N(\xi,\eta)}\right\} \circledast \mathcal{F}\{P(\xi,\eta)\}\right|^2 \quad . \tag{5.7}$$

Zernike polynomials are typically used for optical phase expansion. An alternative is to decompose the phase into two components: Least-Squares (LS) phase and hidden phase. This approach follows the branch point discussion of Section 3.5.2 and

results in the following expression for the focal plane intensity:

$$I_f(f_X, f_Y) = \frac{1}{\lambda^2 f^2} \left| \mathcal{F}\left\{A(\xi,\eta)\right\} \circledast \mathcal{F}\left\{e^{j\phi_{LS}(\xi,\eta)}\right\} \circledast \mathcal{F}\left\{e^{j\phi_{HID}(\xi,\eta)}\right\} \circledast \mathcal{F}\left\{P(\xi,\eta)\right\} \right|^2 \quad . \quad (5.8)$$

Equation (5.8) is central to the results presented in this chapter. The next two sections further discuss specific impacts from the pupil plane amplitude and phase terms. These discussions lead to the complexity based fade classification presented in Section 5.2.4.

5.2.2 Fluctuations in Total Captured Power. Pupil plane amplitude perturbations affect focal plane metrics in two ways. First, there can be significant fluctuations in total power captured by the telescope. Second, spatial variations in the pupil plane amplitude profile impact the corresponding focal plane amplitude profile. This section only addresses fluctuations in total captured power. The next section addresses the spatial variations.

The instantaneous received power captured by the telescope is given by

$$s = \iint_{-\infty}^{\infty} A^2(\xi,\eta) P(\xi,\eta)\, d\xi d\eta \quad , \quad (5.9)$$

where $P(\xi,\eta) = 1$ within the aperture and $P(\xi,\eta) = 0$ elsewhere. To illustrate variations in s caused by turbulence, Figure 5.2 presents total captured power versus time for one segment of the wave-optics simulation data described in Chapter IV. This specific data segment corresponds to a single realization of the ten phase screen 'atmosphere' at a uniform turbulence strength of $C_n^2 = 2 \times 10^{-17}$ m$^{-2/3}$ and a uniform relative wind speed of 10 m/s. The maximum and minimum captured powers for all simulation data at this turbulence strength are 159.4 mw and 1.8 mw, respectively.

Since the metric of interest is fade probability, Figure 5.3 shows the minimum captured power for each value of C_n^2 studied in the simulation. The corresponding

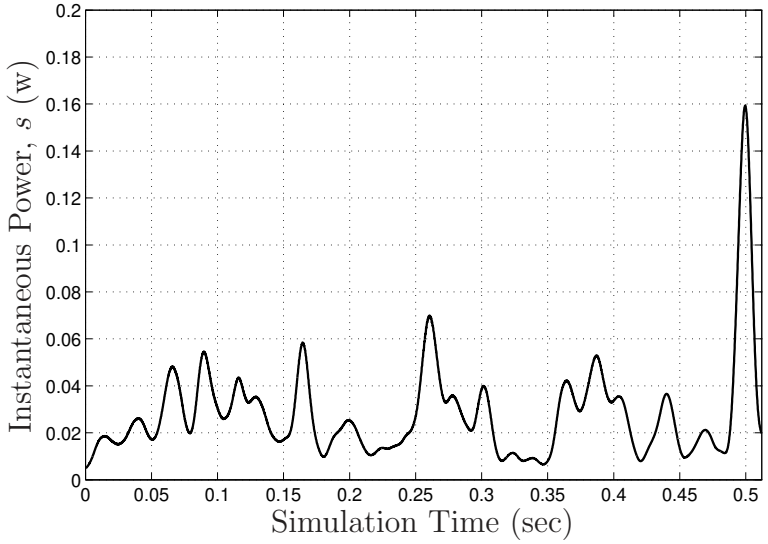

Figure 5.2: Instantaneous received power versus time for a single realization of the ten phase screen 'atmosphere' at a uniform turbulence strength of $C_n^2 = 2 \times 10^{-17}$ m$^{-2/3}$. The scenario is a 100 km path with a 10 m/s uniform crosswind. The receiving telescope is 20 cm in diameter and the wavelength is 1.5 μm.

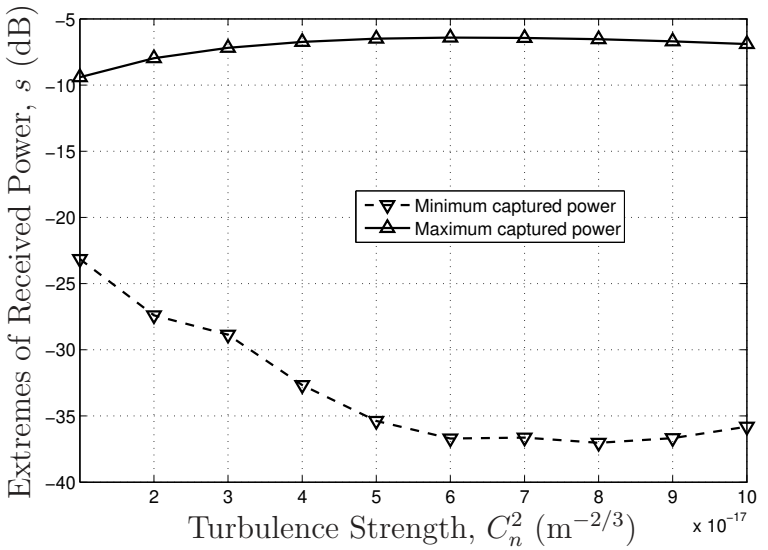

Figure 5.3: Minimum and maximum instantaneous received power versus turbulence strength. Each data point corresponds to the extreme value of 153,600 data points generated using 30 independent realizations of the ten phase screen 'atmosphere' and a 10 m/s wind. The scenario is a 100 km path at a wavelength of 1.5 μm.

maximum values are also displayed. Each data point in Figure 5.3 corresponds to the extreme value of 153,600 data points generated using 30 independent realizations of the ten phase screen 'atmosphere' and a 10 m/s wind. The global minimum occurred for $C_n^2 = 8{\times}10^{-17}$ m$^{-2/3}$, while the global maximum occurred for $C_n^2 = 6{\times}10^{-17}$ m$^{-2/3}$. Notice that the minimum captured power steadily decreases with increasing turbulence strength until $C_n^2 = 6 \times 10^{-17}$ m$^{-2/3}$. For stronger turbulence, the minimum value is nearly the same, and actually increases slightly for the strongest turbulence scenarios studied. This behavior is similar to the saturation in log-amplitude variance seen both in wave-optics simulation and experimental results [20]. This is due to an increasing loss of spatial coherence, which limits the degree of self-interference of the optical field.

In terms of LaserCom performance, fluctuations in total captured power cannot be addressed by wavefront control at the receiver. However, Chapter VI proposes a signal processing approach to mitigate the impact of power fluctuations on bit-error probability. The following section addresses spatial variations in both amplitude and phase.

5.2.3 Spatial Fluctuations in the Pupil Plane Field. In the area of digital image processing, phase is generally more important than amplitude in reconstructing an image [**?**]. Since image quality is not the metric of interest here, it is not clear that this will be the case for LaserCom. Furthermore, the relative impact on fade probability of the LS and hidden portions of the phase are also of interest. Therefore, the complex pupil field associated with the focal plane image breakup presented in Figure 4.7(a) was further examined. This image occurred for a turbulence strength of $C_n^2 = 2 \times 10^{-17}$ m$^{-2/3}$, which corresponds to a log-amplitude variance of 0.19 and a Fried parameter of 33.1 cm ($D/r_0 = 0.61$).

For the pupil field of interest several operations were performed. Each operation relates to one of the convolution terms in (5.8). First, the uncompensated field was propagated to the focal plane. The resulting intensity image is displayed in Fig-

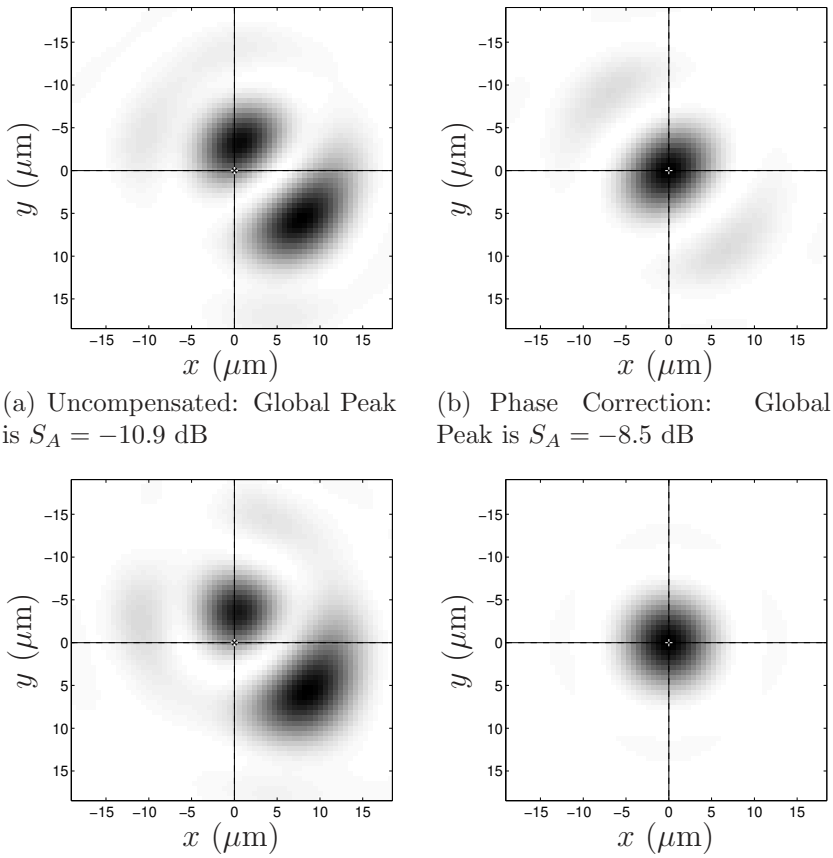

(a) Uncompensated: Global Peak is $S_A = -10.9$ dB

(b) Phase Correction: Global Peak is $S_A = -8.5$ dB

(c) Amplitude Correction: Global Peak is $S_A = -11.4$ dB

(d) Phase and Amplitude Correction: Global Peak is $S_A = -7.6$ dB

Figure 5.4: Focal plane images for various corrections to the pupil plane field and a uniform turbulence profile of $C_n^2 = 2 \times 10^{-17}$ m$^{-2/3}$. The atmospheric random seed is 3 and the image is frame 2719 of 5120. The scenario is a 100 km path with a 10 m/s uniform crosswind.

ure 5.4(a). Second, the perturbed pupil phase was replaced with a uniform phase which models ideal phase compensation. The modified field was propagated to the focal plane and the resulting intensity image is displayed in Figure 5.4(b). This case corresponds to complete removal of both the LS and hidden phase terms in (5.8). Third, the perturbed amplitude profile was replaced with a uniform amplitude (while conserving energy). The modified field was propagated to the focal plane and the resulting image is displayed in Figure 5.4(c). This case corresponds to removing all spatial fluctuations in the amplitude convolution term, resulting in a constant am-

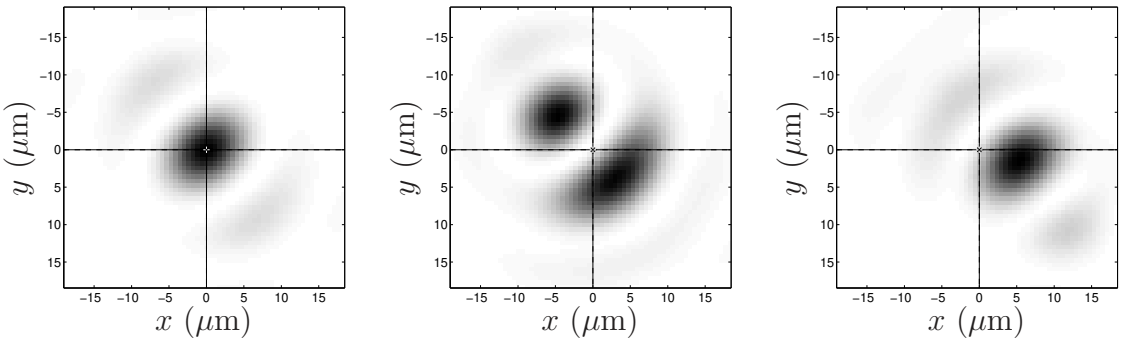

(a) Total Phase Correction: Global Peak is $S_A = -8.5$ dB

(b) LS-phase Correction: Global Peak is $S_A = -11.1$ dB

(c) Hidden Phase Correction: Global Peak is $S_A = -9.1$ dB

Figure 5.5: Focal plane images for various corrections to the pupil plane phase and a uniform turbulence profile of $C_n^2 = 2 \times 10^{-17}$ m$^{-2/3}$. The scenario is a 100 km path with a 10 m/s uniform crosswind.

plitude across the telescope aperture. However, energy was conserved in calculating the constant amplitude so that fluctuations in total captured power are still present. Finally, the image resulting from both amplitude and phase correction is presented in Figure 5.4(d) which is the ideal diffraction limited Airy pattern.

This experiment at least partially validates the intuition that amplitude errors are less critical than phase errors. Figure 5.4 demonstrates that for the pupil field considered, ideal phase correction causes the broken image to merge into one spot, while ideal (spatial) amplitude correction does not. However, spatial amplitude variations are not the same as fluctuations in total captured energy, which is a serious issue for performance as discussed in the previous section.

The next step is to further decompose the phase contribution in accordance with (5.8). Therefore, the impact of LS and hidden phase components are considered individually. First, the focal plane image resulting from ideal phase correction was presented in Figure 5.4(b) and is displayed again in Figure 5.5(a) for reference. Second, the LS portion of the perturbed pupil phase was replaced with a uniform phase. The modified field was propagated to the focal plane and the resulting intensity image is displayed in Figure 5.5(b). This case corresponds to complete removal of the LS phase term in (5.8). Third, the hidden portion of the perturbed pupil

phase was replaced with a uniform phase. The modified field was propagated to the focal plane and the resulting intensity image is displayed in Figure 5.5(c). This case corresponds to complete removal of the hidden phase term in (5.8).

Results in Figure 5.5 provide important insight into the results of Chapter IV, as well as directions for future work. As expected, ideal pupil plane phase correction results in a global peak value in the focal plane which is greater than global peaks for either LS or hidden phase corrections alone. The global peak for LS-phase removal is less than for either ideal or hidden phase correction, as well as for the uncompensated case. This makes sense because the image remains separated into two distinct spots as in the uncompensated image. Thus, the energy is split between two separate spots with both approximately the same size as the Airy disk. The most interesting observation is that removal of only the hidden (i.e., branch point) portion of the phase causes the two original spots to merge into one. However, there is still some residual global phase tilt, and thus the new single spot is shifted away from the optical axis. This result helps explain the improvement due to peak tracking shown in Chapter IV. Removal of the LS-phase performs nearly the same as centroid tracking due to the small values of D/r_0, and causes the low-intensity point between the two peaks to be placed on the optical axis. By tracking a single peak, this is avoided. However, some performance is still lost due to energy being shared with the other spot.

5.2.4 Complexity-Based Fade Classification. A fade can result from amplitude and/or phase perturbations caused by propagation through turbulence. The typical modal-based decomposition of turbulence-perturbed phase [64] does not reveal the optimal compensation technique for all metrics and design constraints of interest. Therefore, a complexity-based decomposition for fade classification was developed and is depicted in Figure 5.6.

For a given fade, the first step is to determine whether performance is limited by phase errors or captured power. If sufficient power is captured by the aperture to theoretically achieve the desired performance, then the signal is phase error limited.

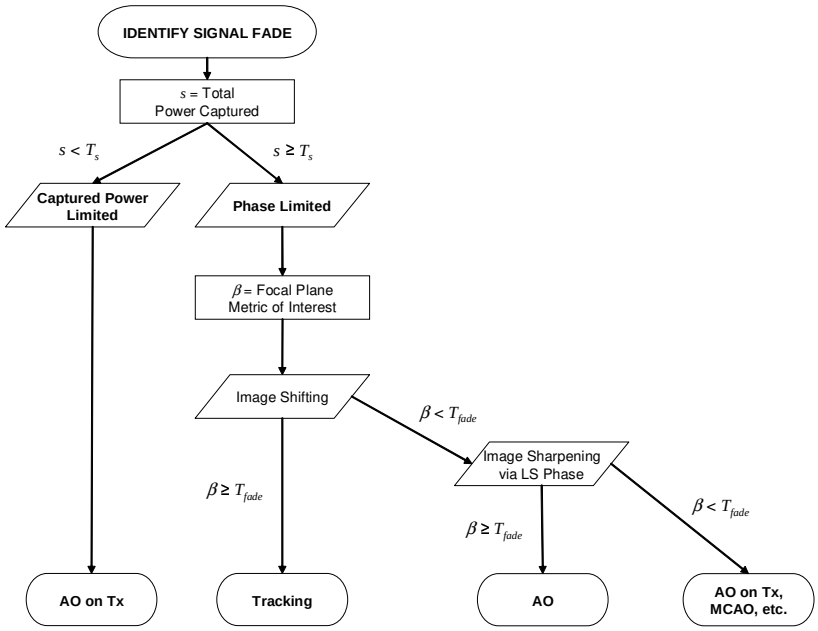

Figure 5.6: Complexity-based classification of turbulence induced signal fades.

Otherwise, the captured signal is power limited and cannot be corrected by wavefront control at the receiver. This case would require an increase in transmitter power and/or incorporation of AO in the transmitting telescope. Mathematically, the initial decomposition is expressed as

$$s \geq T_s \implies \text{phase limited} \tag{5.10}$$

or

$$s < T_s \implies \text{captured power limited} \quad , \tag{5.11}$$

where s is total power captured by the telescope and T_s is the *captured power threshold*. T_s is defined as the minimum captured power required to meet a given BER value. Throughout this section, s is defined to be an average over numerous atmospheric cases, and thresholds T are defined by system parameters and a desired BER. While this discussion is based on a single frame of data, system design would be based on results of multiple individual frames.

As depicted in Figure 5.6, phase limited signals are further decomposed. First, if a simple shifting of the focal plane field will meet the BER requirement, then tracking is the least complex solution. Mathematically, the corresponding pupil plane phase correction is given by

$$\phi_{BSM} \neq C_{tilt} \tag{5.12}$$

$$\phi_{BSM} = aZ_2 + bZ_3 \ni [a,b] = \arg\left\{\max_{a,b}\left[MOI\left(\phi_{BSM}\right)\right]\right\} \quad , \tag{5.13}$$

where C_{tilt} is pupil plane tilt derived from the focal plane image centroid, and $MOI(\phi_{BSM})$ is the value of the focal plane metric of interest (Strehl, coupling efficiency, etc.) for a given beamsteering correction in the pupil plane. If beamsteering does not push the signal above threshold, then higher-order phase correction is required to sharpen the image (i.e., redistribute focal plane energy). If removal of the LS portion of the phase will push the signal above threshold, then traditional single DM (continuous face-sheet) AO should be considered. Mathematically, the corresponding pupil plane phase correction is

$$\phi_{DM} = -\phi_{LS} \quad , \tag{5.14}$$

where the perturbed pupil plane field is given by $A\exp\{j(\phi_{LS} + \phi_{BP})\}$, and ϕ_{BP} is the branch point, or hidden, portion of the phase. If removal of the LS-phase does not push the signal above threshold, then the hidden phase must be at least partially corrected. This requires consideration of a more complex system and advanced AO techniques and hardware, such as Multi-Conjugate AO (MCAO) and spatial light modulators (liquid crystal, MEMS, etc.), or possibly AO at the transmitter.

This approach to fade classification identifies the least complex solution for meeting given fade probability (P_{fade}) and BER requirements, and guides the approach for mitigating fades. The relative importance of the different phase and amplitude components may vary depending on the propagation scenario. For the peak

intensity tracking results presented in Chapter IV, a relatively small aperture, moderate range LaserCom scenario was examined. Within the context of the fade classification architecture, the focus of Chapter IV was phase-limited fades correctable via beamsteering. Spot breakup was observed for $D/r_0 < 1$ and identified as the primary failure mechanism for phase-limited fades in the scenarios studied.

5.3 Regions of Superior Performance

The previous section presented a method for classifying fades based on complexity of the required wavefront compensation. This section identifies which of the wavefront control techniques previously discussed provides superior performance, in terms of minimal fade probability, for the 100 km air-to-air scenario of interest. Therefore, P_{fade} was calculated for each compensation technique considered in the previous section using the wave-optics simulation data described in Chapter IV. P_{fade} was calculated for a range of fade threshold values in terms of S_A, which is normalized to the on-axis intensity resulting from vacuum propagation. P_{fade} values were then available as a function of three parameters: wavefront control technique, turbulence strength, and normalized detection threshold.

For a given turbulence strength, P_{fade} can be plotted as a function of normalized detection threshold (i.e., S_A) for various wavefront control methods. The remaining results only consider three techniques: LS-phase removal, centroid tracking, and peak intensity tracking. LS-phase removal provides an upper bound on the performance of a traditional AO system using a LS reconstruction algorithm. Centroid tracking is also included because it is the typical and most straightforward algorithm for controlling Zernike modes two and three. Figure 5.7 presents P_{fade} results for these three techniques using the strongest turbulence considered, $C_n^2 = 1 \times 10^{-16}$ m$^{-2/3}$. These results highlight distinct regions of superior performance for the three techniques. For larger values of fade threshold ($S_A \gtrsim 0.1$) all three techniques provide nearly identical performance in terms of fade probability. However, a closer inspection of the data reveals that AO slightly outperforms both centroid and peak intensity tracking in

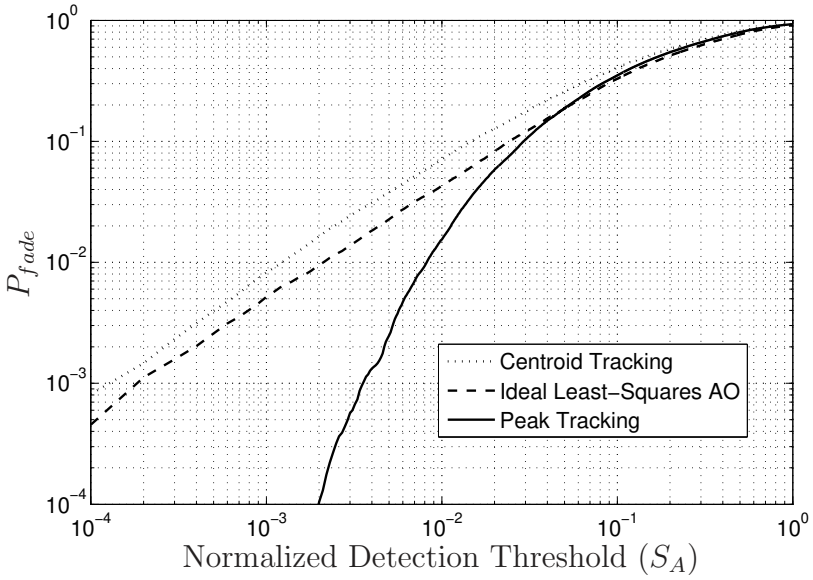

Figure 5.7: Fade probability P_{fade} versus normalized detection threshold (in terms of absolute Strehl) for three wavefront control techniques. The strength of the uniform turbulence profile is $C_n^2 = 1 \times 10^{-16}$ m$^{-2/3}$.

this region. For smaller fade thresholds ($S_A \lesssim 0.05$), as would be applicable to a real OOK LaserCom system, peak tracking outperforms both AO and centroid tracking. Furthermore, the relative improvement provided by peak tracking increases with decreasing normalized fade threshold. In this same region, AO provides a consistent improvement relative to centroid tracking, reducing P_{fade} by 24 to 44%.

Results in Figure 5.7 indicate a crossover point defining a region of superior performance for peak tracking compared to centroid tracking and ideal LS AO. The crossover point was numerically estimated for each value of C_n^2 studied and the resulting boundary is plotted in Figure 5.8. This result identifies the region for superior performance, in terms of fade probability, for peak intensity tracking as compared to ideal LS AO. The boundary of the performance dominance region is nearly invariant to turbulence strength for $C_n^2 \geq 3 \times 10^{-17}$ m$^{-2/3}$, and approximately equal to $S_A = 0.04$ in this turbulence region. Recall from (3.16) that $S_A = 0.04$ indicates an on-axis intensity in the focal plane which is 4% of the vacuum propagation result. The boundary begins to increase slightly for the weaker turbulence scenarios.

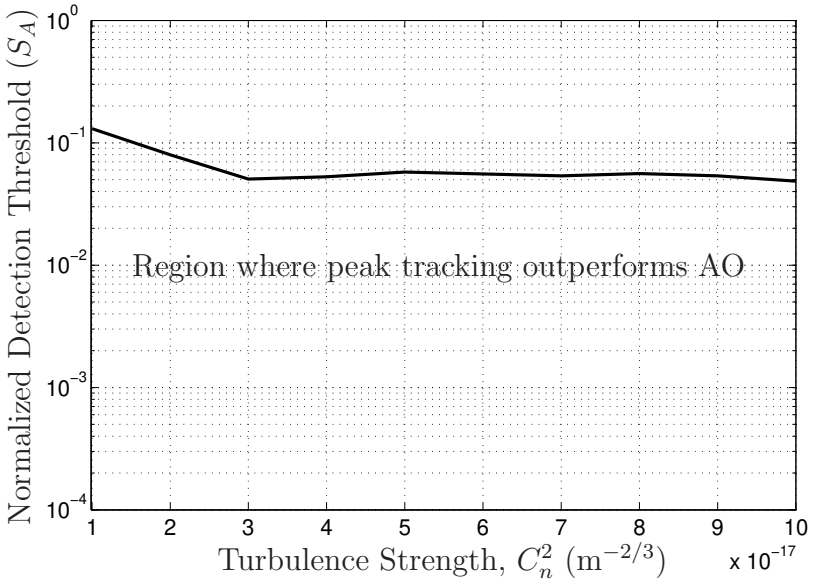

Figure 5.8: Regions of superior performance, in terms of fade probability, for peak tracking and AO.

Thus, for a given atmospheric turbulence strength and normalized detection threshold smaller than the crossover point, the optimal compensation technique is known. If the threshold requirement changes due to changes in system parameters or communication range, this boundary informs the designer as to the optimal algorithm selection.

5.4 Closing Remarks

This chapter defined an architecture to further examine regions of operation for various atmospheric compensation techniques based on deep fade phenomenology. Fades are classified based on complexity of the required compensation technique. For compensation techniques studied, regions of superior performance are identified in terms of fade probability as a function of detection threshold. Peak tracking outperforms ideal LS AO for normalized thresholds below approximately 4% of the unabberated on-axis intensity in the focal plane. Furthermore, the fade threshold boundary defining a region of superior performance for peak tracking (relative to ideal LS AO) is nearly invariant to turbulence strength for $C_n^2 \geq 3 \times 10^{-17}$ $m^{-2/3}$. Boundary in-

variance would simplify operation of a composite system able to adaptively select compensation methodology in real-time.

5.5 Future Work

The result of Figure 5.5 helps visualize and explain the performance gains due to peak tracking demonstrated in Chapter IV. This result also leads to consideration of a potential advanced system that removes the hidden portion of phase while tracking peak intensity. However, if it could be shown that removal of the hidden phase always causes the broken spots to merge, traditional centroid tracking could be used instead of peak tracking. The self-referencing interferometer WFS sensor could be combined with advanced spatial light modulator technology for a potential implementation of such an advanced system. The other most promising area for extending the research would be to repeat the analysis in this chapter for other atmospheric and engagement scenarios, such as a potential UAV-to-GEO communication uplink. The analysis could also be extended to a two-way propagation scenario with AO at the transmitter. Fade phenomenology could then be studied at the receiver as a function of wavefront control technique at the transmitter.

VI. Adaptive Thresholding

While Chapters IV and V considered physical modification of the wavefront phase, this chapter takes a signal processing approach to improve performance. Furthermore, the focus on wavefront control up to this point has not required a full model of the detection noise processes. This chapter develops an adaptive binary decision threshold optimized to mitigate the impact of scintillation and detector noise on BER.

Section 6.1 describes basic digital communication and presents an optical receiver model for OOK direct-detection. Detection noise sources considered in the investigation are also defined. Section 6.2 reviews binary decision theory. BER expressions are then formulated for several cases of increasing complexity, culminating in the case which accounts for signal dependent noise, scintillation, and an adaptive decision threshold. Section 6.3 derives an optimal fixed threshold for several cases based on minimizing BER. These results provide a means for comparing the fixed and adaptive techniques, as well as a method to calculate the adaptive threshold from mean signal current. Section 6.4 addresses necessary considerations prior to calculating numeric results. Analytic results are presented in Section 6.5, beginning with an optimal fixed threshold value for each value of turbulence strength (C_n^2). BER results for adaptive and optimal fixed thresholds are then presented, based on best-fit gamma-gamma PDFs and the results of Section 6.2. Section 6.6 presents Monte Carlo simulation results that validate the analytic BER results. Adaptive threshold estimation error is also quantified. Last, conclusions from this effort and directions for future research are presented in Sections 6.7 and 6.8, respectively. Results presented in this chapter do not assume fiber-coupled detection or wavefront control at receiver. However, adaptive thresholding could be readily combined with a variety of detector and wavefront control architectures.

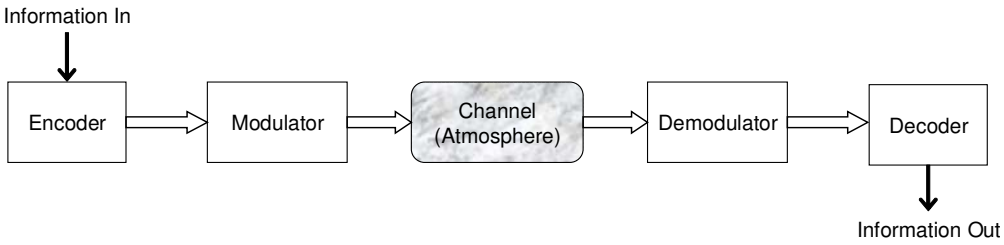

Figure 6.1: Major components of a digital communication system.

6.1 Digital Communication

The major components of a digital communication system are presented in Figure 6.1 [90]. The modulator converts bits to symbols prior to transmission through the channel. In the case of LaserCom, the channel is the stochastic atmosphere, whereas in fiber optics it is a well characterized glass fiber. For the OOK system considered here, the relationship between bits and symbols is one-to-one. The symbols for a 1 and 0 are simply the "on" and "off" states of the laser source, respectively. The encoder and decoder implement Forward Error-Correction (FEC) codes to decrease BER for a fixed transmitter power. Example FECs include linear block, convolutional, Reed-Solomon, and turbo codes [43,90]. FEC codes are not considered in this investigation for the following reasons. First, the focus of this work is the channel. Second, convolutional and turbo-codes are capable of significant performance improvement, but suffer from decoding delays - a drawback for real-time communication [43].

6.1.1 Optical Binary Receiver Model. The optical binary receiver model used for this investigation is described by Figure 6.2. A filter of bandwidth B follows the detector, where B is chosen to match the frequency content of the incoming signal. The output from the filter is

$$i = i_S + i_N \quad , \tag{6.1}$$

where i_S and i_N are the signal and noise currents, respectively. The signal current is defined by

$$i_S = \frac{\eta e s}{h\nu} \quad , \tag{6.2}$$

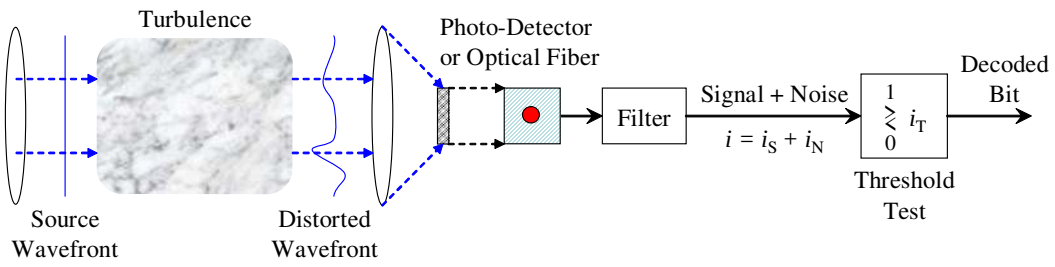

Figure 6.2: Optical binary receiver model for direct-detection digital communication.

where s is optical power captured by the telescope (watts), η is quantum efficiency (electrons/photon), $e = 1.602 \times 10^{-19}$ C is the elementary electric charge, $h = 6.626 \times 10^{-34}$ J·s is Planck's constant, and ν is optical frequency (Hz). Note that the product $h\nu$ gives the energy in joules represented by a single photon. The signal current given by (6.2) is assumed to be constant during any given integration period corresponding to a single bit. Comparing the frequency of atmospheric change ($<$ kHz) with bandwidths studied ($>$ MHz), this is a reasonable assumption. The noise current is described in detail in the next section.

6.1.2 Noise Sources. There are several potential noise sources in the optical detection process, such as: electronic thermal (or Johnson) noise, photon (or shot) noise, generation recombination noise, $1/f$ noise, background noise, dark current, etc. [32]. For typical systems, Johnson and shot noise dominate. Thus, these are the only two detection noise terms considered:

$$i_N = i_{elec} + i_{shot} \quad . \tag{6.3}$$

Shot noise is due to the random arrival times of individual photons, or conversely, the random emission times of photoelectrons. Johnson noise is due to thermal motion of electrons across a resistor.

The statistics of shot noise are fundamentally Poisson, but if the signal level is large enough, a Gaussian PDF is a good approximation [4]. To determine if a

Gaussian PDF is applicable to this research, the minimum received signal power must be estimated. The minimum captured power for all wave-optics simulation data initially generated for results presented in Chapter IV was 198 μw, which occurred for $C_n^2 = 8 \times 10^{-17}$ m$^{-2/3}$. Incorporating an additional constant loss factor of -57 dB due to estimated optical surface losses, atmospheric attenuation, longer paths, reduced transmitter power, smaller receiving aperture, etc. [4], the global minimum received power is 663 nw. The corresponding photons per bit is calculated as

$$\text{Photons Per Bit} = \frac{s\tau}{h\nu} \quad , \tag{6.4}$$

where τ is the temporal bit duration (sec). For the minimum captured power and a bit rate of 10.0 Gbps ($\tau = 0.1$ ns), the corresponding minimum photons per bit is 500. Furthermore, as the captured power approaches zero, the signal and shot noise currents will also approach zero. Therefore, shot noise current statistics are well approximated as a zero-mean Gaussian [4, 8]:

$$p(i_{shot}) = \frac{1}{\sqrt{2\pi}\sigma_{shot}} \exp\left\{-\frac{i_{shot}^2}{2\sigma_{shot}^2}\right\} \quad , \tag{6.5}$$

where the mean square current due to shot noise is given by [32:173]

$$E\{i_{shot}^2\} = \sigma_{shot}^2 = 2eBi_S \tag{6.6}$$

$$= \frac{2\eta e^2 Bs}{h\nu} \quad , \tag{6.7}$$

where B is signal bandwidth. Note that shot noise current is signal level dependent.

Johnson noise current is typically modelled as a zero mean Gaussian random variable, with mean square current given by [32:171]

$$E\{i_{elec}^2\} = \sigma_{elec}^2 = \frac{4KTB}{R} \quad , \tag{6.8}$$

where $K = 1.381 \times 10^{-23}$ joules/kelvin is Boltzmann's constant, T is temperature of the electronics (kelvin), and R is the effective input resistance (ohms). The statistics of Johnson noise are described by

$$p(i_{elec}) = \frac{1}{\sqrt{2\pi}\sigma_{elec}} \exp\left\{-\frac{i_{elec}^2}{2\sigma_{elec}^2}\right\} \quad . \tag{6.9}$$

The total detector current is now given by

$$i = i_S + i_{shot} + i_{elec} \quad . \tag{6.10}$$

The noise sources are assumed to be independent. Therefore, the mean current is

$$\begin{aligned} E\{i\} &= E\{i_S\} + E\{i_{shot}\} + E\{i_{elec}\} & (6.11)\\ &= i_S \quad , & (6.12) \end{aligned}$$

and the variance is due only to the detection noise terms:

$$\begin{aligned} \sigma_i^2 &= \sigma_{shot}^2 + \sigma_{elec}^2 & (6.13)\\ &= \frac{2\eta e^2 Bs}{h\nu} + \frac{4KTB}{R} \quad . & (6.14) \end{aligned}$$

Furthermore, since a sum of Gaussian random variables is also a Gaussian random variable, the total detector current is described by a Gaussian distribution:

$$p(i) = \frac{1}{\sqrt{2\pi}\sigma_i} \exp\left\{-\frac{(i - i_S)^2}{2\sigma_i^2}\right\} \quad . \tag{6.15}$$

6.2 Binary Decision Problem and Bit-Error Rate Formulation

Figure 6.3 depicts the basic binary decision problem [67]. The function $p_0(i)$ is the *a priori* PDF for the null hypothesis, corresponding to the case that a 0 was transmitted. The function $p_1(i)$ is the *a priori* PDF for the simple alternate hypothesis, corresponding to the case that a 1 was transmitted. The results of Section 6.1.2

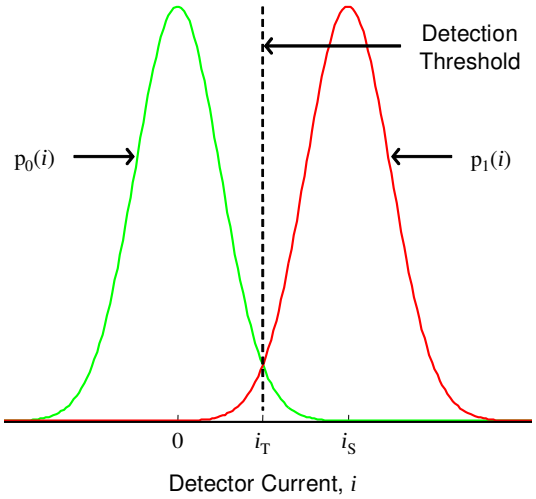

Figure 6.3: Illustration of the basic binary decision problem. The Gaussian function on the left, $p_0(i)$, is the *a priori* PDF for the null hypothesis, which corresponds to transmission of a 0. The Gaussian function on the right, $p_1(i)$, is the *a priori* PDF for the simple alternate hypothesis, which corresponds to transmission of a 1.

are used to formulate a binary decision problem applicable to LaserCom. The assumption is made that no optical power reaches the detector during transmission of a zero. The current generated by the receiver is expressed as a pair of conditional Gaussian PDFs: $p_0(i)$, the probability of detector current, i, given a zero was sent and $p_1(i)$, the probability of detector current given a one was sent, where

$$p_0(i) = \frac{1}{\sqrt{2\pi}\sigma_{elec}} \exp\left\{-\frac{i^2}{2\sigma_{elec}^2}\right\} \tag{6.16}$$

and

$$p_1(i) = \frac{1}{\sqrt{2\pi}\sigma_i} \exp\left\{-\frac{(i-i_S)^2}{2\sigma_i^2}\right\} \quad . \tag{6.17}$$

where σ_{elec}^2 is given by (6.8), i_S is given by (6.2), and σ_i^2 is given by (6.14). BER expressions are now formulated for several cases of increasing complexity, culminating in the case which accounts for signal dependent noise, scintillation, and an adaptive decision threshold.

6.2.1 Fixed Threshold without Scintillation. In the absence of scintillation (i.e., fixed signal level), the probability of a bit-error (i.e., BER) is expressed as

$$P_e = P(0)\int_{i_T}^{\infty} p_0(i)di + P(1)\int_{-\infty}^{i_T} p_1(i)di \quad , \tag{6.18}$$

where $P(0)$ and $P(1)$ are the *a priori* probabilities for transmissions of a zero or one, respectively, and i_T is the fixed decision threshold in terms of detector current. Numerically, (6.18) is defined as the number of bits in error divided by the total number of bits transmitted. Equation (6.18) is common to discussions of binary decision theory [4, 8, 38, 67, 90]. The first term in (6.18) is often called the Probability of False Alarm (P_{FA}), while the second is called the Probability of Missed Detection (P_{MD}) [67].

6.2.2 Fixed Threshold with Scintillation. The impact of scintillation is to vary i_S. To include this variation, $p_1(i)$ must be conditioned on the received optical power. Extending the approach of Andrews, Phillips, and Hopen [8]:

$$P_e = P(0)\int_{i_T}^{\infty} p_0(i)di + P(1)\int_{0}^{\infty}\int_{-\infty}^{i_T} p_1(i|s)p(s)dids \quad , \tag{6.19}$$

where $p_1(i|s)$ is the PDF of detector current during transmission of a 1 conditioned on the optical power, s, captured by the telescope. To find the total error probability, the PDF describing atmosphere-induced power fluctuations, $p(s)$, is weighted by the conditional fade probability and integrated over all possible values of s.

Equation (6.19) is now simplified to calculate subsequent results. All numeric results presented in this chapter assume that a 0 and 1 are equally likely so that $P(1) = P(0) = 1/2$. Further, substitution of (6.16) and (6.17) into (6.19) gives

$$\begin{aligned} P_e = \frac{1}{2}\int_{i_T}^{\infty} \frac{1}{\sqrt{2\pi}\sigma_{elec}} \exp\left\{-\frac{i^2}{2\sigma_{elec}^2}\right\} di \\ + \frac{1}{2}\int_{0}^{\infty}\int_{-\infty}^{i_T} \frac{1}{\sqrt{2\pi}\sigma_i(s)} \exp\left\{-\frac{[i - i_S(s)]^2}{2\sigma_i^2(s)}\right\} p(s)dids \quad , \end{aligned} \tag{6.20}$$

where the dependence of the mean and variance of detector current on captured optical power (during transmission of a 1) is explicit to avoid confusion.

The integrals cannot be evaluated analytically, but (6.20) is simplified prior to numeric evaluation using the Gaussian error, and complementary error, functions. To maintain consistency with `Matlab`®, the following definitions are assumed:

$$\text{erf}(x) = \frac{2}{\sqrt{\pi}} \int_0^x e^{-t^2} dt \tag{6.21}$$

and

$$\begin{aligned} \text{erfc}(x) &= \frac{1}{2} - \text{erf}(x) & (6.22) \\ &= \frac{2}{\sqrt{\pi}} \int_x^\infty e^{-t^2} dt \quad . & (6.23) \end{aligned}$$

Making a change of variables and using (6.21) and (6.23), the probability of error is expressed as

$$P_e = \frac{1}{4} + \frac{1}{4}\text{erfc}\left[\frac{i_T}{\sqrt{2}\sigma_{elec}}\right] + \frac{1}{4}\int_0^\infty \text{erf}\left[\frac{i_T - i_S(s)}{\sqrt{2}\sigma_i(s)}\right] p(s) ds \quad . \tag{6.24}$$

6.2.3 Adaptive Threshold with Scintillation. For the final BER formulation, an adaptive threshold is assumed. Therefore, the decision threshold becomes a function of captured power. To start, (6.18) is rewritten as

$$P_{e|s} = P(0) \int_{i_T(s)}^\infty p_0(i) di + P(1) \int_{-\infty}^{i_T(s)} p_1(i|s) di \quad . \tag{6.25}$$

Unlike the fixed threshold case, the terms corresponding to P_{FA} and P_{MD} are both dependent on captured optical power. To find the total error probability, (6.25) is weighted by the PDF describing atmosphere-induced power fluctuations, and inte-

grated over all possible values of s:

$$P_e = \int_0^\infty P_{e|s} p(s) ds \tag{6.26}$$

$$= P(0) \int_0^\infty \int_{i_T(s)}^\infty p_0(i) p(s) di ds + P(1) \int_0^\infty \int_{-\infty}^{i_T(s)} p_1(i|s) p(s) di ds \, . \tag{6.27}$$

Once again, the error and complementary error functions given by (6.21) and (6.23) are used to simplify the expression for BER, resulting in

$$P_e = \frac{1}{4} + \frac{1}{4} \int_0^\infty \text{erfc} \left[\frac{i_T(s)}{\sqrt{2}\sigma_{elec}} \right] p(s) ds + \frac{1}{4} \int_0^\infty \text{erf} \left[\frac{i_T(s) - i_S(s)}{\sqrt{2}\sigma_i(s)} \right] p(s) ds \quad , \tag{6.28}$$

where $i_T(s)$ is the adaptive decision threshold.

6.3 Optimal Fixed Decision Threshold

This section develops an optimal fixed decision threshold for three separate cases. First, Section 6.3.1 considers the simplest case which ignores scintillation and signal dependant noise. This case serves as a validation point for the more general result derived in Section 6.3.2, which accounts for signal dependent noise. The result of Section 6.3.2 does not account for scintillation, but provides a method to calculate the adaptive threshold. Last, Section 6.3.3 considers the impact of scintillation on the fixed threshold selection. The optimal fixed threshold cannot be solved for directly in this case. However, a constraint equation is produced, which can be used to numerically solve for the optimal fixed threshold for a given PDF describing the turbulence-induced power fluctuations.

6.3.1 Equal Variance without Scintillation. In the case where the *a priori* densities for noise and signal-plus-noise have the same variance, the optimum fixed threshold is simply the midpoint between the two means. Both densities having the same variance implies signal independent noise. For the current notation, the threshold in this case is $i_T = i_S/2$. This common result can be found by setting

$dP_e/di_T = 0$ and using the Leibnitz Rule (see following subsection) or by a maximum likelihood approach [90]. This result serves as a validation point for the following derivation in Section 6.3.2.

6.3.2 Unequal Variance without Scintillation. The more general case accounting for signal dependent noise is now considered. In this case, the two *a priori* densities illustrated by Figure 6.3 no longer have the same variance, and the threshold value minimizing BER is no longer obvious. The *a priori* densities for noise and signal-plus-noise are now assumed to be given by (6.16) and (6.17). The optimum threshold which minimizes the probability of bit-error is found by finding $dP_e/di_T = 0$ and solving for i_T (assuming this is not a maximum). Starting with BER as given by (6.18) gives

$$\frac{dP_e}{di_T} = \frac{d}{di_T}\left[P(0)\int_{i_T}^{\infty} p_0(i)di + P(1)\int_{-\infty}^{i_T} p_1(i)di\right] = 0 \quad . \tag{6.29}$$

Use of the Leibnitz Rule leads to

$$-P(0)p_0(i_T) + P(1)p_1(i_T) = 0 \quad . \tag{6.30}$$

Substitution of (6.16) and (6.17) for the *a priori* densities yields

$$\frac{\sigma_i P(0)}{\sigma_{elec} P(1)} = \exp\left\{-\frac{1}{2}\left[\frac{(i_T - i_S)^2}{\sigma_i^2} - \frac{i_T^2}{\sigma_{elec}^2}\right]\right\} \quad . \tag{6.31}$$

Taking the natural logarithm of both sides results in

$$\ln\left\{\frac{\sigma_i P(0)}{\sigma_{elec} P(1)}\right\} = -\frac{1}{2}\left[\frac{(i_T - i_S)^2}{\sigma_i^2} - \frac{i_T^2}{\sigma_{elec}^2}\right] \quad . \tag{6.32}$$

Rearranging terms gives a quadratic equation in i_T:

$$(\sigma_i^2 - \sigma_{elec}^2)i_T^2 + 2i_S\sigma_{elec}^2 i_T + \left[-2\sigma_{elec}^2\sigma_i^2 \ln\left\{\frac{\sigma_i P(0)}{\sigma_{elec} P(1)}\right\} - \sigma_{elec}^2 i_S^2\right] = 0 \quad . \tag{6.33}$$

At this point the solution is tested by assuming the special case where $P(0) = P(1) = 1/2$ and $\sigma_i = \sigma_{elec} = \sigma$. Making these substitutions yields

$$2i_S\sigma^2 i_T - \sigma^2 i_S^2 = 0 \quad , \tag{6.34}$$

which gives $i_T = i_S/2$, matching the previous result discussed in Section 6.3.1.

Using the quadratic formula and simplifying gives the following pair of solutions to (6.33):

$$i_T = \frac{-i_S\sigma_{elec}^2 \pm \sigma_{elec}\sigma_i\sqrt{2\ln\left\{\frac{\sigma_i P(0)}{\sigma_{elec}P(1)}\right\}(\sigma_i^2 - \sigma_{elec}^2) + i_S^2}}{\sigma_i^2 - \sigma_{elec}^2} \quad . \tag{6.35}$$

For the special case where $\sigma_{elec} = \sigma_i = \sigma$ the denominator of (6.35) becomes zero. The two solutions for the numerator are

$$-i_S\sigma^2 - i_S\sigma^2 = -2i_S\sigma^2 \tag{6.36}$$

and

$$-i_S\sigma^2 + i_S\sigma^2 = 0 \quad . \tag{6.37}$$

In the first case, $i_T \to \infty$ which is not reasonable and thus this solution is ignored. Therefore, the desired result for the optimal fixed threshold for the case of unequal variance is given by

$$i_T = \frac{-i_S\sigma_{elec}^2 + \sigma_{elec}\sigma_i\sqrt{2\ln\left\{\frac{\sigma_i P(0)}{\sigma_{elec}P(1)}\right\}(\sigma_i^2 - \sigma_{elec}^2) + i_S^2}}{\sigma_i^2 - \sigma_{elec}^2} \quad . \tag{6.38}$$

Equation (6.38) represents a key result as it defines the optimal fixed threshold accounting for signal dependent noise. Since the mean detector current is assumed constant during any given transmission of a 1, (6.38) also gives the adaptive threshold for a given value of captured optical power, s.

6.3.3 Unequal Variance with Scintillation. The most general case, accounting for signal dependent noise and scintillation, is now considered. As in Section 6.3.2, the two *a priori* densities illustrated by Figure 6.3 have different standard deviations. Furthermore, the PDF for signal-plus-noise has a mean value dependent on the optical power captured by the telescope, which varies due to atmospheric turbulence. The search for an optimum threshold which minimizes the probability of bit-error again starts with $dP_e/di_T = 0$. Starting with BER as defined by (6.19) gives

$$\frac{dP_e}{di_T} = P(0)\frac{d}{di_T}\left[\int_{i_T}^{\infty} p_0(i)di\right] + P(1)\frac{d}{di_T}\left[\int_0^{\infty}\int_{-\infty}^{i_T} p_1(i|s)p(s)didi s\right] = 0\ . \quad (6.39)$$

Using the Leibnitz Rule to differentiate the integral in the first term gives

$$-P(0)p_0(i_T) + P(1)\int_0^{\infty}\frac{d}{di_T}\left[\int_{-\infty}^{i_T} p_1(i|s)di\right]p(s)ds = 0 \quad . \quad (6.40)$$

Invoking the Leibnitz Rule a second time results in

$$-P(0)p_0(i_T) + P(1)\int_0^{\infty} p_1(i_T|s)p(s)ds = 0 \quad . \quad (6.41)$$

Substitution of (6.16) and (6.17) for $p_0(i_T)$ and $p_1(i_T|s)$, respectively, gives the following:

$$-\frac{P(0)}{\sigma_{elec}}\exp\left\{\frac{-i_T^2}{2\sigma_{elec}^2}\right\} + P(1)\int_0^{\infty}\frac{p(s)}{\sigma_i(s)}\exp\left\{\frac{-[i_T - i_S(s)]^2}{2\sigma_i^2(s)}\right\}ds = 0 \quad . \quad (6.42)$$

Assuming that $P(0) = P(1) = 1/2$ gives

$$\int_0^{\infty}\frac{p(s)}{\sigma_i(s)}\exp\left\{\frac{-[i_T - i_S(s)]^2}{2\sigma_i^2(s)}\right\}ds - \frac{1}{\sigma_{elec}}\exp\left\{\frac{-i_T^2}{2\sigma_{elec}^2}\right\} = 0 \quad . \quad (6.43)$$

Unfortunately, (6.43) does not provide an explicit solution for the optimal fixed threshold. However, a single integral remains which can be solved numerically.

Table 6.1: Parameter values for analysis of the optimal fixed and adaptive threshold optical binary receivers.

Parameter	Fixed Value	Case 1	Case 2
η (electrons/photon)	0.80		
ν (Hz)	2.0×10^{14}		
Bit Rate/Bandwidth (bps/Hz)		10×10^{6}	10×10^{9}
T (kelvin)	300		
R (ohms)	1000		
Loss Factor (dB)	-57		

6.4 System Evaluation Parameters

This section addresses several necessary considerations prior to calculating threshold values and BER results. First, Section 6.4.1 presents assumed values for required system parameters. Second, to obtain numeric results using the equations formulated in Sections 6.2 and 6.3, an analytic representation of the PDF describing turbulence-induced power fluctuations is required. Section 6.4.2 describes using the gamma-gamma PDF for this purpose. Last, Section 6.4.3 provides signal and noise current values corresponding to the extremes of captured optical power for the wave-optics simulation data described in Chapter IV.

6.4.1 System Parameter Values. System parameter values used to calculate numeric BER results for the optimal fixed and adaptive threshold techniques are presented in Table 6.1. Two bit rates are initially considered: 10 Mbps and 10 Gbps. Recall that for a random binary waveform, the bandwidth for baseband transmission is equal to the bit rate [90]. Therefore, with all other parameter values fixed, changing the bit rate from 10 Mbps to 10 Gbps increases the variance of both Johnson and shot noise by three orders of magnitude. The -57 dB loss factor previously discussed is applied to the wave-optics simulation data described in Chapter IV [4].

6.4.2 Using the Gamma-Gamma PDF. To calculate optimal fixed threshold and BER values, an analytic description of $p(s)$ is required. The gamma-gamma PDF

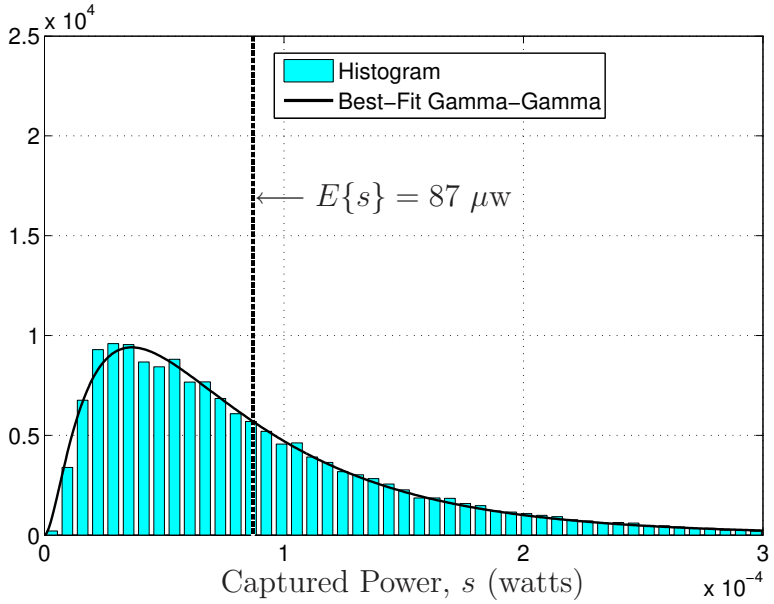

Figure 6.4: Histogram of captured power and best-fit gamma-gamma PDF for a turbulence strength of $C_n^2 = 3 \times 10^{-17}$ m$^{-2/3}$. The resulting parameter values for the gamma-gamma are $\alpha = \beta = 3.51$.

(see Section 2.4.6) has been the subject of much recent work in this area and is used for this purpose. Histograms of captured power were generated using the wave-optics data set described in Chapter IV. Best-fit gamma-gamma parameters were then found for each turbulence strength and define $p(s)$ for subsequent calculations. Resulting histograms and best-fit gamma-gamma curves are presented in Figures 6.4 and 6.5 for C_n^2 values of 3×10^{-17} and 8×10^{-17} m$^{-2/3}$, respectively. A best-fit was accomplished by using the *fminsearch* function in `Matlab`® to minimize sum square error between the normalized histogram and the gamma-gamma PDF evaluated at bin centers. Resulting parameter values are listed in Table 6.2. Bin edge locations were adjusted for each value of C_n^2 to just span the range of recorded values of captured power. Thus, histogram resolution was maximized for a fixed number of bins; 100 bins were used in all cases. Note that a best-fit yields identical values for α and β. Just as for the log-normal PDF [41:399-402], when the mean value of the gamma-gamma PDF is fixed, the other two parameters cannot be chosen independently.

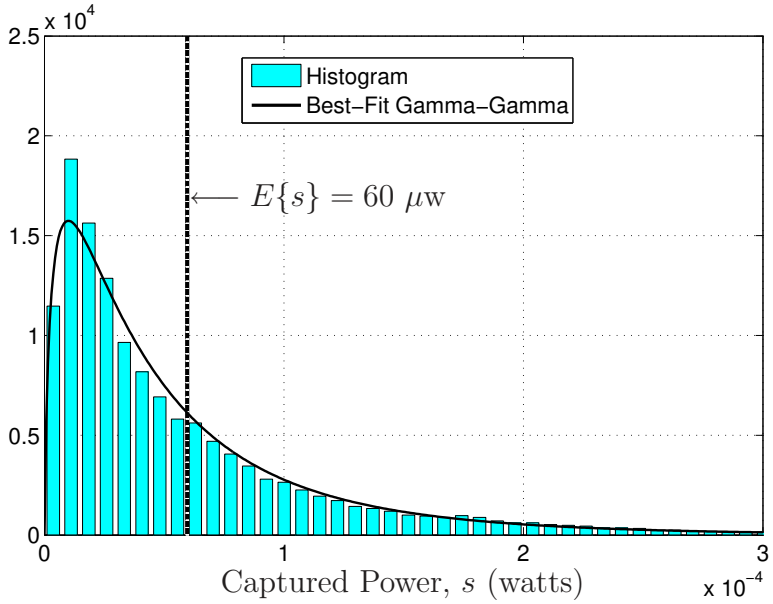

Figure 6.5: Histogram of captured optical power and best-fit gamma-gamma PDF for a turbulence strength of $C_n^2 = 8 \times 10^{-17}$ m$^{-2/3}$. The resulting parameter values for the gamma-gamma are $\alpha = \beta = 2.07$.

Table 6.2: Best-fit parameter values for the gamma-gamma PDF. Results for mean captured power reflect the -57 dB loss factor listed in Table 6.1. A best-fit was accomplished by using the *fminsearch* function in `Matlab`® to minimize the sum square error between the normalized histogram and the gamma-gamma PDF evaluated at bin centers. 100 bins were used for histogram generation.

	Mean Captured	Best-Fit
C_n^2 (m$^{-2/3}$)	Power (μw)	$\alpha = \beta$
1×10^{-17}	104	9.91
2×10^{-17}	95	5.04
3×10^{-17}	87	3.51
4×10^{-17}	80	2.85
5×10^{-17}	74	2.53
6×10^{-17}	69	2.32
7×10^{-17}	64	2.18
8×10^{-17}	60	2.07
9×10^{-17}	56	2.01
1×10^{-16}	52	1.97

Table 6.3: Signal and noise current values corresponding to minimum and maximum captured power from the wave-optics simulation data described in Chapter IV.

	Minimum	Maximum
Captured Power, s	663×10^{-9} w	763×10^{-6} w
Signal Current, i_S	642×10^{-9} A	739×10^{-6} A
Photons per Bit (at 10 Mbps)	5.0×10^{5}	5.8×10^{8}
Photons per Bit (at 10 Gbps)	500	5.8×10^{5}
Noise Currents at 10 Mbps		
Johnson Noise Current, i_{elec}	13×10^{-9} A	
Shot Noise Current, i_{shot}	1×10^{-9} A	49×10^{-9} A
Total Noise Current, i_N	13×10^{-9} A	50×10^{-9} A
Noise Currents at 10 Gbps		
Johnson Noise Current, i_{elec}	407×10^{-9} A	
Shot Noise Current, i_{shot}	45×10^{-9} A	2×10^{-6} A
Total Noise Current, i_N	410×10^{-9} A	2×10^{-6} A

6.4.3 Noise Current Regimes. Signal and noise current values are presented in Table 6.3 for the two bit rates considered and for corresponding minimum and maximum values of captured power (from wave-optics simulation data). Several important observations are made from the data presented in Table 6.3. First, the total noise current is shot noise limited for the maximum value of captured power, and Johnson noise limited for the minimum value of captured power. This is true for both bit rates considered. Second, the signal current generated by the minimum recorded value of captured power is approximately 50 and 1.5 times larger than Johnson noise current for the 10 Mbps and 10 Gbps cases, respectively. This observation is important for upcoming discussions of both analytic and simulated BER results.

6.5 Analytic Results

6.5.1 Optimal Fixed Threshold Calculations. The first step to determine performance of optimal fixed thresholds is calculating the threshold value itself, which depends on turbulence strength. To present an initial comparison between the fixed and adaptive decision threshold techniques, perfect knowledge of C_n^2 is assumed for

Table 6.4: Optimal fixed threshold values i_T for 10 Mbps and 10 Gbps communication links. Threshold values are presented both in terms of actual detector current, and as a multiple of the corresponding electronic (a.k.a., Johnson) noise current.

	i_T (10 Mbps)		i_T (10 Gbps)	
C_n^2 ($m^{-2/3}$)	nA	σ_{elec}	μA	σ_{elec}
1×10^{-17}	125	9.7	2.54	6.2
2×10^{-17}	91	7.1	1.91	4.7
3×10^{-17}	77	6.0	1.63	4.0
4×10^{-17}	70	5.4	1.49	3.7
5×10^{-17}	65	5.1	1.40	3.4
6×10^{-17}	63	4.9	1.35	3.3
7×10^{-17}	61	4.7	1.29	3.2
8×10^{-17}	59	4.6	1.26	3.1
9×10^{-17}	58	4.5	1.23	3.0
1×10^{-16}	57	4.4	1.21	3.0

fixed threshold cases. Thus, an optimal fixed threshold was calculated for each C_n^2 value prior to BER calculations. The best-fit gamma-gamma parameters listed in Table 6.2 were used to determine the form of $p(s)$, which then defined the threshold, i_T. Note that imperfect knowledge of turbulence, as existing in real-world scenarios, will degrade performance. Resulting optimal fixed threshold values i_T are presented in Table 6.4 for bit rates of 10 Mbps and 10 Gbps. Note that the optimal threshold monotonically decreases with increasing turbulence strength. However, the rate of decrease drops off significantly as C_n^2 exceeds 2×10^{-17} $m^{-2/3}$.

6.5.2 Adaptive Threshold Calculation. The adaptive threshold is chosen based on knowledge of i_S. Since the mean detector current is assumed constant during any given transmission of a 1, adaptive threshold selection reduces to a simpler problem of choosing the optimal fixed threshold corresponding to the assumed mean detector current. Thus, (6.38) is used to calculate the adaptive threshold as a function of mean signal current, i_S, which is a function of captured optical power, s.

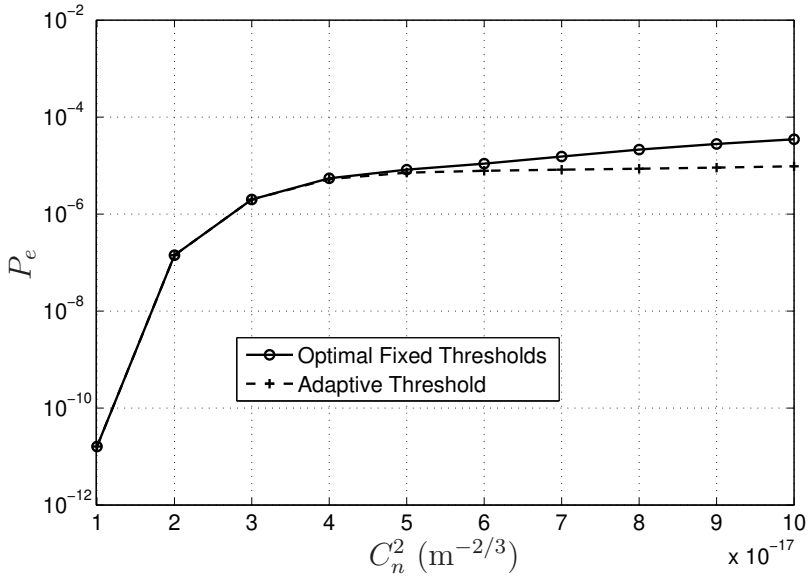

Figure 6.6: Analytic BER results versus turbulence strength for a 10 Mbps communication link. The optimal fixed threshold curve assumes knowledge of C_n^2, while the adaptive curve does not.

6.5.3 Analytic BER Results. Analytic BER results for the optimal fixed and adaptive threshold techniques are presented in Figures 6.6 and 6.7 for bit rates of 10 Mbps and 10 Gbps, respectively. As expected, an adaptive threshold either outperforms or provides nearly identical performance as compared to the case of optimal fixed thresholds. However, for the 10 Mbps case the benefit of adaptive thresholding grows as turbulence intensifies, whereas the benefit decreases slightly for 10 Gbps. To quantify the relative improvement provided by an adaptive threshold, the (order of magnitude) BER improvement factor is defined as

$$\text{BER Improvement Factor} = \log_{10}\left\{\frac{P_{e,fixed}}{P_{e,adapt}}\right\} \quad \text{(orders of magnitude)}\,. \tag{6.44}$$

The improvement factor is plotted in Figure 6.8 for the two bit rates considered using the adaptive threshold. Note that for a 10 Mbps link, the adaptive threshold does not show noticeable improvement until C_n^2 exceeds 4×10^{-17} m$^{-2/3}$. However, for a 10 Gbps link the adaptive threshold provides significant improvement for all turbulence strengths considered. In contrast to the 10 Mbps result, the 10 Gbps

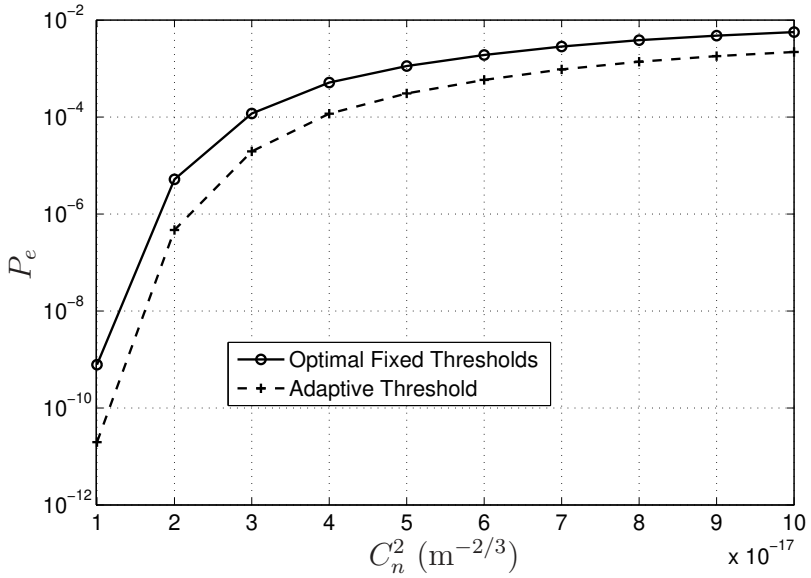

Figure 6.7: Analytic BER results versus turbulence strength for a 10 Gbps communication link. The optimal fixed threshold curve assumes knowledge of C_n^2, while the adaptive curve does not.

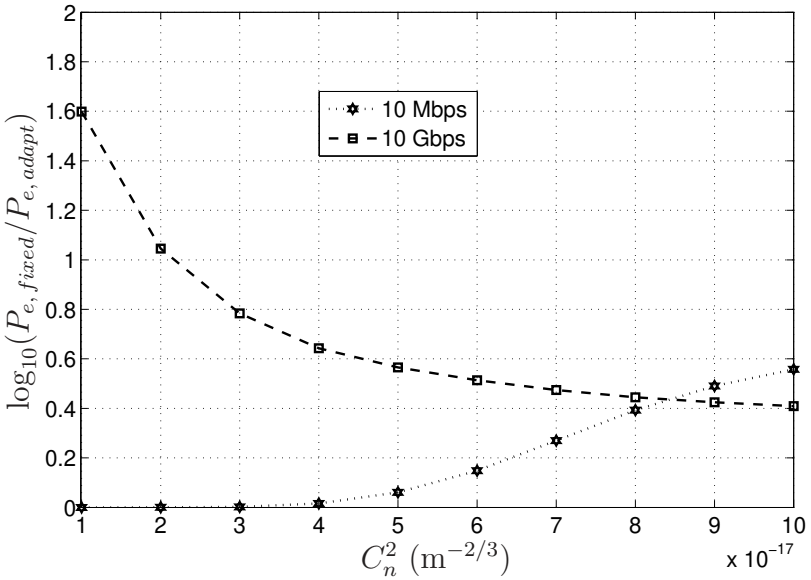

Figure 6.8: BER improvement factor of (6.44) versus turbulence strength for bit rates of 10 Mbps and 10 Gbps using an adaptive threshold.

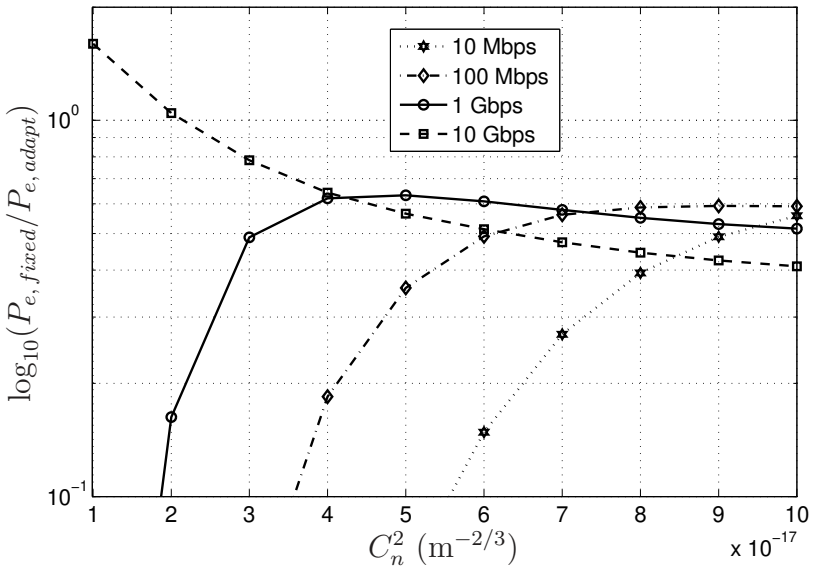

Figure 6.9: BER improvement factor of (6.44) versus turbulence strength for bit rates of 10 Mbps, 100 Mbps, 1 Gbps, and 10 Gbps using an adaptive threshold.

improvement factor actually increases with decreasing turbulence strength - ranging from 0.41 at $C_n^2 = 1 \times 10^{-16}$ m$^{-2/3}$ to 1.60 at $C_n^2 = 1 \times 10^{-17}$ m$^{-2/3}$.

To further understand the relationship between bit rate (i.e., noise bandwidth) and the BER improvement factor, two additional bit rates were considered: 100 Mbps and 1 Gbps. The improvement factors for all four bit rates are presented in Figure 6.9, and are now displayed in log space along the y-axis to highlight results in the region of weaker turbulence. The BER improvement factor is a convenient metric in the sense that it corresponds directly to differences between the fixed and adaptive threshold BER results in Figures 6.6 and 6.7. However, this metric is also somewhat deceptive in that an improvement factor of 0.1 may seem trivial, which is not the case. BER improvement factors of 0.1, 1.0, and 1.6 correspond to situations where the optimal fixed threshold has 1.3, 10, and 33 times more bit-errors than the adaptive threshold case. Furthermore, if 0.1 orders of magnitude is the minimum acceptable BER improvement per (6.44), then Figure 6.9 implies the existence of a lower bound, in terms of turbulence strength, on the region of improvement for each bit rate. This lower bound is approximately $C_n^2 = [5.6, 3.6, 1.9] \times 10^{-17}$ m$^{-2/3}$ for bit rates of 10 Mbps,

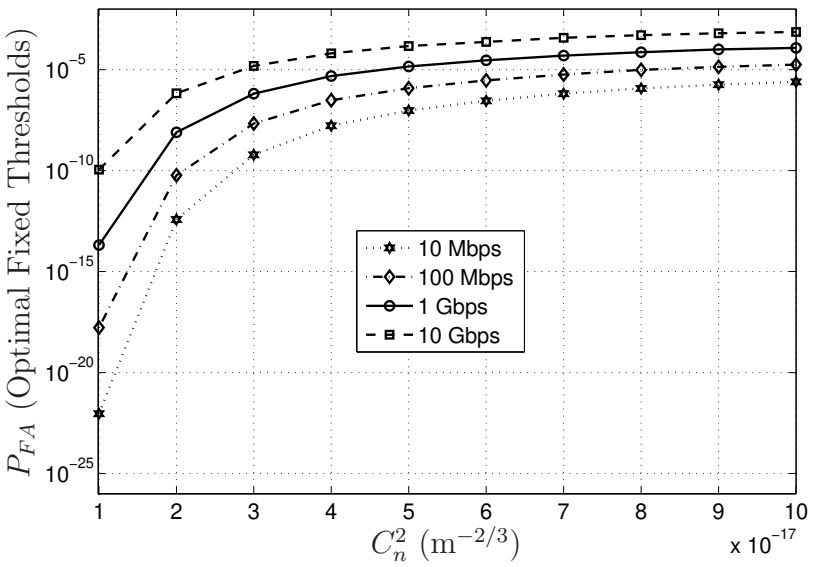

Figure 6.10: Probability of false alarm (P_{FA}) versus turbulence strength for *optimal fixed thresholds* and bits rates of 10 Mbps, 100 Mbps, 1 Gbps, and 10 Gbps.

100 Mbps, and 1 Gbps, respectively. The value of the lower bound in the 10 Gbps case is less than the weakest turbulence strength considered, 1×10^{-17} m$^{-2/3}$. Given that a major motivation behind LaserCom is high-bandwidth communication, and that BER degrades with increasing C_n^2, the adaptive threshold is an attractive approach for improving LaserCom performance in challenging, long-range scenarios.

To further understand performance gains afforded by adaptive thresholding, the probabilities of missed detection (P_{MD}) and false alarm (P_{FA}) are plotted separately in Figures 6.10 through 6.13 for bit rates of $[1, 10, 100, 1000] \times 10$ Mbps. Figures 6.10 and 6.11 provide insight into BER performance for the case of optimal fixed thresholds. Figure 6.10 shows P_{FA} versus C_n^2, with P_{FA} increasing monotonically both with increasing bit rate and turbulence strength. Figure 6.11 shows P_{MD} versus C_n^2, with P_{MD} appearing to approach a lower limit (as a function of bit rate) for the three weakest turbulence strengths considered. Furthermore, for any pair of bit rate/turbulence strength values considered, P_{MD} is larger than P_{FA}, and therefore the limiting contributor to total bit-error probability.

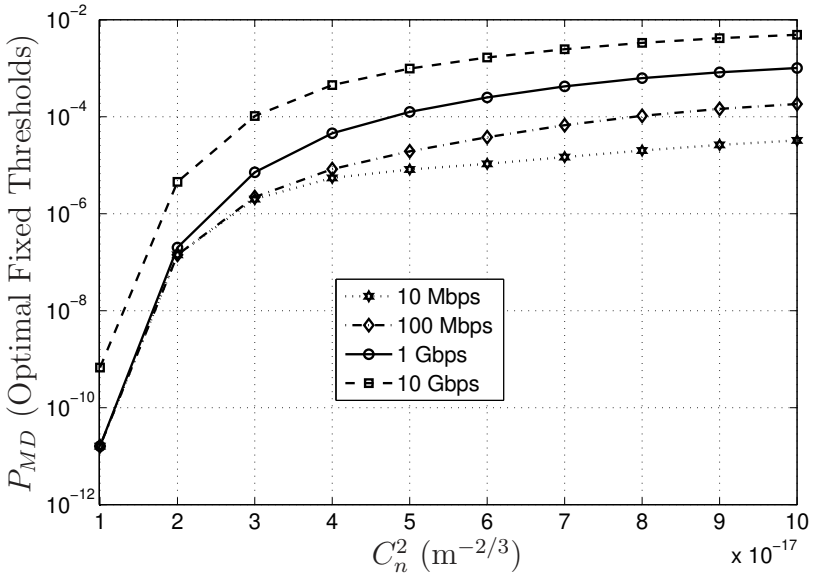

Figure 6.11: Probability of missed detection (P_{MD}) versus turbulence strength for *optimal fixed thresholds* and bits rates of 10 Mbps, 100 Mbps, 1 Gbps, and 10 Gbps.

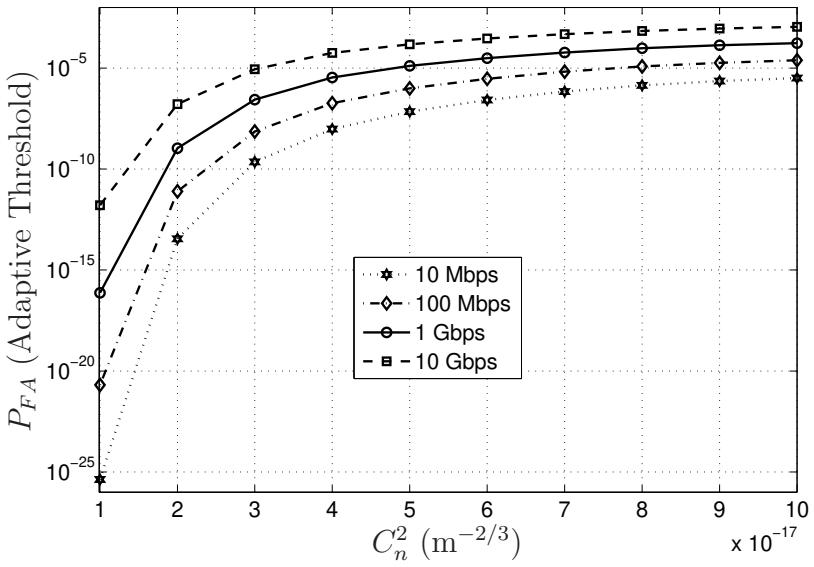

Figure 6.12: Probability of false alarm (P_{FA}) versus turbulence strength for an *adaptive threshold* and bits rates of 10 Mbps, 100 Mbps, 1 Gbps, and 10 Gbps.

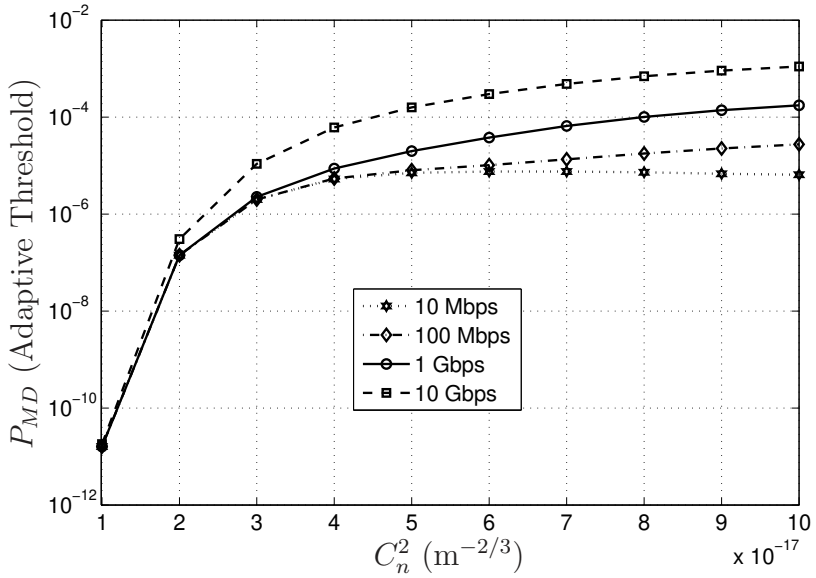

Figure 6.13: Probability of missed detection (P_{MD}) versus turbulence strength for an *adaptive threshold* and bits rates of 10 Mbps, 100 Mbps, 1 Gbps, and 10 Gbps.

Figures 6.12 and 6.13 provide insight into BER performance for the adaptive threshold. Figure 6.12 shows P_{FA} versus C_n^2. Once again, P_{FA} increases monotonically both with increasing bit rate and turbulence strength. Furthermore, relative to Figure 6.10 results the adaptive threshold has significantly decreased P_{FA} for the weakest turbulence strength considered, 1×10^{-17} m$^{-2/3}$. Although not obvious from comparing the results of Figures 6.10 and 6.12, closer inspection of the data reveals that the adaptive threshold actually increased P_{FA} slightly for several of the stronger turbulence strengths considered. Figure 6.13 shows P_{MD} versus C_n^2. This result shows a similar trend to that for optimal fixed thresholds. However, relative to Figure 6.11 results the adaptive threshold has pushed the P_{MD} curves downward - approaching what appears to be a lower limit (as a function of bit rate) for weaker turbulence strengths considered. Although not obvious from comparing the results of Figures 6.11 and 6.13, closer inspection of the data reveals that for $C_n^2 \geq 2 \times 10^{-17}$ m$^{-2/3}$ the P_{MD} results for adaptive thresholding are smaller than for optimal fixed thresholds. This is the region of turbulence strength which corresponds to moderate to strong amplitude fluctuations. For the weakest turbulence considered, $C_n^2 = 1 \times 10^{-17}$ m$^{-2/3}$, P_{MD}

values for the adaptive and optimal fixed threshold cases are nearly equal. As in the case of optimal fixed thresholds, for any pair of bit rate/turbulence strength values considered, P_{MD} is larger than P_{FA}, and therefore the limiting contributor to total bit-error probability.

The breakout of performance by P_{FA} and P_{MD} gives interesting insight into adaptive threshold performance. The adaptive threshold actually gives up some performance in terms of P_{FA} at stronger turbulence strengths, but in this same region provides the most improvement in P_{MD}. Furthermore, for both adaptive and optimal fixed thresholds, P_{FA} is smaller than P_{MD} for any pair of bit rate/C_n^2 values considered. Thus, the tradeoff of P_{FA} and P_{MD} resulted in an overall improvement in P_e.

6.6 Simulation Results

6.6.1 Adaptive Threshold Estimation Error. In practice, perfect knowledge of i_S is unavailable. However, i_S can be estimated based on prior measurements of detector current since bit rates are much greater than the rate of atmospheric change. The effectiveness of an adaptive threshold implementation will depend on accuracy of the estimate of i_S, upon which the threshold i_T is based. The normalized variance of the adaptive threshold estimate is described by

$$\sigma^2_{\hat{i_T}}(N) = E\left\{\frac{[i_T - \hat{i_T}(N)]^2}{i_T^2}\right\} \quad , \tag{6.45}$$

where N is the number of prior samples used to generate the estimate, $\hat{i_T}$. Results in terms of standard deviation are presented in Figure 6.14 for the 10 Mbps case. The calculations were also made for the 10 Gbps case, but results were nearly indistinguishable from those presented in Figure 6.14. Initially, the estimation error decreases with an increasing number of prior samples. This is attributed to an increased ability to average out the noise. However, when N goes from 500 to 750 the estimation error actually increases for $C_n^2 > 2 \times 10^{-17}$ m$^{-2/3}$. This is attributed to increased

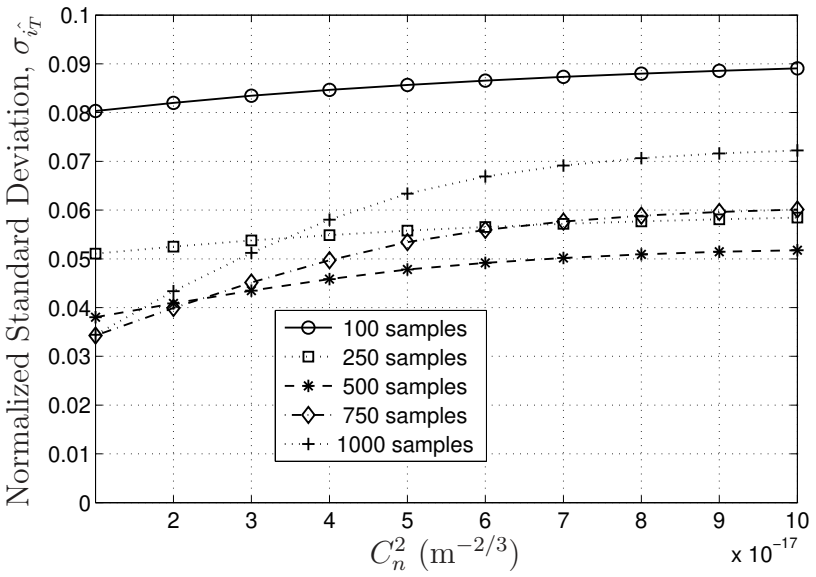

Figure 6.14: Adaptive threshold estimation error (standard deviation) versus turbulence strength for a 10 Mbps link, and a varying number of prior samples used to estimate the threshold i_T.

scintillation-induced power fluctuations captured by a great number of samples. For the given bit rate, 1000 samples corresponds to 1 msec, which is on the order of the expected rate of atmospheric change. Overall, based on the results presented here, a value of $N = 500$ is the best choice for adaptive threshold estimation in the scenarios studied. At this value, the estimated i_T will have a normalized standard deviation of about 5% of the true value.

6.6.2 Adaptive Threshold BER Results. To provide additional validation of the analytic results and flexibility for future studies, a simulation approach was also pursued. The fixed and adaptive threshold techniques were implemented in `Matlab`®. Next, the wave-optics data from Chapter IV was processed using both techniques. However, this approach yielded BER results below (better than) those predicted by analysis. The discrepancy was suspected to result from using too few data points to properly estimate the very small probabilities of interest. The wave-optics simulation produced 153,510 data points per C_n^2 value. However, this data is temporally correlated. To validate the assertion of too few samples, a second approach

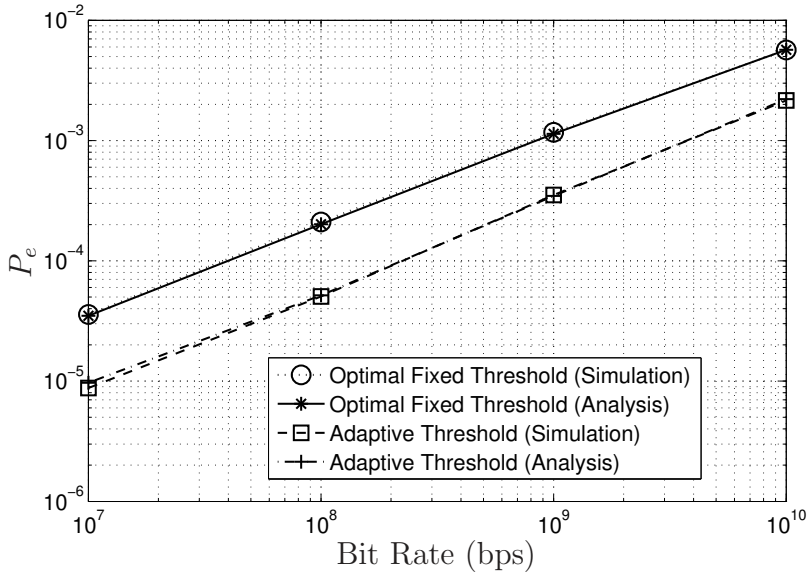

Figure 6.15: Analytic and simulated BER results versus bit rate for a turbulence strength of $C_n^2 = 1 \times 10^{-16}$ m$^{-2/3}$. Four million independent realizations of captured power were used to calculate each simulation result.

was undertaken. Using the best-fit gamma-gamma curves described in Section 6.4.2, 4×10^6 independent random realizations of captured optical power were generated for the strongest turbulence studied ($C_n^2 = 1 \times 10^{-16}$ m$^{-2/3}$). This new set of data was then processed using both the optimal fixed and adaptive threshold techniques. Results are presented in Figure 6.15 for the four bit rates considered, and show excellent agreement between the simulation and analytic approaches. Furthermore, this result highlights the challenge of estimating the small BER values of interest. Considering the computation time required to generate the wave-optics data set for Chapter IV, an analytic approach is required for the adaptive threshold investigation presented in this chapter assuming limited computation resources.

6.6.3 Impact of Threshold Estimation Error on BER. The previous two sections investigated adaptive threshold estimation error and validated analytic BER results in simulation. This section extends those two results to produce a higher fidelity model of adaptive threshold performance. BER is plotted versus turbulence strength in Figure 6.16 for a bit rate of 10 Gbps, and for three calculation methods.

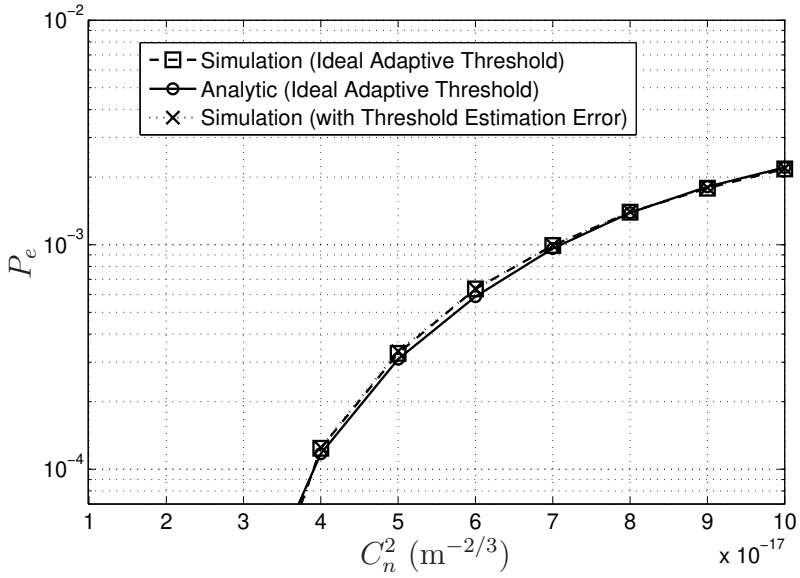

Figure 6.16: BER versus turbulence strength for an adaptive threshold and a bit rate of 10 Gbps. A threshold estimation error of $\sigma_{\hat{i_T}} = 0.05$ was used to calculate the third curve. One million independent realizations of captured power were used to calculate each simulation result.

First, the analytic result is presented assuming an ideal adaptive threshold. Second, the simulation result for the ideal adaptive threshold is presented. The third curve corresponds to a simulated adaptive threshold, including the effect of threshold estimation error. The estimation error was modelled as Gaussian, with a standard deviation of $0.05 \times i_T$ based on the results of Figure 6.14 for $N = 500$. One million independent values of captured power were used to calculate each simulation result. Figure 6.16 demonstrates that the impact of threshold estimation error on BER is negligible for the given parameters and scenario studied.

6.7 Closing Remarks

This chapter developed an adaptive binary decision threshold to mitigate the impact of scintillation and detector noise on BER. This included comparisons with optimal fixed thresholds. Expressions for BER were derived for both the fixed and adaptive threshold cases. Analytic results show an adaptive threshold provides a BER improvement of 0.41 to 1.60 orders of magnitude (2.6 to 33-fold decrease) for a 10 Gbps

link, and up to 0.56 orders of magnitude (3.6-fold decrease) for a 10 Mbps link. This approach yields significant improvement in BER without the additional cost, weight, and/or complexity of increasing source power, incorporating wavefront control at receiver, or incorporating AO at the transmitter. Furthermore, adaptive threshold performance was compared to fixed threshold performance, where an optimal fixed threshold was chosen for each turbulence strength to minimize BER. This implies that knowledge of C_n^2 would be required to achieve fixed threshold results presented in this chapter. However, results for the adaptive threshold technique do not assume knowledge of C_n^2.

To highlight the impact of an adaptive threshold, several system design scenarios are considered. First, a bit rate requirement of 10 Mbps and a channel BER requirement of 10^{-5} are assumed. As seen in Figure 6.6, an adaptive threshold meets these requirements for all turbulence strengths considered. However, the optimal fixed threshold meets the required BER only for $C_n^2 \leq 5.7 \times 10^{-17}$ m$^{-2/3}$. In other words, the adaptive threshold meets requirements in turbulence which is 75% stronger. Second, a bit rate requirement of 10 Gbps and a channel BER requirement of 10^{-4} are assumed. As seen in Figure 6.7, an adaptive threshold provides the same BER performance as an optimal fixed threshold, but in turbulence that is 33% stronger. Adaptive threshold performance can also be described in terms of providing the same BER performance for a longer communication range or smaller aperture. However, these relationships are not straightforward. Longer propagation paths will change the shape of $p(s)$, and further calculations would be required to explore the space of BER as a function of path length and aperture size.

6.8 Future Work

There are several promising areas for extending the research. First, fidelity could be increased by accounting for fixed threshold estimation error in BER calculations. For the optimal fixed threshold case, threshold estimation error would be driven by C_n^2 estimation error. Since r_0 is often used to characterize turbulence strength, and

is related to C_n^2 in a simple fashion for uniform turbulence, r_0 could be allowed to vary by up to 200% from the true value. Second, the impact of peak tracking and other wavefront control schemes on the gamma-gamma parameters could be explored. This result could then be used to analytically investigate system performance using both wavefront control and an adaptive threshold. A simulation approach could also be utilized. The third area for extending the research is to explore a combination of adaptive thresholding with other scintillation/fade compensation techniques, such as forward error-correction codes, data interleaving, multiple beams, etc. Last, the entire analysis could be repeated for a UAV-to-GEO engagement, where an optical communication link provides an additional means to disseminate surveillance imagery in near real-time to any point on Earth.

VII. Conclusion

The goal of this research was to extend the standard approach to atmospheric turbulence compensation system design from one that strives to minimize MSE to one that strives to optimize the metric of interest. A MSE performance metric is typical of both image restoration algorithms and AO systems. For post-processing techniques, the common metric is the MSE between the ideal and recovered image intensities. For AO, the aperture averaged mean square phase abberation is often used for system analysis and design. For a closed-loop system, assuming negligible amplitude fluctuations, mean square phase is directly related to average Strehl ratio [47,89]. As a result, characterization of turbulence effects and optimization of AO performance is typically accomplished in terms of mean square phase [44,64,101,103]. For LaserCom performance, the probability of fade and associated area under the tail of the signal's PDF are more important than the average signal power. Furthermore, UAVs of various sizes are playing an ever increasing role for surveillance, reconnaissance, and weapon delivery. The divergence of design approaches based on minimizing MSE versus preventing and mitigating the impact of deep signal fades was the motivation for this research. The additional weight, size, power, and other constraints imposed on small airborne platforms were also considered in the sense that simplicity is desired.

Chapter IV presented investigative results for alternate tracking schemes for LaserCom fade mitigation. A 100 km air-to-air scenario was studied using analysis and wave-optics simulation. Focal plane image spot breakup was identified as the dominant failure mechanism. Significant breakup first occurs when $D/r_0 \approx 0.6$ and $\sigma_\chi^2 = 0.19$. The impact of spot breakup was minimal for average Strehl, but considerable for fade probability - demonstrating that optimization of a wavefront control system must consider the performance metric of interest. Fade probability is directly related to BER for direct-detection communication systems. Alternate tracking schemes were then investigated based on knowledge of spot breakup. Metric-driven design led to exploration of peak intensity tracking, which reduces fade probability by

greater than 50% over conventional centroid trackers and AO systems for scenarios studied. This result demonstrates that metric-driven control of two wavefront phase modes outperforms MSE driven control of over 23 modes for the metric of interest. Thus, improved performance is achieved with a much simpler system. This result is important for potential UAV based optical receivers using a fiber-coupled detector. The duration of focal plane spot breakup was then characterized. From a system design standpoint, this result is important for both sensor frame-rate and system bandwidth requirements, as well as optimizing error-correction codes.

Chapter V defined an architecture to further examine regions of operation for various atmospheric compensation techniques. Fades are classified based on complexity of the required compensation technique. For compensation techniques studied, regions of superior performance, in terms of minimal fade probability as a function of detection threshold, were identified. Peak tracking outperforms AO for thresholds below approximately 4% of the unabberated intensity. Furthermore, the boundary between dominance regions is nearly invariant to turbulence strength. Boundary invariance would simplify operation of a composite system which is capable of adaptively selecting compensation methodology in real-time.

Chapter VI presented an adaptive binary decision threshold for mitigating scintillation induced bit-errors. Results show this technique to be viable for decreasing BER in the presence of scintillation and receiver noise. Expressions for BER were derived for both the fixed and adaptive threshold cases. Analytic results show an adaptive threshold provides a BER improvement of 0.41 to 1.60 orders of magnitude (2.6 to 33-fold decrease) for a 10 Gbps link, and up to 0.56 orders of magnitude (3.6-fold decrease) for a 10 Mbps link. This approach yields significant improvement in BER without the additional cost, weight, and/or complexity of increasing source power, incorporating wavefront control at receiver, or incorporating AO at the transmitter.

Bibliography

1. "Alexander Graham Bell as Inventor and Scientist". Article on the United States Library of Congress Website. 14 Jan 2004 http://memory.loc.gov/ammem/bellhtml/bellinvent.html.

2. Akihiko, Watanabe and Kawasumi Ikuo. "Study on wideband CDMA system in burst error environment". *IEEE International Conference on Personal Wireless Communications*, 324–328. 1997.

3. Al-Habash, M.A., Larry C. Andrews, and Ronald L. Phillips. "Mathematical Model for the Irradiance PDF of a Laser Beam Propagating through Turbulent Media". *Opt. Eng.*, 40(8):1554–1562, August 2001.

4. Alexander, Stephen B. *Optical Communication Receiver Design*. SPIE Tutorial Texts in Optical Engineering, vol. TT22; IEE Telecommunications Series, vol. 37. SPIE Press, Bellingham, WA, 1997.

5. Andrews, Larry C. and Ronald L. Phillips. *Laser Beam Propagation through Random Media*. SPIE Press, Bellingham, WA, 1998.

6. Andrews, Larry C. and Ronald L. Phillips. *Mathematical Techniques for Engineers and Scientists*. SPIE Press, Bellingham, WA, 2003.

7. Andrews, Larry C., Ronald L. Phillips, and Cynthia Y. Hopen. "Scintillation Model for a Satellite Communication Link at Large Zenith Angles". *Opt. Eng.*, 39:3272–3280, 2000.

8. Andrews, Larry C., Ronald L. Phillips, and Cynthia Y. Hopen. *Laser Beam Scintillation with Applications*. SPIE Press, Bellingham, WA, 2001.

9. Andrews, Larry C., Ronald L. Phillips, Cynthia Y. Hopen, and M.A. Al-Habash. "Theory of Optical Scintillation". *J. Opt. Soc. Am. A*, 16(6):1417–1429, June 1999.

10. Babcock, Horace W. "The possibility of compensating astronomical seeing". *Publ. Astron. Soc. Pac.*, 65:229, 1953.

11. Barchers, Jeffrey D. "Evaluation of the Impact of Finite-Resolution Effects on Scintillation Compensation Using Two Deformable Mirrors". *J. Opt. Soc. Am. A*, 18(12):3098–3109, December 2001.

12. Barchers, Jeffrey D. "Application of the Parallel Generalized Projection Algorithm to the Control of Two Finite-Resolution Deformable Mirrors for Scintillation Compensation". *J. Opt. Soc. Am. A*, 19(1):54–63, January 2002.

13. Barchers, Jeffrey D. "Closed-Loop Stable Control of Two Deformable Mirrors for Compensation of Amplitude and Phase Fluctuations". *J. Opt. Soc. Am. A*, 19(5):926–945, May 2002.

14. Barchers, Jeffrey D. "Convergence Rates for Iterative Vector Space Projection Methods for Control of Two Deformable Mirrors for Compensation of Both Amplitude and Phase Fluctuations". *Applied Optics*, 41(12):2213–2218, 20 April 2002.

15. Barchers, Jeffrey D. and Brent L. Ellerbroek. "Improved Compensation of Turbulence-Induced Amplitude and Phase Distortions by Means of Multiple Near-Field Phase Adjustments". *J. Opt. Soc. Am. A*, 18(2):399–411, February 2001.

16. Barchers, Jeffrey D., David L. Fried, and Donald J. Link. "Evaluation of the Performance of a Shearing Interferometer in Strong Scintillation in the Absence of Additive Measurement Noise". *Applied Optics*, 41(18):3674–3684, 20 Jun 2002.

17. Barchers, Jeffrey D., David L. Fried, and Donald J. Link. "Evaluation of the Performance of Hartmann Sensors in Strong Scintillation". *Applied Optics*, 41(6):1012–1021, 20 Feb 2002.

18. Barchers, Jeffrey D., David L. Fried, Donald J. Link, Glenn A. Tyler, William Moretti, Terry J. Brennan, and Robert Q. Fugate. "The Performance of Wavefront Sensors in Strong Scintillation". Peter L. Wizinowich and Domenico Bonaccini (editors), *Proceedings of the SPIE - Adaptive Optical System Technologies II*, volume 4839, 217–227. SPIE Press, Bellingham, WA, Aug 2002.

19. Barchers, Jeffrey D. and Troy A. Rhoadarmer. "Evaluation of Phase-Shifting Approaches for a Point Diffracion Interferometer with the Mutual Coherence Function". *Applied Optics*, 41(36):7499–7509, 20 Dec 2002.

20. Beland, Robert R. *Propagation Through Amospheric Optical Turbulence*, volume 2 of *The Infrared & Electro-Optical Systems Handbook*, chapter 2, 156–232. SPIE Press, Bellingham, WA, 1993.

21. Bell, Alexander Graham. "Apparatus for Signaling and Communicating, called "Photophone"". United States Patent, 7 Dec 1880. U.S. Patent No. 235199.

22. Bell, Alexander Graham, Chichester A. Bell, and Sumner Tainter. "Transmitting and Recording Sounds by Radiant Energy". United States Patent, 4 May 1886. U.S. Patent No. 341213.

23. Bell, Alexander Graham and Sumner Tainter. "Photophone-Transmitter". United States Patent, 14 Dec 1880. U.S. Patent No. 235496.

24. Bell, Alexander Graham and Sumner Tainter. "Photophonic Receiver". United States Patent, 24 May 1881. U.S. Patent No. 241909.

25. Burris, Harris R., Christopher I. Moore, Michael J. Vilcheck, Rita Mahon, Mena F. Stell, Michele R. Suite, Mark A. Davis, William J. Scharpf, Anne E. Reed, William S. Rabinovich, G. C. Gilbreath, Eun Oh, and Nader M. Namazi.

"Low-frequency sampling adaptive thresholding for free-space optical communication receivers with multiplicative noise". David G. Voelz and Jennifer C. Ricklin (editors), *Proc. SPIE 5160, Free-Space Laser Communication and Active Laser Illumination III*, 355–368. SPIE Press, Bellingham, WA, 2004.

26. Burris, H.R., A.E. Reed, N.M. Namazi, W.J. Scharpf, M.J. Vicheck, M.F. Stell, and M.R. Suite. "Adaptive thresholding for free-space optical communication receivers with multiplicative noise". *IEEE Aerospace Conference Proceedings*, volume 3, 1473–1480. 2002.

27. Burris, H.R., A.E. Reed, N.M. Namazi, M.J. Vilcheck, and M. Ferraro. "Use of Kalman filtering in data detection in optical communication systems with multiplicative noise". *Proc. of the IEEE International Conference on Acoustics, Speech, and Signal Processing (ICASSP '01)*, volume 4, 2685–2688. 7-11 May 2001.

28. Carroll, Joseph, Daniel C. Gray, Austin Roorda, and David R. Williams. "Recent advances in retinal imaging with adaptive optics". *Optics & Photonics News*, 16(1):36–42, January 2005.

29. Churnside, J.H. and R.G. Frehlich. "Experimental Evaluation of Log-Normally Modulated Rician and IK Models of Optical Scintillation in the Atmosphere". *J. Opt. Soc. Am. A*, 6:1760–1766, 1989.

30. Coles, Wm. A., J.P. Filice, R.G. Frehlich, and M. Yadlowsky. "Simulation of Wave Propagation in Three-Dimensional Random Media". *Applied Optics*, 34(12):2089–2101, April 1995.

31. Crabtree, Peter N. "Critical (Wavefront) Mode Analysis for Improved Reliability of Lasercom Systems using Adaptive Optics (AO)". *7th Annual Directed Energy Symposium*. Rockville, MD, 18-21 Oct 2004.

32. Dereniak, E.L. and G.D. Boreman. *Infrared Detectors and Systems*. Wiley Series in Pure and Applied Optics. Wiley-Interscience, New York, NY, 1996.

33. Flatte, S.M., C. Bracher, and G.-Y. Wang. "Probability-Density Functions of Irradiance for Waves in Atmospheric Turbulence Calculated by Numerical Simulations". *J. Opt. Soc. Am. A*, 11:2080–2092, 1994.

34. Fried, David L. "Limiting Resolution Looking Down Through the Atmosphere". *J. Opt. Soc. Am.*, 56(10):1380–1384, 1966.

35. Fried, David L. "Optical Resolution Through a Randomly Inhomogeneous Medium". *J. Opt. Soc. Am.*, 56:1372–1379, 1966.

36. Fried, David L. "Anisoplanatism in Adaptive Optics". *J. Opt. Soc. Am.*, 72(1):52–61, January 1982.

37. Fried, David L. "Branch Point Problem in Adaptive Optics". *J. Opt. Soc. Am. A*, 15(10):2759–2768, October 1998.

38. Gagliardi, Robert M. and Sherman Karp. *Optical Communications*. Wiley Series in Telecommunications and Signal Processing. John Wiley and Sons, Inc., New York, NY, 2nd edition, 1995.

39. Gaughan, Richard. "Miniature deformable mirrors bring adaptive optics within reach". *Photonics Spectra*, 39(2):82–90, February 2005.

40. Ghiglia, Dennis C. and Mark D. Pritt. *Two-Dimensional Phase Unwrapping: Theory, Algorithms, and Software*. John Wiley and Sons, Inc., New York, NY, 1998.

41. Goodman, Joseph W. *Statistical Optics*. John Wiley & Sons, Inc., New York, NY, 1985.

42. Goodman, Joseph W. *Introduction to Fourier Optics*. McGraw-Hill Electrical and Computer Engineering Series. McGraw-Hill, New York, NY, 2nd edition, 1996.

43. Guizzo, Erico. "Closing in on the perfect code". *IEEE Spectrum*, 41(3):36–42, March 2004.

44. Hardy, John W. *Adaptive Optics for Astronomical Telescopes*. Oxford Series in Optical and Imaging Science. Oxford University Press, Oxford, 1998.

45. Harris R. Burris, Jr., Nader M. Namazi, Anne E. Reed, William J. Scharpf, Christopher I. Moore, Michael J. Vilcheck, Mark A. Davis, Mena F. Stell, Michele R. Suite, William S. Rabinovich, and R. Mahon. "Comparison of adaptive methods for optimal thresholding for free-space optical communication receivers with multiplicative noise". Jennifer C. Ricklin and David G. Voelz (editors), *Proc. SPIE 4821, Free-Space Laser Communication and Laser Imaging II*, 139–154. SPIE Press, Bellingham, WA, 2002.

46. Hecht, Eugene. *Optics*. Addison-Wesley, Reading, MA, 3rd edition, 1998.

47. Herrmann, Jan. "Phase variance and Strehl ratio in adaptive optics". *J. Opt. Soc. Am. A*, 9(12):2257–2258, December 1992.

48. Higgs, Charles, Herbert T. Barclay, and Kenneth W. Billman. "Multibeam laser illuminator approach". Todd D. Steiner and Paul H. Merritt (editors), *Airborne Laser Advanced Technology II*, volume 3706, 206–215. SPIE Press, Bellingham, WA, 1999.

49. Hill, R.J. and R.G. Frehlich. "Probability Distribution of Irradiance for the Onset of Strong Scintillation". *J. Opt. Soc. Am. A*, 14:1530–1540, 1997.

50. Hines, John. "Transformational Communications Air Layer". *Technology Horizons*, 6(3):12, Jun 2005.

51. Horwath, Joachim, Nicolas Perlot, Dirk Giggenbach, and Ralf Jüngling. "Numerical simulations of beam propagation through optical turbulence for high-altitude

platform crosslinks". G. Stephen Mecherle, Cynthia Y. Young, and John S. Stryjewski (editors), *Free-Space Laser Communication Technologies XVI*, volume 5338 of *Proc. SPIE*, 243–252. 2004.

52. H.R. Burris, Jr., C.I. Moore, L.A. Swingen, L.M. Wasiczko, R. Mahon, M.F. Stell, M.R. Suite, W.S. Rabinovich, J.L. Murphy, G.C. Gilbreath, and W.J. Scharpf. "Laboratory implementation of an adaptive thresholding system for free-space optical communication receivers with signal dependent noise". David G. Voelz and Jennifer C. Ricklin (editors), *Proc. SPIE 5892, Free-Space Laser Communications V*, 283–302. SPIE Press, Bellingham, WA, 2005.

53. Hudgin, Richard. "Wave-front Compensation Error Due to Finite Corrector-Element Size". *J. Opt. Soc. Am.*, 67(3):393–395, March 1977.

54. Killinger, Dennis. "Free Space Optics for Laser Communication Through the Air". *Optics and Photonics News*, 13(10):36–42, October 2002.

55. Lambert, Stephen G. and William L. Casey. *Laser Communications in Space*. Artech House, Inc., Boston, MA, 1995.

56. Lane, R.G., A. Glindemann, and J.C. Dainty. "Simulation of a Kolmogorov Phase Screen". *Waves in Random Media*, 209–224, 1992.

57. Levine, B. Martin, Elizabeth A. Martinsen, Allan Wirth, Andrew Jankevics, Manuel Toledo-Quinones, Frank Landers, and Theresa L. Bruno. "Horizontal line-of-sight turbulence over near-ground paths and implications for adaptive optics corrections in laser communications". *Applied Optics*, 37(21):4553–4560, 20 July 1998.

58. Linnik, Vladimir P. "On the possibility of reducing the influence of atmospheric seeing on the image quality of stars". *Opt. Spectrosc.*, 3:401, 1957.

59. Martin, Jan. *Simulation of Wave Propagation in Random Media: Theory and Applications*, 463–486. SPIE Press, Bellingham, WA, 1993.

60. Masanovic, Goran Z., Graham T. Reed, William Headley, Branislav Timotijevic, Vittorio M. N. Passaro, Raghied Atta, Graham Ensell, and Alan G. R. Evans. "A high efficiency input/output coupler for small silicon photonic devices". *Optics Express*, 13(19):7374–7379, September 2005.

61. McGlamery, Benjamin L. "Computer Simulation Studies of Compensation of Turblence Degraded Images". *SPIE/OSA*, 74:225–233, 1976.

62. Munson, K. (editor). *Jane's Unmanned Aerial Vehicles and Targets*. Jane's Information Group, Alexandria, VA, 2000.

63. Nikulin, Vladimir V. "Fusion of adaptive beam steering and optimization-based wavefront control for laser communications in atmosphere". *Opt. Eng.*, 44(10):106001, October 2005.

64. Noll, Robert J. "Zernike Polynomials and Atmospheric Turbulence". *J. Opt. Soc. Am.*, 66(3):207–211, March 1976.

65. Northcott, Malcolm J. *Performance Estimation and System Modeling*, chapter 7, 155–168. Cambridge University Press, Cambridge, UK, 1999.

66. Ohtsuki, Tomoaki. "Turbo-coded atmospheric optical communication systems". *IEEE International Conference on Communications*, volume 5, 2938–2942. 2002.

67. Osche, Gregory R. *Optical Detection Theory for Laser Applications*. Wiley Series in Pure and Applied Optics. Wiley-Interscience, Hoboken, NJ, 2002.

68. Pan, Feng, Jing Ma, Liying Tan, SiYuan Yu, and Chong Gao. "Scintillation characterization for multiple beams". Haimei Gong, Yi Cai, and Jean-Pierre Chatard (editors), *Infrared Components and Their Applications*, volume 5640, 448–454. SPIE Press, Bellingham, WA, 2005.

69. Parry, G. "Measurements of Atmospheric Turbulence Induced Intensity Fluctuations in a Laser Beam". *Opt. Acta*, 28:715–728, 1981.

70. Phillips, Ronald L. and Larry C. Andrews. "Measured Statistics of Laser-Light Scattering in Atmospheric Turbulence". *J. Opt. Soc. Am.*, 71:1440–1445, 1981.

71. Praus, II., Bob W. *WaveTrain User's Guide Online Documentation*. MZA Associates Corporation, 2021 Gerard SE, Suite 150, Albuquerque, NM 87106, Oct 2005. URL `http://www.mza.com/doc/`.

72. Recolons, Jaume and Federico Dios. "Accurate calculation of phase screens for the modelling of laser beam propagation through atmospheric turbulence". Stephen M. Doss-Hammel and Anton Kohnle (editors), *Proc. of the SPIE*, volume 5891. 2005.

73. Rhoadarmer, Troy A. "Development of a self-referencing interferometer wavefront sensor". John D. Gonglewski, Mark T. Gruneisen, and Michael K. Giles (editors), *Proc. SPIE - Advanced Wavefront Control: Methods, Devices, and Applications II*, volume 5553, 112–126. SPIE Press, Bellingham, WA, 2004.

74. Rhoadarmer, Troy A. and Jeffrey D. Barchers. "Noise Analysis for Complex Field Estimation Using a Self-Referencing Interferomter Wave Front Sensor". John D. Gonglewski, Mikhail A. Vorontsov, Mark T. Gruneisen, Sergio R. Restaino, and Robert K. Tyson (editors), *Proceedings of the SPIE - High-Resolution Wavefront Control: Methods, Devices, and Applications IV*, volume 4825, 215–227. SPIE Press, Bellingham, WA, Jul 2002.

75. Richardson, Lewis Fry. *Weather Prediction by Numerical Process*. Dover Publications, New York, 1922.

76. Ricklin, Jennifer C. and Frederic M. Davidson. "Atmospheric turbulence effects on a partially coherent Gaussian beam: implications for free-space laser communication". *J. Opt. Soc. Am. A*, 19(9):1794–1802, September 2002.

77. Ricklin, Jennifer C. and Frederic M. Davidson. "Atmospheric optical communication with a Gaussian Schell beam". *J. Opt. Soc. Am. A*, 20(5):856–866, May 2003.

78. Roberts, Phillip H. *A Wave Optics Propagation Code*. Technical Report TR-760, the Optical Sciences Company, Anaheim, CA, 1986.

79. Robertson, Lawrence and Troy Meink. "Transformational Communications". *Technology Horizons*, 6(3):10–11, Jun 2005.

80. Roche, James G. and John P. Jumper. *Air Force Directed Energy Master Plan*. Technical report, USAF, Washington D.C., 2003.

81. Roche, James G. and John P. Jumper. "The Edge: Air Force Transformation". Unpublished pamphlet, Washington, D.C. *www.oft.osd.mil/library/library_files/document_230_EDGEweb.pdf*, 30 May 2003.

82. Roggemann, Michael C. and Alan C. Koivunen. "Wave-front Sensing and Deformable-Mirror Control in Strong Scintillation". *J. Opt. Soc. Am. A*, 17(5):911–919, May 2000.

83. Roggemann, Michael C. and David J. Lee. "Two-deformable mirror concept for correcting scintillation effects in laser beam projection through the turbulent atmosphere". *Applied Optics*, 37(21):4577–4585, July 1998.

84. Roggemann, Michael C. and Byron Welsh. *Imaging Through Turbulence*. The CRC Press Laser and Optical Science and Technology Series. CRC Press, Boca Raton, FL, 1996.

85. Ruilier, Cyril. "A study of degraded light coupling into single-mode fibers". Robert D. Reasenberg (editor), *Proc. SPIE 3350, Astronomical Interferometry*, 319–329. SPIE Press, Bellingham, WA, 1998.

86. Ruilier, Cyril and Frédéric Cassaing. "Coupling of large telescopes and single-mode waveguides: application to stellar interferometry". *J. Opt. Soc. Am. A*, 18(1):143–149, January 2001.

87. Rumsfeld, Donald. "21st Century Transformation", 31 Jan 2002. Remarks as delivered by the Secretary of Defense at the National Defense University.

88. Ryan, Patrick T., William H. Lowrey, Imelda A. De La Ru, and Robert Q. Fugate. "Scintillation characterization for multiple beams". Michael C. Roggemann and Luc R. Bissonnette (editors), *Propagation and Imaging through the Atmosphere III*, volume 3763, 210–217. SPIE Press, Bellingham, WA, 1999.

89. Sasiela, Richard J. *Electromagnetic Wave Propagation in Turbulence*. Springer Series on Wave Phenomena. Springer-Verlag, Berlin, 1994.

90. Sklar, Bernard. *Digital Communications Fundamentals and Applications*. Prentice-Hall, Inc., Englewood Cliffs, NJ, 1988.

91. Staelin, David H., Ann W. Morgenthaler, and Jin Au Kong. *Electromagnetic Waves*. Prentice-Hall, Englewood Cliffs, NJ, 1994.

92. Tatarkskii, V. I. *Wave Propagation in a Turbulent Medium*. McGraw-Hill, New York, NY, 1961. Translated by R.A. Silverman.

93. Tatarkskii, V. I. *The Effects of the Turbulent Atmosphere on Wave Propagation*. NOAA Report No. TT 68-50464, U.S. Dept. of Commerce, Springfield, VA, 1971.

94. Thompson, Laird A. "Adaptive Optics in Astronomy". *Physics Today*, 47(12):24–31, December 1994.

95. Tyson, Robert K. *Principles of Adaptive Optics*. Academic Press, San Diego, CA, 2nd edition, 1998.

96. Tyson, Robert K. "Bit-error rate for free-space adaptive optics laser communications". *J. Opt. Soc. Am. A*, 19(4):753–758, April 2002.

97. Tyson, Robert K. and Douglas E. Canning. "Indirect measurement of a laser communications bit-error rate reduction with low-order adaptive optics". *Applied Optics*, 42(21):4239–4243, 20 July 2003.

98. Tyson, Robert K., Douglas E. Canning, and Jeffrey S. Tharp. "Measurement of the bit-error rate of an adaptive optics, free-space laser communications system, part 1: tip-tilt configuration, diagnostics, and closed-loop results". *Opt. Eng.*, 44(9):096002, September 2005.

99. Tyson, Robert K. and Benjamin W. Frazier. *Field Guide to Adaptive Optics*, volume FG03 of *SPIE Field Guides*. SPIE Press, Bellingham, WA, 2004.

100. Tyson, Robert K., Jeffrey S. Tharp, and Douglas E. Canning. "Measurement of the bit-error rate of an adaptive optics, free-space laser communications system, part 2: multichannel configuration, aberration characterization, and closed-loop results". *Opt. Eng.*, 44(9):096003, September 2005.

101. Wallner, E.P. "Optimal Wave Front Correction Using Slope Measurements". *J. Opt. Soc. Am.*, 73:1771–1776, 1983.

102. Wallner, Oswald, Walter R. Leeb, and Peter J. Winzer. "Minimum length of a single-mode fiber spatial filter". *J. Opt. Soc. Am. A*, 19(12):2445–2448, December 2002.

103. Welsh, Byron M. and Chester S. Gardner. "Performance analysis of adaptive-optics systems using laser guide stars and slope sensors". *J. Opt. Soc. Am. A*, 6(12):1913–1923, December 1989.

104. Whiteley, Matthew R. "Class Notes, EENG 699", 2005. School of Engineering and Management, Air Force Institute of Technology.

105. Yenice, Y. E. and B. G. Evans. "Adaptive beam-size control for ground-to-space laser communications". G. Mecherle (editor), *Proc. SPIE 3266, Free-Space Laser Communication Technologies X*, 221230. SPIE Press, Bellingham, WA, 1998.

106. Yenice, Yusuf E. and Barry G. Evans. "Adaptive beam-size control scheme for ground-to-satellite optical communications". *Opt. Eng.*, 38(11):1889–1895, 1999.

107. Yu, Meng, Jing Li, and Jennifer C. Ricklin. "Efficient forward error correction coding for free-space optical communications". Jennifer C. Ricklin and David G. Voelz (editors), *Proc. SPIE 5550, Free-Space Laser Communications IV*, 344–353. SPIE Press, Bellingham, WA, 2004.

108. Zhu, Xiaoming and Joseph .M. Kahn. "Free-space optical communication through atmospheric turbulence channels". *Communications, IEEE Transactions on*, 50(8):1293–1300, August 2002.

109. Zhu, Xiaoming and Joseph M. Kahn. "Markov chain model in maximum-likelihood sequence detection for free-space optical communication through atmospheric turbulence channels". *Communications, IEEE Transactions on*, 51(3):509–516, March 2003.

110. Zhu, Xiaoming and Joseph M. Kahn. "Performance bounds for coded free-space optical communications through atmospheric turbulence channels". *Communications, IEEE Transactions on*, 51(8):1233–1239, August 2003.

REPORT DOCUMENTATION PAGE

Form Approved
OMB No. 0704–0188

1. REPORT DATE *(DD–MM–YYYY)*	2. REPORT TYPE	3. DATES COVERED *(From — To)*
13–06–2006	Doctoral Dissertation	Sep 2002 — Mar 2006

4. TITLE AND SUBTITLE

Performance-Metric Driven Atmospheric Compensation
for
Robust Free-Space Laser Communication

5a. CONTRACT NUMBER

5b. GRANT NUMBER

5c. PROGRAM ELEMENT NUMBER

6. AUTHOR(S)

Peter N. Crabtree, Maj, USAF

5d. PROJECT NUMBER

5e. TASK NUMBER

5f. WORK UNIT NUMBER

7. PERFORMING ORGANIZATION NAME(S) AND ADDRESS(ES)

Air Force Institute of Technology
Graduate School of Engineering and Management (AFIT/EN)
2950 Hobson Way, Bldg 640
WPAFB, OH 45433-7765

8. PERFORMING ORGANIZATION REPORT NUMBER

AFIT/DS/ENG/06-03

9. SPONSORING / MONITORING AGENCY NAME(S) AND ADDRESS(ES)

Dr. Earl Spillar
AFMC/AFRL/DES
US Air Force Research Laboratory
Kirtland AFB, NM 87117
Earl.Spillar@kirtland.af.mil
505-846-6740

10. SPONSOR/MONITOR'S ACRONYM(S)

11. SPONSOR/MONITOR'S REPORT NUMBER(S)

12. DISTRIBUTION / AVAILABILITY STATEMENT

Approved for Public Release; Distribution is Unlimited

13. SUPPLEMENTARY NOTES

14. ABSTRACT

This research investigates atmospheric compensation techniques to mitigate the impact of turbulence on the performance of free-space laser communication systems. Several receiver-based techniques are developed given constraints relevant to tactical airborne platforms. First, wavefront control techniques was considered. In a moderate range air-to-air scenario, focal plane image breakup is identified as the dominant failure mechanism causing deep fades. This led to investigation of peak intensity tracking, which reduces fade probability by greater than 50% over conventional centroid trackers and Adaptive Optics (AO) systems for scenarios studied. Atmospheric compensation requirements were then examined based on deep fade phenomenology. For compensation techniques studied, regions of superior performance are identified. Peak tracking is shown to outperform AO for normalized detection thresholds below approximately 4% of the unabberated intensity. An adaptive binary decision threshold is the third major focus of this research. Analytic results show that an adaptive threshold decreases bit-error rate by up to 1.60 orders of magnitude (33-fold decrease) for a 10 Gbps link.

15. SUBJECT TERMS

optical communications, wavefront compensation, tracking, adaptive optics, atmospheric optics, scintillation

16. SECURITY CLASSIFICATION OF:			17. LIMITATION OF ABSTRACT	18. NUMBER OF PAGES	19a. NAME OF RESPONSIBLE PERSON
a. REPORT	b. ABSTRACT	c. THIS PAGE			Matthew E. Goda, Lt Col, USAF
			UU	190	19b. TELEPHONE NUMBER *(include area code)* (937) 255–3636, ext 4614